



SAPIENZA
UNIVERSITÀ DI ROMA

EARTH SCIENCES DEPARTMENT

PHD THESIS IN EARTH SCIENCES

XXVI cycle

**Ground deformation analysis by means of
satellite SAR interferometry: spatial and
temporal characterization and forecasting
potential**

ALFREDO ROCCA

Advisor:

Prof. Francesca Bozzano

Co –Advisors:

Daniele Perissin, PhD

Paolo Mazzanti, PhD

2010-2013

SUMMARY

1. INTRODUCTION	3
2. SATELLITE REMOTE SENSING FOR GROUND DEFORMATION MEASUREMENTS: SAR INTERFEROMETRY	10
2.1. SATELLITE SAR PRINCIPLES	10
2.2. SATELLITE SAR IMAGE FORMATION	12
2.3. DISTORTION EFFECTS AND ORBITAL GEOMETRY	14
2.4. SAR INTERFEROMETRY PRINCIPLES	16
2.4.1. SPATIAL COHERENCE AND DECORRELATION EFFECTS	20
2.5. ADVANCED DINSAR (A-DINSAR): OPPORTUNITIES AND LIMITATIONS	23
2.5.1. PERSISTENT SCATTERERS INTERFEROMETRY (PSI)	23
2.6. SAR SATELLITES: CURRENT SITUATION AND FUTURE PERSPECTIVE	28
3. DETECTION OF PAST SLOPE ACTIVITY IN A DESERT AREA USING MULTI-TEMPORAL DINSAR WITH ALOS PALSAR DATA	31
3.1. INTRODUCTION	31
3.2. STUDY AREA	33
3.2.1. GEOLOGICAL AND GEOMORPHOLOGICAL SETTING	33
3.3. MULTI-TEMPORAL DINSAR ANALYSES	37
3.3.1. C-BAND ARCHIVE SAR IMAGES	37
3.3.2. L-BAND ARCHIVE SAR IMAGES	38
3.3.3. ANALYSES OF ARCHIVED SAR DATA	40
3.4. INTERFEROMETRIC RESULTS	44
3.5. DISCUSSION	50
3.6. CONCLUSIONS	51
4. EXTENSIVE A-DINSAR AND GEOMORPHOLOGICAL STUDY OF LANDSLIDES EVOLUTION: BASIN-SCALE AND SINGLE PROCESSES INVESTIGATION	53
4.1. INTRODUCTION	53
4.2. THE STUDY SITE	55
4.2.1. GEOLOGICAL-STRUCTURAL CHARACTERISTICS	55
4.2.2. GEOMORPHOLOGICAL CHARACTERISTICS	56
4.3. LANDSLIDE MAPPING	59
4.3.1. METHODS	59
4.3.2. RESULTS	60
4.4. A-DINSAR ANALYSES	63
4.4.1. BASIC PRINCIPLES AND APPLICATIONS	63
4.4.2. A-DINSAR DATA PROCESSING	66
4.4.3. A-DINSAR RESULTS	69
4.4.4. CHARACTERISATION OF THE LANDSLIDE KINEMATICS	75
4.5. DISCUSSION	78
4.6. CONCLUSIONS	81

<u>5. UNDERSTANDING THE SUBSIDENCE PROCESS OF A QUATERNARY PLAIN BY COMBINING GEOLOGICAL AND HYDROGEOLOGICAL MODELING WITH SATELLITE INSAR DATA: THE ACQUE ALBULE PLAIN CASE STUDY</u>	83
5.1. INTRODUCTION	83
5.2. STUDY SITE	85
5.2.1. GEOLOGICAL SETTING	89
5.2.1. HYDROGEOLOGICAL SETTING	92
5.2.1.1. Groundwater numerical modelling	94
5.3. ADVANCED DINSAR ANALYSES	100
5.3.1. PERFORMED ANALYSES	100
5.3.1.1. Full-site analyses	102
5.3.1.2. Local-scale analyses	102
5.3.2. RESULTS OF A-DINSAR ANALYSES	103
5.4. DIAGNOSIS OF THE SUBSIDENCE PROCESS	108
5.5. CONCLUSIONS	113
<u>6. POTENTIAL FOR A-DINSAR TO PREDICT THE TIME OF FAILURE OF SLOPES</u>	115
6.1. INTRODUCTION	115
6.2. DETECTION OF NON-LINEAR PROCESSES BY A-DINSAR	118
6.3. DATABASE OF CREEP EVOLUTION FOR MONITORED LANDSIDES	121
6.3.1. INVESTIGATION OF LANDSLIDE TERTIARY CREEP USING A-DINSAR: A THEORETICAL APPROACH	124
6.3.2. INVESTIGATION OF LANDSLIDE TERTIARY CREEP USING A-DINSAR: A PRACTICAL APPROACH.	127
<u>7. CONCLUSIONS</u>	129
<u>REFERENCES</u>	134

1. INTRODUCTION

Natural hazards represent an increasing challenge in the modern world, where the impact on the populations of such phenomena (always occurring on our planet) is dramatically increasing.

The problem is complex and touches many (perhaps all) areas of society: politics, economy, industry and science. Among the causes of this growing impact, likely the primary cause is the increase in the vulnerability to natural hazards of modern societies that are characterised by an increasing technological level that exposes people to very diverse risks (Alexander, 1993; Smith, 2013). Moreover, increasing human population pressure is certainly a crucial aspect because populations settled in hazardous areas can cause or accelerate natural hazardous processes (Muller, 1964; Olshansky, 1996; Amelung *et al.*, 1999; Schuster & Highland, 2001; Syvitski *et al.*, 2009; Bozzano *et al.*, 2010).

Natural risk assessment and mitigation represents one of the primary fields of application for Earth sciences. Essentially, all disciplines related to Earth sciences could contribute to reaching this aim. Nevertheless, as suggested by Alexander (1993): “*Anecdotal and purely descriptive approaches should be avoided...Hence a rigorous approach to natural disasters requires that we look for the common regularities in each event, however unique it may at first seem*”.

Following this philosophy, many efforts have been made to address the problem of natural hazards for the quantification of the risk of landslides (Bell & Glade, 2004; Corominas *et al.*, 2013), subsidence (Kim *et al.*, 2006) and volcanoes (Blong, 1996; Jenkins *et al.*, 2014). In addition, the quantity of work performed on the evaluation of seismic risks is very vast and does not need to be summarised.

In this thesis, we want to focus on two particular types of natural hazards: ground subsidence and landslides.

In the frame of the quantitative approaches discussed above, the mitigation of such natural hazards has been addressed using different methodologies. Such approaches aim to define the hazard level spatially (susceptibility) and temporally (for example, by correlating with the triggering factors), both areally and focused on a single event. In addition, a complementary quantitative approach to address the issue focuses on the evaluation of the

vulnerability of constructed elements placed in the natural environment and seeks solutions that aim to mitigate possible risks.

From a general perspective, landslides and subsidence develop as ground deformation processes, and our objective is to focus on the effects produced by such phenomena, namely displacements. Following a different approach to address such issues, it is possible to derive useful information starting from quantitative measurements of deformations. On this topic, what Professor R. Peck stated several decades ago is still very true in several areas of engineering geology: “*The observational method (is) one of the most powerful weapons in our arsenal*”, and also: “*We need to carry out a vast amount of observational work, but what we do should be done for a purpose and done well*” (DiBiagio & Flaate, 2000).

Following the observational method philosophy, the availability of quantitative data on ground deformation (hence, displacements) plays a key role in achieving successful results in the understanding of such hazardous natural and anthropogenic processes. For the objective of natural risk reduction, the observational method results in a multiplicity of actions that are based on the collection of displacement data, allowing the accurate reconstruction of the evolution of the ground deformation over time.

Starting from the quantitative data provided by monitoring systems, many outcomes can be obtained. From laboratory experiments (Saito & Uezawa 1961; Saito 1965, 1969), it has been observed that the displacement is the best parameter for information regarding the time before natural materials failure occurs. In 1965, Saito applied this methodology to the prediction of the time of failure of a slope. In the following years, several authors demonstrated the predictive potential of the relationship between displacement-derived parameters and time of failure (Fukuzono, 1985; Crosta & Agliardi, 2003; Bozzano *et al.*, 2012; Mazzanti *et al.*, 2011). A special acknowledgement goes to Voight, who demonstrated the great potential of the observational method with predictive analyses related to the eruptions of Mount Saint Helen and also showed how the collapse of Mount Toc, on the Vajont artificial reservoir, could be anticipated well in advance (Voight, 1988; 1989).

However, to attain available reliable data about displacement, a proper monitoring system needs to be installed for the investigated area. Huge steps forward have been made in this field using remote sensing. Nevertheless, such techniques provide information only about

surface movements. More specifically, ground based remote sensing systems, both partially remote systems (e.g., robotic total stations and Global Navigation Satellite Systems - GNSS) and fully remote systems (e.g., reflectorless robotic total stations, terrestrial laser scanning, and terrestrial synthetic aperture radar interferometry) allow for the collection of data with very high spatial and temporal resolution and thus allow for the reconstruction of the deformation processes with very high accuracy and precision (Mazzanti, 2012). However, such techniques are strictly future-oriented; therefore (trivially), they are able to collect information only after an *ad-hoc* equipment installation has been performed for specific scopes. In the frame of remote sensing, a good opportunity to attain information about the past evolution of the territory, especially for landslides, is represented by a well-established methodology, such as aerial photo interpretation. Many archived aerial photos are available for several decades, and today, optical satellite data represent a new frontier in Earth Observation (EO). Unfortunately, optical data are affected by several limitations, primarily that they are strongly discontinuous in time, they have heterogeneous resolution, and above all, they do not allow the acquisition of highly accurate information about ground deformation.

The need for quantitative measurements of ground deformation (and therefore displacement) and the prior evolution of processes, led us to consider a technique that has proven to be extremely promising over the last decade, namely, Advanced Satellite Differential Synthetic Aperture Radar (SAR) Interferometry (A-DInSAR) (Ferretti *et al.*, 2001, 2011; Berardino *et al.*, 2002; Hilley *et al.*, 2004; Colesanti & Wasowski, 2006; Perissin & Wang, 2012; Wasowski & Bovenga, 2014).

Satellite SAR is a particular EO active system that is able to provide radar images with high spatial resolutions both night and day, with no limitations due to cloud coverage. The transmitted pulse interacts with the surface of the Earth, and only a portion of it is backscattered to the receiving antenna, thus forming an image of the observed scene. By combining the phase signal of the two SAR images (SAR interferometry - InSAR), acquired at different times over the same area, it is possible to derive information about displacements that occurred during the time interval between the two acquisitions (Moreira *et al.*, 2013). Using the ERS-1 satellite, the European Space Agency (ESA) has performed a quite systematic acquisition of almost worldwide SAR images beginning from 1992. Since then, there has been an exponential increase in SAR satellites placed into orbit by

many space agencies around the world, such as ERS-2 (1995, ESA), Radarsat-1 (1995, Canadian Space Agency), Envisat (2002, ESA), and ALOS PALSAR (2006, Japanese Space Agency). After this “first generation” of SAR satellites (almost all of which are no longer operating), many others are currently operational and acquire images with a more or less fixed revisit time with different radiometric characteristics and spatial resolutions. About the present satellites is well to remember: the COSMO-SkyMed constellation (from 2008, Italian Space Agency), TerraSAR-X (from 2007, German Space Agency), and Radarsat-2 (from 2007, Canadian Space Agency). Moreover, several new SAR satellites (Sentinel-1, Alos-2, Radarsat constellation, COSMO-SkyMed-2, and TerraSAR-X-2) will be launched in the near future, thus further expanding the availability of new SAR data for virtually any area of the planet.

The availability of the archives of many SAR images collected over more than 20 years has permitted the development, since the early 2000s, of methodologies for more complex and refined data processing that transformed InSAR into a real tool for ground deformation investigation over time. Such multi-image A-DInSAR methods (Ferretti *et al.*, 2001, 2011; Berardino *et al.*, 2002; Perissin & Wang, 2012) are thus able to provide time series of displacement for wide areas (thousands of square kilometres) related to targets with good and stable reflectivity of radar signals (buildings, transport routes, pylons, exposed rocks, portions of homogeneous soils and constructed structures such as dams and bridges). The possibility to exploit such reflectors, naturally present on the surface of the Earth, combined with the availability of archived images acquired over the last two decades, renders the A-DInSAR methods a unique tool for quantitative measurements of ground surface displacement with millimetre accuracy for areas where no monitoring has been performed in the past. Moreover, present and future satellites represent increasing opportunities in the field of future-oriented monitoring for wide and/or remote areas (Colesanti *et al.*, 2003a, 2003b; Colesanti & Wasowski, 2006; Wasowski & Bovenga, 2014).

In this context, the objective of this PhD thesis is to evaluate the spatial and temporal evolution of ground deformation processes by A-DInSAR to better understand the eventual forecasting potential offered by such techniques in the frame of the general observational methods described above.

Despite the great advantages offered, several technical and practical limitations affect the A-DInSAR methods (Colesanti & Wasowski, 2006; Wasowski & Bovenga, 2014). For this reason, it was necessary to perform the analyses on SAR images through non-standard methods to extract the best information in relation to the available data and the specific issues of the case studies. Moreover, the assessment of the issues related to the characteristics of the satellites/sensors used with respect to the topographical and morphological characteristics of the areas under investigation represented an important cause for reflection about the definition of proper study design. In particular, great efforts were made to determine the ability of the A-DInSAR methods to detect and quantify the presence of motions characterised by non-linear evolution in time (acceleration/deceleration). This aspect is crucial to evaluating the potential of the method for applications with predictive purposes.

The present work is divided into seven sections (including this introduction), and the central parts (Chapters 3-5) are structured as a series of scientific papers, related to specific applications of DInSAR and A-DInSAR for the purposes of the investigation of ground deformation, performed during the PhD research. The organisation of this work follows the most recent guidelines of the Cambridge University (Gustavii, 2012). Using this structure, the most significant parts of the thesis in terms of the data and research activities can be extracted from the larger work and read individually because the structure of a scientific paper is fairly standard and universal.

In more detail, this PhD thesis is organised as follows:

- ✓ Chapter 2 describes the primary features of satellite SAR systems and the interferometric techniques. This section of the thesis explains the potential of differential SAR interferometry (DInSAR) and the improvements attained by Advanced DInSAR (A-DInSAR), illustrating their respective advantages and limitations. In addition, a brief description of the past satellites is provided to illustrate the potential offered by archived SAR images as a tool for quantitative historical analyses. For present and future satellites, their potential for ground deformation monitoring is instead highlighted.
- ✓ Chapter 3 is focused on the first case study of this thesis, related to a coastal slope affected by gravitational stability issues. The slope, located in the Sultanate of Oman, has been successfully investigated in spite of some limitations in the

historical SAR data in terms of image availability that prevented the application of A-DInSAR techniques. In this case, a non-standard investigation through a DInSAR-based methodology allowed the quantitative evaluation of the temporal and spatial evolution of the past slope instability processes using ground deformation measurements. The objective of this Chapter is to demonstrate the potential of SAR data (and the value of historical archives) for the investigation of ground deformation, even when no advanced techniques can be applied.

- ✓ Chapter 4 is related to an in-depth A-DInSAR investigation of a portion of a basin in central Italy that is affected by many landslide processes. As result of nearly 20 years of acquisitions, the SAR data enabled the refinement of the mapping of these processes in both space and time (using the development of a matrix to estimate the state of activity of the slope). In addition, this case study presented several interesting aspects related to the kinematics of some landslide processes in relation to the observation geometries of the SAR satellites, thus allowing some considerations of the usefulness of proper study design.

The attained results have been presented at several national and international conferences, such as the IX National Conference of Young Researchers in Engineering Geology (14-15 of February 2013, Naples, Italy), the 33rd Annual Seminar of the Geotechnical Division (Hong Kong Institution of Engineers) (31st of May 2013, Hong Kong) and the ESA Living Planet Symposium 2013 (9-13 September 2013, Edinburgh, UK).

- ✓ Chapter 5 is related to a large-scale, anthropogenic ground deformation triggered by long-term quarry extraction activities in the Tivoli-Guidonia area (nearby Rome).

Using available data related to an inherited hydrogeological modelling of the underground water variations and detailed underground geological reconstruction, the A-DInSAR results allowed good definition of the mechanism of subsidence evolution in the affected area for the period 1992-2010. Moreover, using unconventional A-DInSAR analyses, the timing of subsidence triggering has been detected and measured. These results have also been useful in defining the potential of A-DInSAR methods to quantify and measure displacement processes affected by non-linear evolution in time.

This case study has been presented at the ESA Living Planet Symposium 2013 (9-13 September 2013, Edinburgh, UK).

- ✓ The objective of Chapter 6 is to discuss, in a critical sense, the potential for investigation of ground deformation using predictive applications based on the observational method. Beginning with the outcomes discussed in the previous chapters and using a database of landslides that were monitored until failure, the potential and limitations of the A-DInSAR methodologies are evaluated to judge the ability of the technique itself based on the data available today and in the light of the future prospects of the new SAR satellite data that will become available.
- ✓ Chapter 7 summarizes the main conclusions that have been reached thanks to the results of the research reported in this thesis.

2. SATELLITE REMOTE SENSING FOR GROUND DEFORMATION MEASUREMENTS: SAR INTERFEROMETRY

PREFACE

The following paragraphs aim to provide some basic information about satellite SAR systems and interferometric principles to facilitate the understanding of following parts of this thesis, focused on the activities performed. What follows should not to be considered an exhaustive treatment of the theoretical principles and analytical methods related to satellite SAR interferometry. For further information, please consult references mentioned in this chapter and listed in the bibliography.

2.1. Satellite SAR principles

A “RADAR” (Radio Detection And Ranging) is a system capable of emitting a pulse of electromagnetic energy and recording the return signal (echo), produced as a signal reflection from an object on the ground (target). This pulse propagates in the form of a wave having a wavelength belonging to the range of so-called microwaves. Because the system illuminates the scene, it is an “*active remote sensing system*”; solar lighting is not required, and the frequencies used by radars are able to pass through cloud cover. Using such equipment, we are able to determine the presence and distance of objects in the observed scene. The reflectivity of the objects observed on the surface is of primary importance, as well as the dielectric properties (ability to conduct/transmit) of these targets.

A SAR (Synthetic Aperture Radar) (Graham, 1974) system is a particular type of radar whose main characteristic is to exploit the movement along a predefined path (such as the orbit of a satellite platform where the sensor is mounted) to observe the same area from different viewing angles, thus synthesising a very large antenna to increase the ground resolution. This particular acquisition geometry is schematically shown in Figure 2.1. One of the main features of such a system is that the satellite observes the surface of the Earth with a side-looking configuration. This feature, that will be detailed later, has several important implications for the purposes of our work.

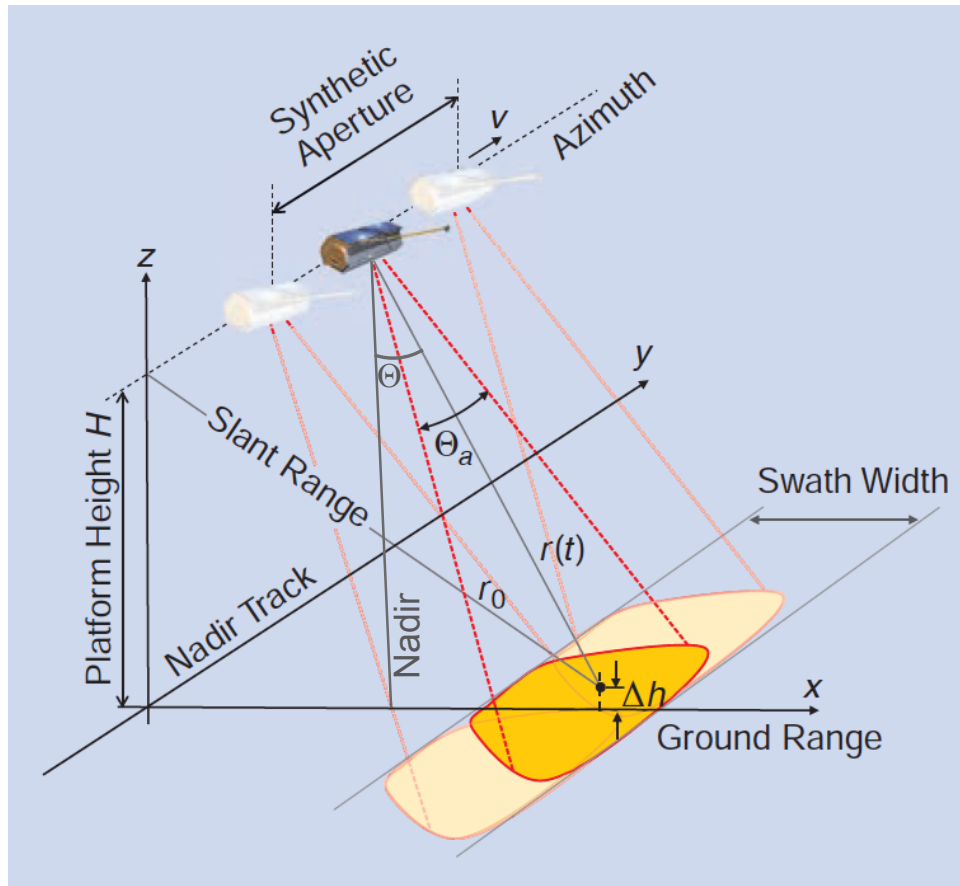


Figure 2.1 Illustration of the SAR imaging geometry. r_0 stands for the shortest approach distance, Θ_a for the azimuth beam width and v for the sensor velocity. Θ represents the off-nadir angle (from Moreira *et al.* 2013, modified).

Another important characteristic of SAR systems is to be anisotropic; SAR images, detected along the sensor-target path, called the LOS (Line of Sight), are characterised by the resolution in the Slant Range and in the Azimuth, which may differ. The former refers to the resolution along the direction of signal propagation (LOS), perpendicular to the orbit, with an angle (θ) with respect to the normal to the ground (off-nadir). The latter (azimuth) refers to the resolution along the direction of flight of the satellite, which in a first approximation can be considered essentially North-South.

In addition to satellite platforms (the most interesting for the purposes of this thesis), SAR sensors can be mounted on aircraft and also used in ground-based systems. Using the latter configuration, a particularly interesting displacement monitoring technique is performable, known as Terrestrial SAR Interferometry (TInSAR) (Luzi, 2010; Mazzanti, 2011). In this case, the SAR antenna is synthesised using a linear rail installed in front of the observed scene, along which transmitting and receiving antennas move.

2.2. Satellite SAR image formation

The SAR system illuminates an area on the surface of the Earth by transmitting a series of electromagnetic pulses and, after the measurement of the time delay between the transmitted and received echoes, is able to evaluate the distance (along the slant range) between the sensor and the illuminated targets on the ground. Because the SAR sensor moves along the orbital path during the radar signal transmission, a certain frequency shift in the receiving signal occurs (due to the Doppler effect).

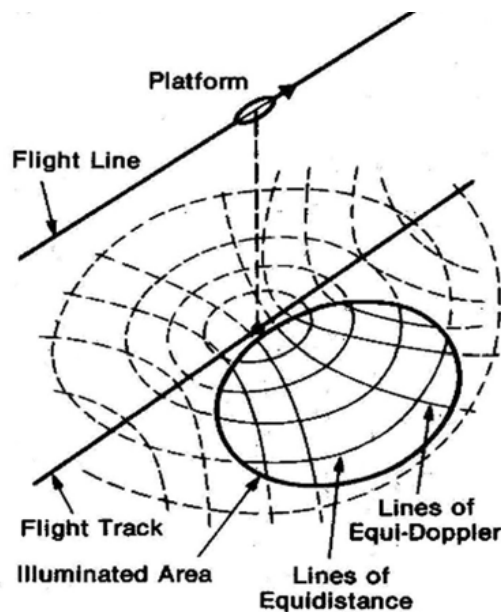


Figure 2.2 Coordinate system during a SAR acquisition (Elachi, 1988, modified)

In Figure 2.2, the points lying on concentric spheres, with their centres located in the position of the sensor, simultaneously return the reflection echoes. The intersection of these spheres with an imaginary horizontal plane generates a family of concentric circles that define the locus of points equidistant in range from the radar (equi-range). The nadir projection of the sensor on the ground represents the centre of the circumferences.

The points that lie on coaxial cones, with their shared axis coincident with the line of flight and the vertex of the radar, return echoes reflected with the same Doppler shift. The intersection of these cones with the horizontal plane generates a family of hyperbolic loci of points characterised by the same frequency shift (equi-Doppler) (Elachi, 1988).

Based on these considerations, we have a reference system consisting of concentric circles and hyperbolas in which each point can be identified by its time delay and Doppler shift. The only potential ambiguity regarding the identification of the target is due to the symmetry between the right and left with respect to the line of flight. If the illuminated area were centred at nadir, in the presence of equi-range targets, the sensor would record the same delay time, thus failing to distinguish between right and left. For this reason, the scene is illuminated with the side-looking configuration (Figure 2.1).

The thus-acquired raw data require a processing step (known as focusing) to convert the information from backscattered echoes into an image. Through this step, a complex matrix, known as the Single Look Complex (SLC), is obtained. In SLC images, pixels are arranged along Azimuth and Slant Range directions. Because SAR provides coherent signal, SLC pixels are characterised by a complex value (S) that can be represented as:

$$S = Ae^{i\varphi}$$

where A represents the Amplitude, and φ the Phase related to the signal backscattered by the targets on the scene. The amplitude identifies the portion of the incident electromagnetic field reflected back to the sensor (Figure 2.3), and the phase carries the most important information for our purposes: the sensor-target distance.

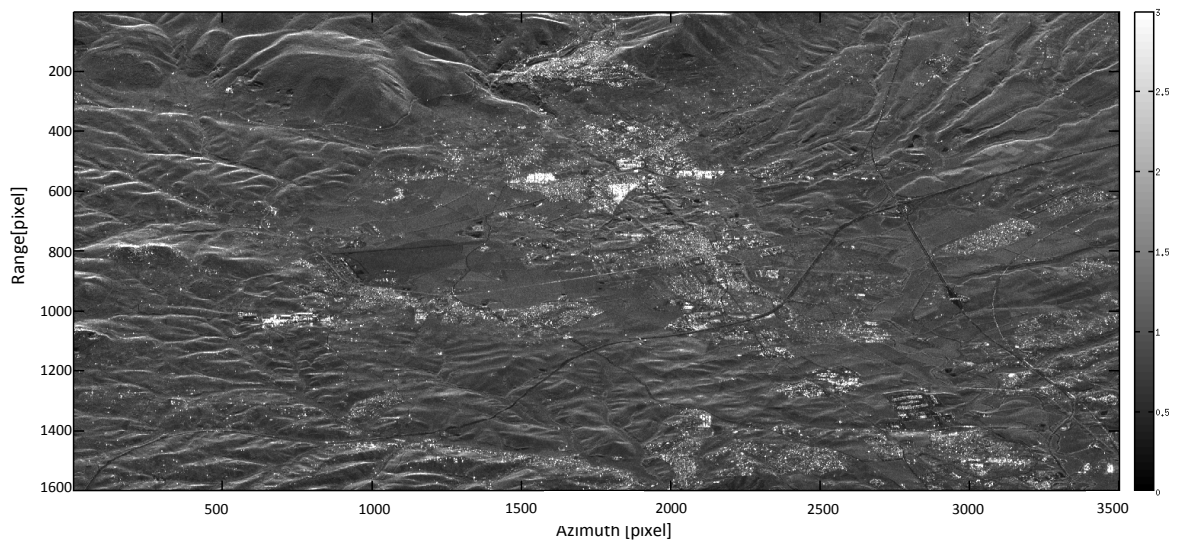


Figure 2.3 Example of amplitude signal from satellite SAR images. This figure is the result of 50 averaged amplitude images, acquired by Envisat satellite (European Space Agency) on the Guidonia-Tivoli area, near the city of Rome (Central Italy). Black pixels are related to targets with low reflectivity, while white pixels are related to targets characterized by good reflectivity of radar signal.

2.3. Distortion effects and orbital geometry

Because sensor-targets distances are not measured in the horizontal plane but in slant-range, SAR systems generate some distortion effects due to the interaction between the radar beam and the local topography (Simons & Rosen, 2007).

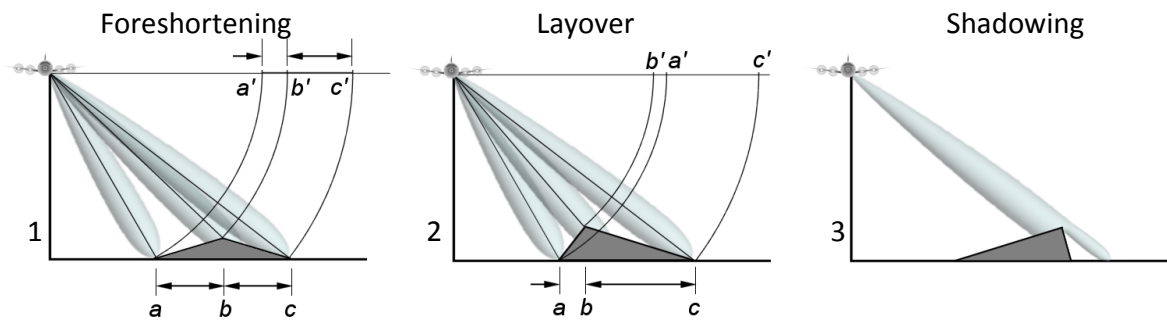


Figure 2.4 Radar distortion effects related to geometrical interactions between system acquisition geometry and local topography (from <http://www.radartutorial.eu/20.airborne/ab07.en.html>, modified.)

Foreshortening effect (Figure 2.4.1) occurs when the incident beam reaches the base of a high structure (e.g., a mountain slope) before the top. In this case, the correct geometry is recorded in the image, but the surface facing the SAR sensor (a-b) will be compressed into a few pixels, appearing smaller than reality (a'-b'). Because many targets fall inside a few image pixels, the backscattering contribution will be stronger than normal, and the SAR image will be brighter (Figure 2.5). For opposite conditions (i.e., a slope facing in the opposite direction with respect to the sensor), the b-c slope (with the same length as a-b) will be represented in a greater number of pixels in the SAR image (b'-c'). In this case, the area will be darker because the backscattering contribution, provided by the targets on the ground, will be distributed into several resolution cells (Figure 2.5).

Layover (Figure 2.4.2) is a very characteristic distortion effect in SAR images that is due to steep slopes or vertical structures. In these cases, the radar beam reaches the top of the structure (b) before the base (a). For this reason, the feature is recorded in the SAR image in opposite order (b'-a') and it seems “*laid down*” in the image.

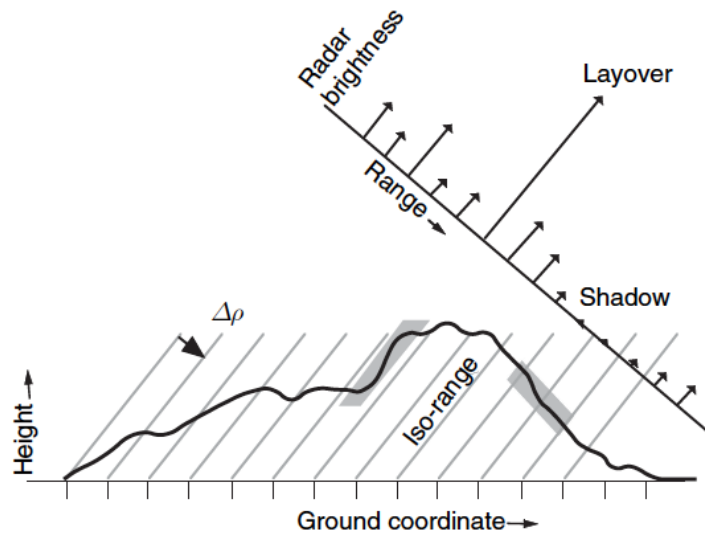


Figure 2.5 This sketch shows a profile of the terrain at constant azimuth, with the radar flight track into the page. The profile is cut by curves of constant range, spaced by the range resolution of radar ($\Delta\rho$). The backscattered energy from all surface scatterers within a range resolution element contribute to the radar return for that element (from Simons & Rosen, 2007, modified).

Shadowing effect is a quite intuitive effect related to the impossibility of covering areas masked by high objects, with an effect similar to shadows generated by solar illumination. In this case, such areas appear black, with a null backscattering signal to the sensor (Figure 2.4.3 and Figure 2.5).

However, limitations due to distortion effects can be prevented or mitigated by exploiting another typical peculiarity of satellite SAR systems explained below.

The capability of SAR satellites to acquire images of the entire Earth surface is the result of the combination of two movements: the quite fixed orbital path (quasi-polar) and the rotation of the Earth around its axis. Starting from this basic information, the satellite can observe the same area both during the North-to-South path (descending orbit) and during the South-to-North path (ascending orbit) (Figure 2.6). Because SAR satellites generally keep the same side-looking configuration for both orbital geometries, the result is that the same area can be observed from two different perspectives. This allows this method to overcome the limitations provided by radar distortions because they are dependent on the observation point.

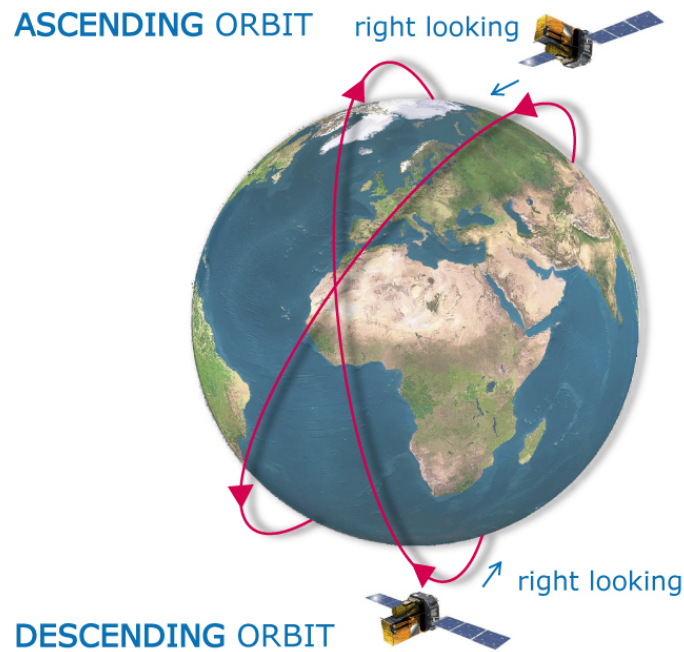


Figure 2.6 schematic sketches of ascending and descending orbits principle.

2.4. SAR interferometry principles

A basic requirement in performing interferometric analyses is to use only SAR images acquired with the same geometry (i.e., both images in ascending or descending orbit, same incidence angle, and same resolution). However, even in this case, some differences exist in terms of perspective because positions occupied by the satellite during image acquisition may differ for slight variations in orbital paths. The distance between satellite positions, more specifically its perpendicular component (normal baseline), plays a key role in interferometric results (Figure 2.7).

Amplitude is the part of the SAR signal useful for observing the surface features of the Earth, whereas the phase carries information essential for our purposes: the investigation of ground displacements. The basic technique used to derive information about displacements from SAR data is called Differential SAR Interferometry (DInSAR), which is based on the analysis of the variation in phase values between two acquisitions performed at different times (i.e., multi-pass interferometry) (Li & Goldstein, 1987, 1990; Gabriel & Goldstein, 1988; Goldstein *et al.*, 1988; Prati *et al.*, 1990; Hanssen, 2001; Simons *et al.*, 2002; Simons & Rosen, 2007; Tong *et al.*, 2010).

Such information is derived from the so-called interferogram (computed as the phase difference between two images), which represents the basic element of the methodology.

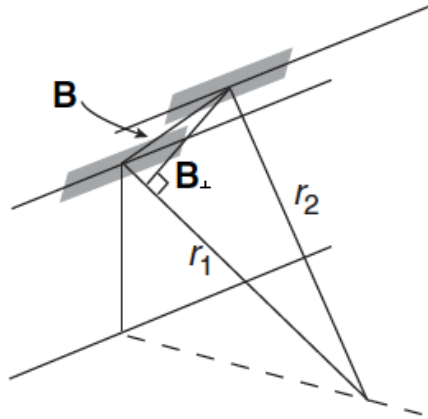


Figure 2.7 Multi-pass interferometry. The sketch represents geometrical baseline (**B**) and related normal baseline (**B_⊥**) between two acquisitions. Different satellite positioning determines different sensor-target distance (**r₁**, **r₂**), thus different points of view (from Simons & Rosen, 2007, modified).

More explicitly, the phase of each image pixel is formed by the sum of two terms:

$$\varphi = \varphi_s + \varphi_r$$

φ_s is related to the scatterers within the resolution cell, and φ_r depends on the dual satellite-target path and on the wavelength of the signal sent and subsequently recorded by the sensor itself:

$$\varphi_r = \frac{4\pi r}{\lambda}$$

where r is the satellite-target distance (along the LOS), and λ is the SAR sensor wavelength.

During the "satellite-target" path, the electromagnetic wave propagates in millions of cycles and reaches the portion of territory with a certain phase value. Therefore, it is reflected by various targets within the resolution cell (thus a random component due to multiple reflections is generated), and then, it returns to the satellite. For this reason the phase signal from a single SAR image does not carry any useful information. On the contrary, if we consider the phase difference, $\Delta\varphi$, between two images, the scatterer term

(φ_s) is cancelled out, and assuming that the backscattering characteristics have not changed, the phase difference (also known as interferometric phase) will be:

$$\Delta\varphi = \varphi_{int} = \frac{4\pi}{\lambda}(\Delta r)$$

The interferometric phase, φ_{int} , is characterised by several contributions:

$$\varphi_{int} = \varphi_{flat} + \varphi_{topo} + \varphi_{disp} + \varphi_{atm} + \varphi_{err}$$

φ_{flat} represent the flat Earth phase component due to different look angles on the same areas used by the satellite during the multi-pass acquisition. This condition leads to a disturbance that is easily removable using a reference ellipsoid.

φ_{topo} is the phase component related to topography. The relation between phase signal and topographic heights is expressed by the following equation (symbols are explained in Figure 2.8):

$$\varphi_{topo} = \frac{4\pi}{\lambda} B_{\perp} \cdot \frac{z}{r_1 \sin \theta}$$

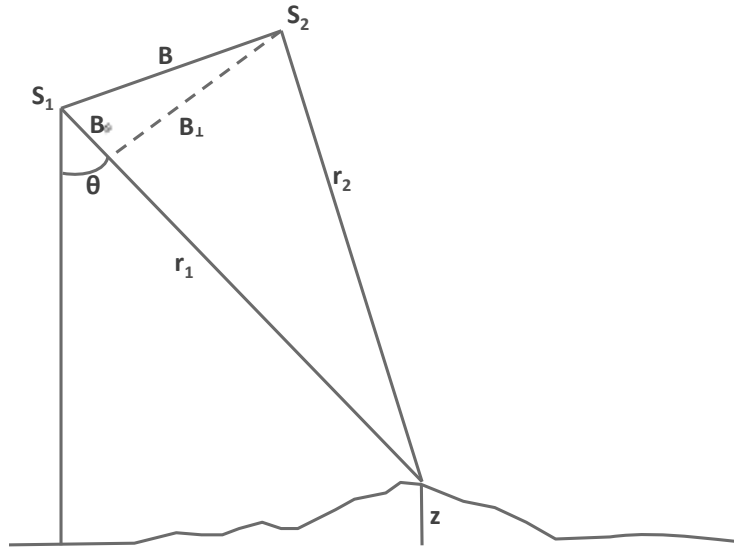


Figure 2.8 Geometry two SAR acquisition to estimate topographic phase component. S₁ and S₂ represent satellite position at different time (multi-pass); θ is the nadir-off angle; r₁ and r₂ are satellite-target distance for S₁ and S₂ respectively; B represents the geometrical baseline (exaggerated for clarity) with its normal and parallel components, while z represent the topographic height detected by SAR interferometry.

The phase component related to topography (Figure 2.9) is directly proportional to the normal baseline value; therefore, the system is more sensitive to topography when the SAR images used to compute the interferogram are characterised by a large baseline. However, an upper limit exists (the so-called “critical baseline”, B_c) whose value depends on the specific satellite, wavelength, acquisition geometry and spatial resolution. Baseline values higher than B_c do not allow the acquisition of useful information from the interferogram.

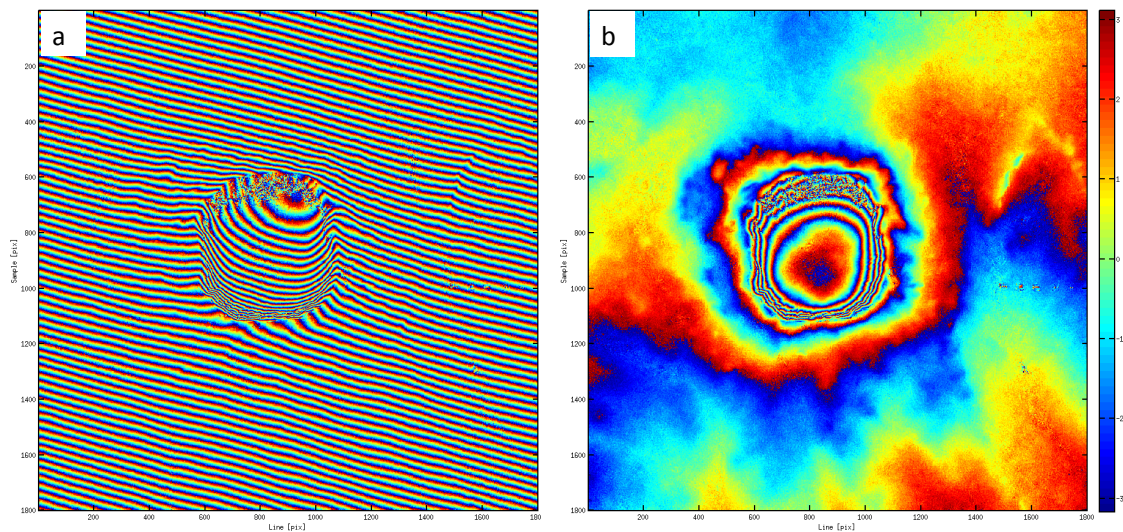


Figure 2.9 Example of interferogram of a crater in a desert area: with flat earth component (a) and the same interferogram after flattening process (b). In the latter, topographic phase contribution in the crater area is well visible, while the same is quite totally masked by “flat earth” still present in (a). SAR images, acquired by COSMO-SkyMed have been kindly provided by the Italian Space Agency.

φ_{disp} represents the phase component related to a ground displacement that occurred between the two acquisitions. If SAR interferometry is performed to detect displacements, φ_{topo} is subtracted using a Digital Elevation Model (DEM). Once φ_{flat} and φ_{topo} are removed, the so-called “differential interferogram” is obtained. However, in the differential interferogram, in addition to displacement information, the φ_{atmo} (due to atmospheric variations between the SAR acquisitions) and φ_{err} (decorrelation noise not directly determinable) values are also still present. In the case of spatially smooth displacements, these values are visible as coloured fringes (Figure 2.10), where one colour cycle corresponds to a displacement of half of wavelength λ .

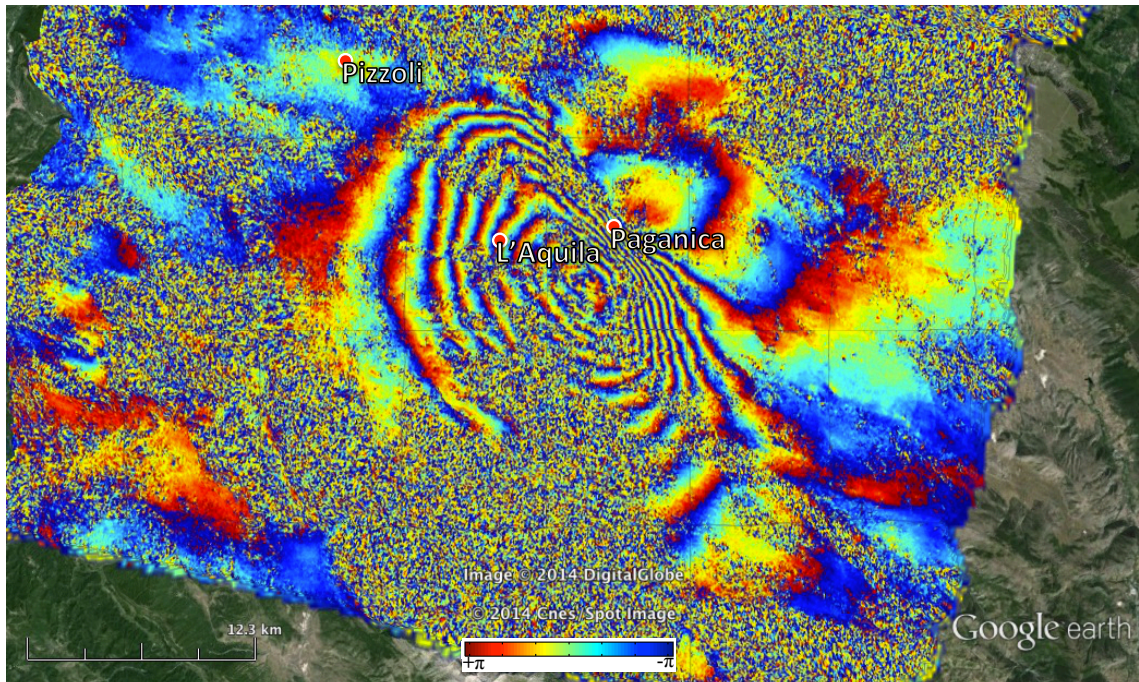


Figure 2.10 Example of differential interferogram showing co-seismic displacement of L'Aquila earthquake (6th of April 2009). The two images, used to generate this interferogram, have been acquired by Envisat Satellite (European Space Agency) on 1st of February 2009 and 12th of April 2009, respectively (Descending geometry, Track 79). Each interferometric fringe (from red to blue) corresponds to a displacement of 2.8 cm along the LOS. Raw SAR data have been provided by the open “ESA SAR dataset (Italy earthquake April 2009)”.

2.4.1. Spatial coherence and decorrelation effects

To provide a quantitative estimation of phase quality in SAR images, let us introduce the spatial coherence (γ), which is the cross-correlation coefficient of the SAR image pair, estimated on a window framed by several pixels in the azimuth and range. A moving window that covers the whole image is used to provide a coherence map (Ferretti *et al.* 2007). The spatial coherence, ranging from 0 to 1, represents an index of similarity between SAR images used to calculate the interferogram. According to Franceschetti *et al.*, (1995), the spatial coherence can be directly stated in relation to the Signal to Noise Ratio (SNR). When γ is 1, there is maximum correlation between images, whereas if γ is 0, then no correlation exists, and the signal is complete noise.

Several factors can affect phase signal, thus generating decorrelation effects (Zebker & Villasenor, 1992). Here, we want to focus primarily on the two main causes of decorrelation, which are temporal and geometrical decorrelation.

Temporal decorrelation may occur when the SAR images of the same area are taken with a temporal shift (so-called “temporal baseline”); therefore, objects may change their backscattering characteristics. In these conditions, the phase component due to objects within the resolution cell (φ_s) is no longer the same in the two images; therefore, the first condition of interferometry (see section 2.4) is not met. When SAR interferometry is performed to derive a DEM of a given area, it is very common to acquire images with a temporal baseline that is as low as possible. In this perspective, several spaceborne SAR missions adopted multi-satellites configurations to prevent long temporal baselines in images pairs, such as the ESA Tandem mission, with the twin satellites ERS-1 and ERS-2, which covered the same region with a 24-hour shift, or the German Space Agency (DLR), using the first bistatic SAR configuration provided by TerraSAR-X and TanDEM-X satellites to obtain an actual null temporal baseline.

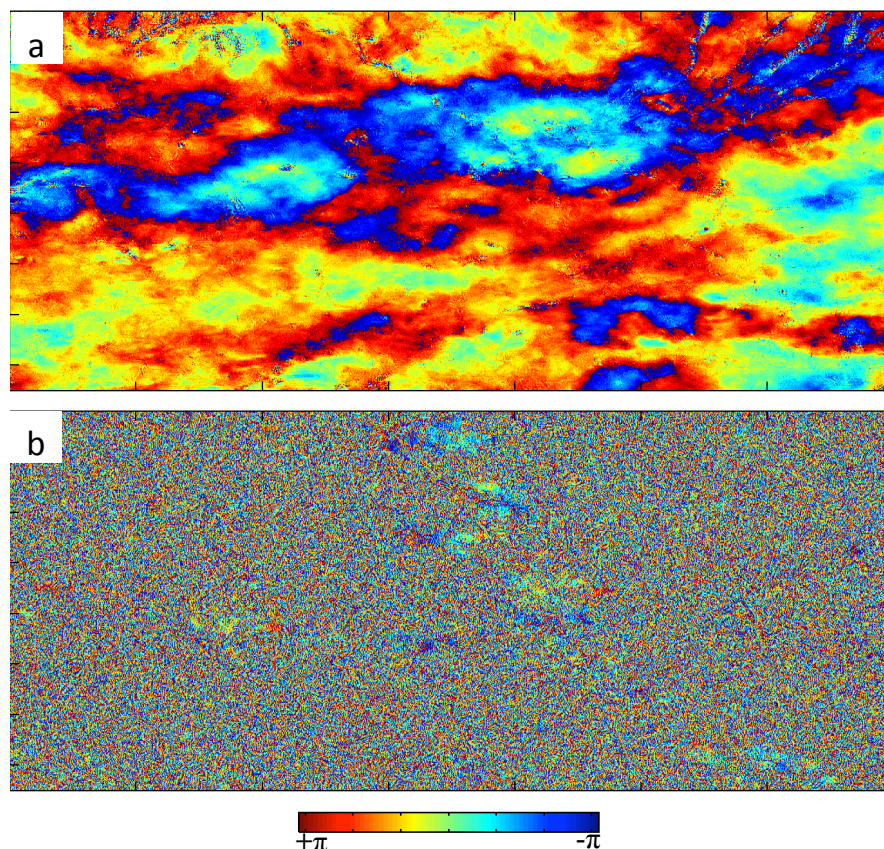


Figure 2.11 Example of temporal decorrelation over the same area observed by ERS data. Differential interferogram (a) is characterized by one day of temporal baseline while SAR images used to compute interferogram (b) have been acquired with more than 8 years of difference. Decorrelation in (b) is evident even if the interferogram has a very small normal baseline (11 m).

Another primary cause of decorrelation is due to the orbital baseline characterising the image pair and is called geometrical (or spatial) decorrelation. Because of the orbital baseline, the images are acquired under slightly different perspectives; this condition is necessary for the topographic InSAR applications, as long as the baseline is under its critical value (see section 2.4). Because different look angles lead to a shift between the range spectra of the SAR images (Franceschetti & Lanari, 1999), the same ground resolution cell will include backscattered phase signals that are too different from each other, even if no real changes occurred between the acquisition time interval (as for temporal decorrelation). It is quite evident that the spatial decorrelation increases as the geometrical baseline increases.

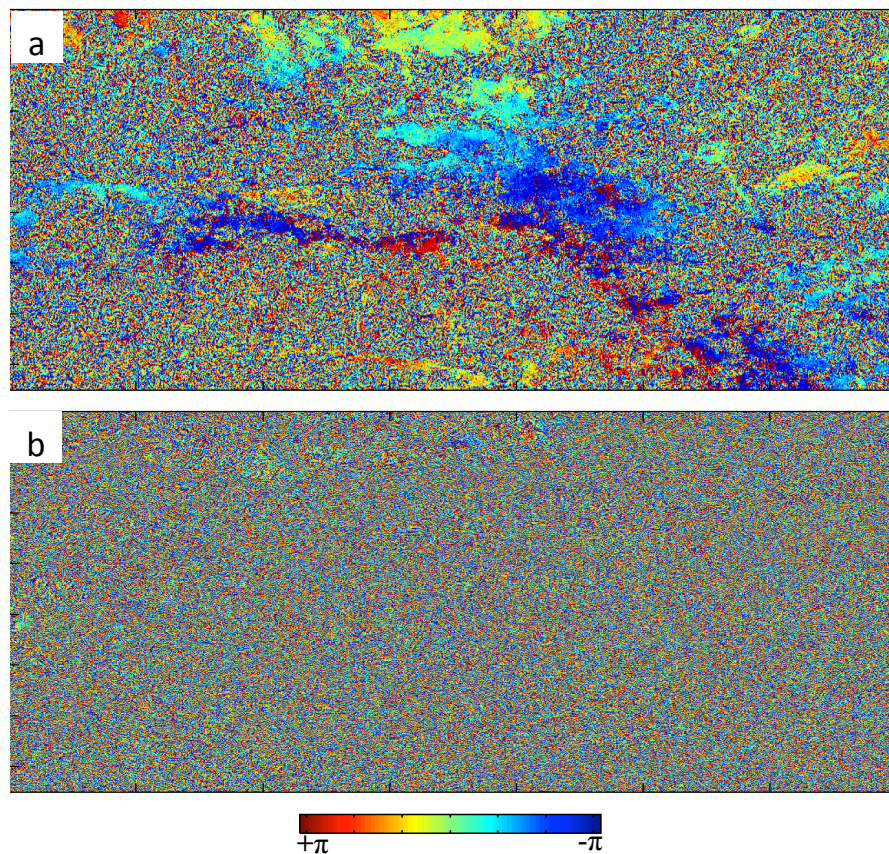


Figure 2.12 Example of spatial decorrelation over the same area observed by ERS data (ESA). Differential interferogram (a) is characterized by a small normal baseline (24 m) while the interferogram (b) is characterized larger normal baseline (910 m). Even if some decorrelation effects are present in both images, in (a) phase signal on urbanized areas and infrastructures is totally noiseless.

2.5. Advanced DInSAR (A-DInSAR): opportunities and limitations

DInSAR represents a valuable tool for digital elevation modelling and investigation of displacement; nevertheless, it is characterised by some limitations, primarily related to the impossibility in investigating both topography and displacements in a single image pair, the presence of atmospheric disturbance affecting the attained results (sometimes quite seriously) and finally, the dependence on image pairs characterised by high spatial coherence to obtain reliable results (in turn, related primarily to the geometric and temporal characteristics of the available images).

Over the last decade, the development of multi-image InSAR techniques, also known as Advanced DInSAR (A-DInSAR), has partially overcome such limitations. Because all A-DInSAR methods are based on the exploitation of multiple SAR scenes, the availability of many historical images archived by several space agencies plays a key role.

First, by using such datasets of many SAR images, A-DInSAR methods allow for the estimation and removal of the atmospheric contribution, which can seriously obscure deformation processes. These methods also allow the analysis of multi-temporal deformation processes with the possibility of obtaining time series of displacement for many measuring points on the observed scene.

Many authors have successfully developed several approaches, all with the objective of solving a common issue: how to increase coherence (to obtain a good phase signal) in available multi-image datasets. Ferretti *et al.* (2001) focused on the analysis of single points (pixels), starting from the assumption that point-like scatterers that are stable in radar reflectivity through time (the so-called Permanent or Persistent Scatterers – PS) are also characterised by high coherence over the whole period during which the SAR images have been acquired. Berardino *et al.* (2002) have addressed this problem by using redundant interferograms generated by connecting SAR images characterised by small baselines, thus performing the phase signal inversion with the most coherent data as possible.

2.5.1. Persistent Scatterers Interferometry (PSI)

Methods based on the Persistent Scatterers InSAR approach (PSI) are generally the most common among the A-DInSAR techniques. The PSs are privileged "measurement points" identified by the satellite on the surface of the Earth. The response to radar reflection of

such targets permits accurate measurements of their distance from the sensor, thus allowing the detection of millimetre displacements. Such good measurement points are targets with good, stable backscattering of radar signal emitted by the satellite sensor. This characteristic is typical of buildings, transport routes (roads, railways), pylons and constructed structures, such as dams and bridges. Exposed rocks and portions of homogeneous soils can also sometimes behave as PSs.

This dense network of measurement points allows the detection and measurement of punctual displacements (e.g., a single building) and the reconstruction, on a larger scale, of patterns of surface displacement processes (e.g., landslides, subsidence, and faults) (Figure 2.13).

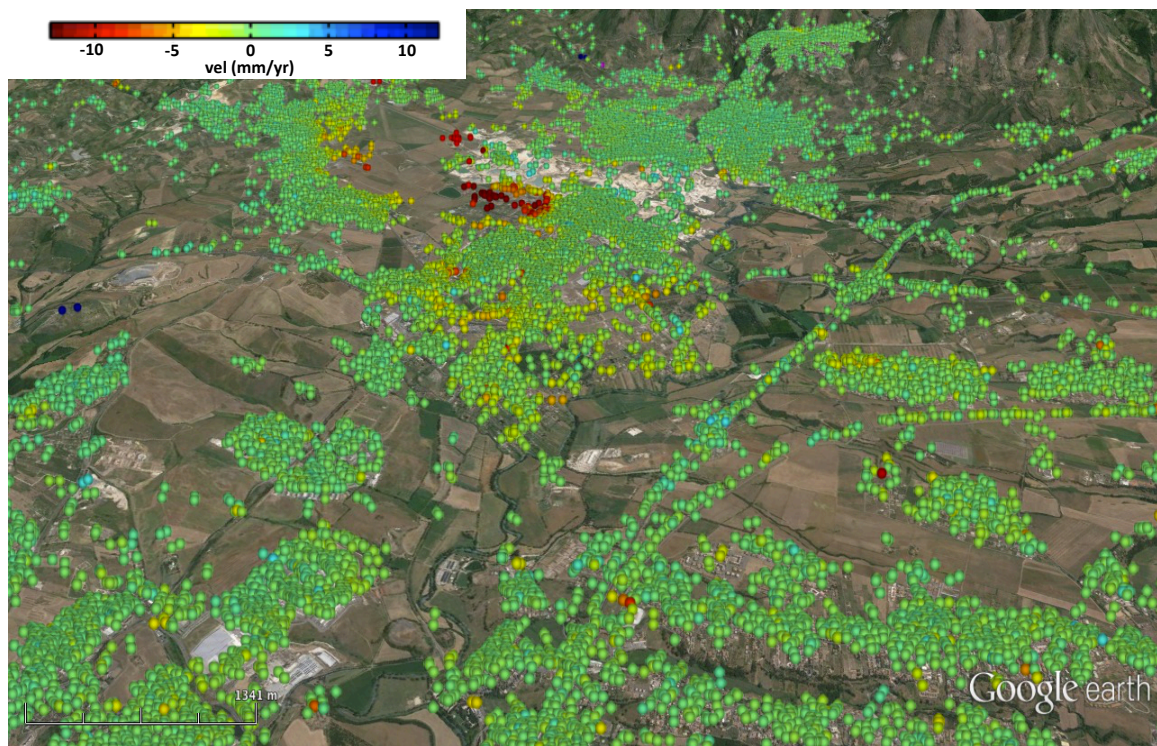


Figure 2.13 Typical representation of A-DInSAR results by PSI analysis. Each point is a PS and it represents a measurement point. Colours are related to displacement rate along the LOS: from yellow to red they indicate movements away from the satellite, while from light blue to dark blue points are affected by displacement toward the satellite. Green points are stable.

In the PSI technique, interferograms are computed coupling all images with a single master, which is selected to reduce the temporal and geometric decorrelation phenomena. To reach this objective, the master image is the one that minimises the dispersion of the

geometrical and temporal baseline compared with the other images in the dataset, which are set as slaves.

As in the DInSAR technique, displacements are measured only in the component along the sensor line of sight (LOS). In the presence of purely vertical movements (e.g., subsidence), the estimated motion is easily ascribable to deformation along the vertical direction; however, if the investigated target is affected by horizontal displacements, it is not possible to distinguish the two contributions without an a priori assumption.

The possibility of available images acquired with quite specular and symmetric geometries can be exploited to overcome this typical limitation of DInSAR techniques. By combining the interferometric results of a given area, computed from both the ascending and descending data, it is possible to derive the vertical and horizontal displacement starting from the two LOS displacement results. Because SAR satellite orbits are on near North-South paths, the error in the estimation of the horizontal displacements is acceptable only for the East-West direction. However, several attempts at three-dimensional displacements reconstruction have been made, as reported by Hu *et al.* (2014).

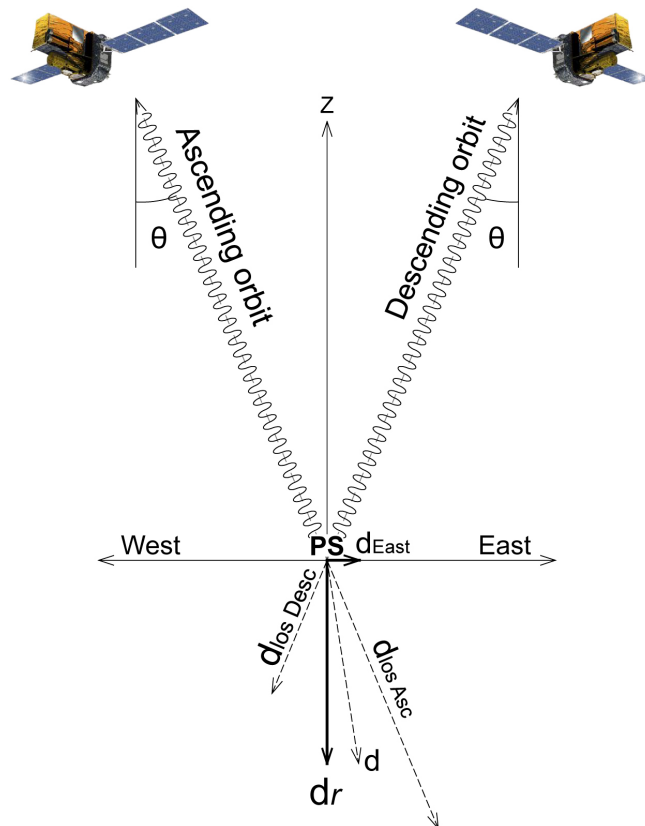


Figure 2.14 The combination of results from ascending and descending datasets allows deriving horizontal and vertical component of observed displacement.

Basically, PSI and other A-DInSAR techniques are based on the analysis of phase signals, performed to estimate and separate all phase contributions for all PS candidates. Generally, A-DInSAR algorithms estimate searched parameters (e.g., topographic height and deformational rate), detecting and removing noise caused by atmospheric disturbance as well as other sources of errors (e.g., orbital inaccuracy). A typical method to accomplish this objective is the use of deformation models (mainly linear) to infer the phase component due to displacements that occurred during the SAR image acquisition period. Each PS has an associated temporal coherence value, which measures the agreement between the measured data and the model used in the phase analysis.

This aspect represents a key point because in some cases, the model used can strongly influence the identification and measurement of the real deformation processes; this will be discussed more in detail in following sections.

It should be observed that the deformation estimations are differential; they do not express an absolute value of displacement of points on the ground, but they are in relation with a reference point chosen as stable.

There are many advantages introduced by this remote sensing technique for the investigation of ground displacements:

- PSs constitute a sort of "natural geodetic network", i.e., the objects are already in the area, such as buildings, transport routes (roads, railways), other constructed structures, and exposed rocks; thus, the installation of artificial reflectors is not necessary;
- several surface deformation phenomena (e.g., subsidence, landslides, and faults) can be analysed both for future (monitoring) and past processes investigation;
- each point is characterised by a time series of displacement with millimetre accuracy;
- the extent of SAR images (up to 100 km side) allows for the rapid analysis of large areas;
- the results integrate well into geographic information systems, allowing rapid integration with other investigative techniques.

However, the following aspects related to A-DInSAR should also be considered:

- the analysis of deformation phenomena with rapid evolution is very difficult because the observable displacement is related to the sensor wavelength: the maximum displacement between the acquisition of two consecutive images is equal to $\lambda/4$, and some attempts are only possible by using a priori information on the investigated phenomenon (Ferretti *et al.*, 2005);
- for the same reason, phenomena characterised by impulsive movements can also not be monitored with this technique;
- as with DInSAR, the A-DInSAR methods allow the observation of displacements only along the Line of Sight;
- Strongly vegetated areas are very difficult to investigate.

A-DInSAR methods based on a PS InSAR approach (PSI) have been used in the analyses reported in this thesis because these methods have been considered the most robust, especially for a time series of displacement reconstruction that is, also thanks to temporal continuity ensured by interferograms computed with a single master image.

Moreover, several improvements have been made recently with respect to the initial PS technique (Werner *et al.*, 2003; Bovenga *et al.*, 2004; Hooper *et al.*, 2004; Van Leijen & Hanssen, 2007; Costantini *et al.*, 2008; Ferretti *et al.*, 2011; Perissin & Wang, 2012). Among the studies just mentioned, the QPS method (Perissin & Wang, 2012) merits a more detailed description.

One of main limitations of the PS technique is represented by the low spatial density of targets, especially for non-urban areas. In the application of the A-DInSAR technique, the absence of the measurement points represents a strong limitation to attain reliable results. Perissin & Wang (2012) have developed a new approach that loosens the strict conditions imposed by the PS technique. Through this innovative method, it is possible to extract information from "partially coherent targets", thus increasing the spatial distribution of the measurement points.

Several differences characterise the QPS method from the classical PS method: i) it is no longer necessary to connect all of the images of the dataset with a single master image (in some cases, in fact, it is not possible to attain good coherence for all pairs of images of a long dataset as required for the PS technique); ii) the parameters (e.g., height and displacements) are estimated on an appropriate target-dependent subset of interferograms;

iii) a spatial filter is applied to the interferometric phase to increase the signal-to-noise ratio.

In particular, in the present thesis, a hybrid method based on the standard PSI (Ferretti *et al.*, 2001) and Quasi-Persistent Scatterers (QPS) technique (Perissin & Wang, 2012) has been adopted to attain better results in terms of a reliable time series of displacement (using the PS approach) and wider spatial covering (using QPS).

All analyses of SAR data have been performed using the software tool SARProz (Perissin *et al.*, 2011).

2.6. SAR satellites: current situation and future perspective

One of most interesting aspects of satellite SAR interferometry is the possibility of performing analyses based on archived data acquired in the past. If archive images are available, quantitative information about past ground displacements are thus achievable.

Beginning in 1992, due to the ERS mission of the European Space Agency, a quite systematic worldwide coverage of the surface of the Earth has been performed. In the following years, new satellites launched by several space agencies have enabled the increasing availability of SAR data with various characteristics.

This variety of data is an important resource as many factors may influence A-DInSAR results, especially in relation to specific ground deformation processes (such as landslides). Several technical features of SAR sensors can play key roles in achievable outcomes: i) the period covered by the data acquisition; ii) the revisit time of the satellite (i.e., the sampling frequency of the data acquisition); iii) geometrical aspects of sensor/satellite acquisition; iv) sensor wavelength (because it directly influences many other aspects, among those, the capability to measure certain deformation trends); and v) spatial resolutions.

Presently, several SAR datasets acquired by sensors in the L-, C-, and X-bands are available. Tab. 2.1 shows historical missions from 1992 to present and missions planned for the near future. Clearly, the sensor features are very variable in terms of the wavelength (band), operational and life status, spatial resolution, revisit time, image size and geometry of ground observation (incidence angle). In this regard, the latest satellites are particularly interesting because they have the ability to modify some observation geometric parameters (e.g., the incidence angle) to better satisfy specific needs.

Tab. 2.1 Selected characteristics of principal Synthetic Aperture Radar (SAR) sensors (from Wasowski & Bovenga, 2014, modified).

Satellite mission	Wave-length (cm)	Life status	Resolution Az./Range (m)	Repeat Cycle (days)	Swath width (km)	Max. Vel. (cm/yr)	Incident Angle (degree)
C-band							
ERS-1/2	5.6	1992÷2001	≈6 / 24	35	100	14.6	23
ENVISAT	5.6	2003÷2010	≈6 / 24	35	100	14.6	19÷44
RADARSAT-1	5.5	1995÷	≈8÷30	24	45 (fine) 100 (Strip) 200 (Scan)	20.4	20÷50
RADARSAT-2	5.5	2007÷	≈3 / 3 ≈8 / 8 ≈26 / 25	24	10 (Spot) 40 (Strip) 200 (Scan)	20.4	20÷50
Sentinel-1 RADARSAT constellation mission (3 sat)	5.6	2014÷2024	5÷20	6, 12	250	85	30÷46
	5.5	2018÷2026	5÷50	3, 12	30÷350	163.2	20÷55
L-band							
J-ERS	23.5	1992÷1998	18	44	75	48.7	35
ALOS PALSAR	23.6	2006÷2011	≈5 / 7÷88	46	40÷70	46.8	8÷60
ALOS PALSAR-2	22.9	2014÷2017	1/3 3÷10/3÷1 0 100/100	14	25 (Spot) 50÷70 (Strip) 350 (Scan)	149.2	8÷70
SAOCOM (2 Sat)	23.5	2014÷2021	10÷50	8, 16	20÷150	268	20÷50
X-band							
COSMO-SkyMED (4 Sat)	3.1	2007÷	≈2.5 / 2.5 1.0 / 1.0	2, 4, 8, 16	10 (Spot) 40 (Strip) 200 (Scan)	17.7 35.4 70.7 141.4	20÷60
TerraSAR-X	3.1	2007÷	≈3.3 / 2.8 1.0 / 1.0	11	10 (Spot) 30 (Strip) 100 (Scan)	25.7	20÷55
COSMO-SkyMED-2 (2 Sat)	3.1	2015÷2023	1÷3	-	10÷40		
TerraSAR-X-2	3.1	2015÷2018	0.5÷4	-	10÷40		

Although they were characterised by quite low spatial and temporal resolution, the first C-band (wavelength approximately 5 cm) ESA satellites (ERS-1/2 and Envisat) represented a milestone for SAR interferometry and Earth observation in general. Because of their large number of archived images, they represented a unique resource for nearly twenty years of studies of Earth surface dynamics.

The Canadian Space Agency (CSA) significantly increased both spatial and temporal resolutions using the RADARSAT-1/2 satellites. The same direction has been taken by the ESA with the Sentinel-1 double satellite mission; the first satellite is planned to be launched within the first half of 2014.

The L-band data (wavelength of more than 20 cm) were provided by the Japanese Space Agency satellites J-ERS and ALOS PALSAR. In the near future, new data will be available from the new satellite ALOS PALSAR-2 and the Argentinean constellation SAOCOM CONAE, both to be launched in 2014.

Finally, new frontiers in SAR interferometry have been opened by a new generation of X-band satellite sensors (wavelength ~ 3 cm). The constellation of four twin satellites of COSMO-SkyMed by the Italian Space Agency (ASI) and the TerraSAR-X and TanDEM-X satellites of the German Space Agency (DLR) have dramatically increased both the spatial (from 3 to 1 m) and temporal resolution (from 11 to 4 days) of the available data. With this higher temporal frequency and spatial resolution, X-band satellites represent a valuable source of data for present and future ground displacement investigations (Wasowski & Bovenga, 2014).

3. DETECTION OF PAST SLOPE ACTIVITY IN A DESERT AREA USING MULTI-TEMPORAL DINSAR WITH ALOS PALSAR DATA

3.1. Introduction

The use of Earth Observation (EO) data for the investigation of remote areas (deserts, forests and generally areas with insufficient lines of communication) plays a key role in acquiring both preliminary information and monitoring data for several fields of infrastructure and natural hazard management (Barrett, 2013). Among spaceborne EO techniques, Synthetic Aperture Radar (SAR) represents an interesting and widely used tool. Because SAR systems are based on active sensors, they are able to provide information both night and day and in the presence of cloud coverage, thus expanding upon the opportunities offered by optical systems. Characteristic of radar sensors is the use of coherent signals, i.e., the capability of retaining information about the phase component of the electromagnetic signal. Therefore, the pixels of the SAR images include both amplitude and phase terms. The former is related to the reflection intensity of the scattering targets, and the latter is related to sensor-target distance. This peculiarity has been exploited in recent decades, turning earth observation spaceborne SAR systems into tools to provide quantitative data, using interferometric processing techniques (InSAR).

Multi-pass classical InSAR is performed by coupling SAR images to generate a single interferogram to perform phase signal analyses (Li & Goldstein, 1987, 1990; Gabriel & Goldstein, 1988; Goldstein *et al.*, 1988; Prati *et al.*, 1990; Hanssen, 2001; Simons *et al.*, 2002; Tong *et al.*, 2010). The phase signal of a single interferogram, however, carries information related to several contributions (e.g., topography, displacement, atmospheric artefacts, and noise). If the temporal baseline (namely, the time interval between the acquisition of the two repeat pass scenes used to compute the interferogram) is short enough, we can assume that no displacement occurred and thus ascribe all phase signals to topographic contribution. In contrast, to acquire information about displacements that occurred in the time interval between the acquisitions of two SAR scenes, the topographic contribution can be subtracted from the derived interferogram (e.g., by an available Digital Elevation Model). In the latter case, this technique, known as Differential InSAR – DInSAR, has been successfully applied in the investigation of various ground deformation processes. DInSAR provides good results for the investigation of displacement

characterised by wide, spatially smooth deformation processes, such as coseismic and postseismic deformations (Massonnet *et al.* 1993, 1994), volcanic deformation processes (Massonnet *et al.* 1995) or ice and glacier dynamics (Goldstein *et al.* 1993; Kwok & Fahnestock, 1996). However, landslide displacements have also been detected and measured by DInSAR (Carnec *et al.*, 1996; Fruneau *et al.*, 1996; Singhroy *et al.*, 1998; Singh *et al.*, 2005; Strozzi *et al.*, 2005, 2010; Riedel & Walther, 2008; Garcia-Davalillo *et al.* 2014, Jebur *et al.* 2013).

As stated above, one of the primary limitations of DInSAR is the difficulty in separating the different contributions affecting the interferometric phase signal. Moreover, DInSAR cannot be supported by effective solutions for the detection and removal of an atmospheric disturbance. Finally, noise caused by temporal decorrelation (i.e., a long time interval between multi-pass SAR scene acquisition) and/or geometrical decorrelation (i.e., long distance between positions occupied by satellite during scene acquisition) can seriously prevent the attainment of useful interferometric results.

To compensate for these limitations, several data processing approaches have been proposed, namely Advanced DInSAR (A-DInSAR). All of them exploit long time series of SAR images of the same area to attain some common results: i) estimation and removal of atmosphere artefacts (i.e., Atmosphere Phase Screen – APS); ii) contemporary estimation of several phase contributions (at least, topography and displacement); iii) capability of providing time series of deformation along the whole time interval. The development and diffusion of Advanced Differential SAR Interferometry (A-DInSAR) methods over the last decade have significantly increased the range of applications of SAR data for past-oriented investigation and for future monitoring of ground displacements (Ferretti *et al.* 2001, 2011; Berardino *et al.* 2002, Hooper *et al.*, 2004, Lanari *et al.*, 2004; Lauknes, 2004; Kampes, 2006; Van Leijen & Hanssen, 2007; Perissin, 2008; Stramondo *et al.*, 2008; Perissin *et al.*, 2011, 2012; Bozzano & Rocca, 2012).

From this perspective, if DInSAR is able to provide a “snapshot” of a given deformation process in the time interval between the acquisition of two scenes, A-DInSAR approach is actually able to provide displacement information over time, such as long-term time series of displacement.

However, some conditions need to be satisfied to perform A-DInSAR analysis, such as the availability of a large quantity of SAR images (conventionally, greater than 20) acquired

with the same geometric and radiometric features over the same area. However, especially in remote areas, this condition cannot be always satisfied by space agency archives.

For the area investigated in this chapter, only few archive images from the ALOS PALSAR, ERS and Envisat sensors were available; hence, DInSAR analyses were performed using a redundant approach suitable for increasing the reliability of the attained results.

The study presented herein is of a coastal slope in the Dhofar region in the Sultanate of Oman involved in the construction of a major road (Hasik - Ash Shwaimiyah Project). As the slopes experienced some gravitational instability processes during construction activities during the period August 2011-June 2012, our objective was to better understand the stability conditions of such a slope before the above-mentioned time interval. To attain quantitative information related to past displacements, InSAR based approaches represent the only available solutions.

3.2. Study area

The study area is in the Dhofar region (Oman, in the eastern Arabian Peninsula) (Figure 3.1), located inside the Hasik graben, north of the riverbed of Wadi Dahanat (almost always dry). The area under investigation is a steep barren slope under a high cliff facing the Kuria Muria Bay. The slope, affected by instability issues, has been involved in the construction of a road to connect Hasik to the northern village of Ash Shuwaymiyyah.

3.2.1. Geological and geomorphological setting

The Hasik Graben is an Oligocene onshore deformation zone of the passive margin related to the oblique opening of the oceanic basin of the Aden Rift. The Hasik Graben (10 km wide and 30 km long) is bounded to the North and South by two master normal faults with a N45°E to N75°E trend and presents an axial dip towards the east (Figure 3.2) (Fournier *et al.*, 2004).

Several paleo-environments have characterised the deposition during the Tertiary period. Transgressive cycles with the deposition of shallow marine formations and regressive cycles evidenced by the deposition of gypsum began in the Late Palaeocene (60 Ma) and ended in the Late Eocene (38 Ma) (Roger *et al.*, 1989; Watchorn *et al.*, 1998).

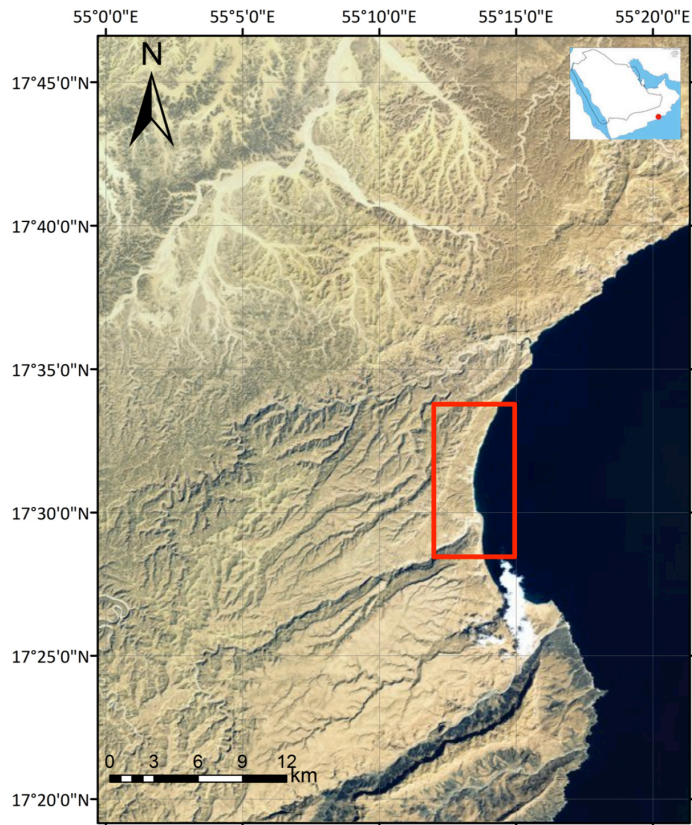


Figure 3.1 Geographic location of the study area.

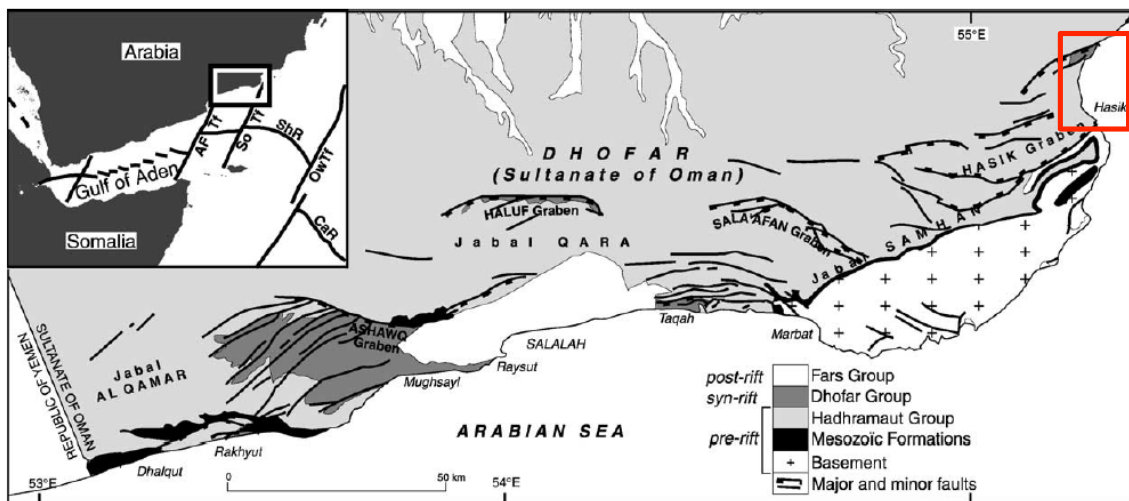


Figure 3.2 Structural map and sedimentary units of Southern Dhofar, Sultanate of Oman, derived and simplified from the 1/250,000 geological maps of Salalah and Hawf (Platel *et al.*, 1992; Roger *et al.*, 1992); in addition, the main structures of the Gulf of Aden and the on-land study area are present. Abbreviations are as follows: AF Tf: Alula–Fartak Transform Fault; So Tr: Socotra Transform Fault; Ow Tr: Owen Transform Fault; ShR: Sheba Ridge; CaR: Carlsberg Ridge. The red box identifies the study area (from Lepvrier *et al.*, 2002, mod.)

A carbonate succession up to 1000 m thick is exposed, characterised by three sedimentary groups (Platel & Roger, 1989; Roger *et al.*, 1989; Béchenec *et al.*, 1993; Robertson & Bamkhalif, 2001), which correspond to pre-rift, syn-rift and post-rift stages of deposition, the Hadhramaut, Dhofar and Fars groups, respectively. The study area is dominated by the Eocene series of the Hadhramaut group, whereas the Dhofar group (syn-rift) locally outcrops in the northern part of this sector. The post-rift Fars group, instead, does not outcrop in the study area and is restricted to the Salalah plain (Figure 3.2).

Focusing on the study area (Figure 3.3), the Hadhramaut group, which in turn overlies the Proterozoic basement (~800 Ma; Mercolli *et al.*, 2006), consists of carbonate units typical of shallow-water conditions, including the massive limestone of the Umm Er Radhuma Formation and the Rus Formations (up to 600 m thick, late Palaeocene/Thanetian - early Eocene/Ypresian), the Dammam formation (middle Eocene/Lutetian-Bartonian), consisting of yellow shale and chalky marl with interbedded argillaceous limestone (thickness 43 meters) and fine to medium grained creamy limestone, sometimes marly and chalky, nodular or dolomised (thickness approximately of 200 meters), and finally the Aydim formation (late Eocene/Priabonian), consisting of limestone, chalky marl and calcarenitic deposits characterised by rich macrofauna and banks of corals.

The syn-rift Dhofar group, unconformably deposited on the Hadhramaut group, consists of lacustrine limestone at the base (100 m), overlain by platform limestone (Ashawq Formation, 600 m), which passes laterally at the top to the overlying, chalky calci-turbidic deposits of the late Oligocene to early Miocene Mughsayl Formation (700 m thick beneath the Salalah plain; Platel *et al.*, 1992). The slope deposits of the Mughsayl Formation, which include megabreccia, debris flows, and olistolitic material transported from the adjoining shelf, result from the collapse and subsidence of the margin and correspond to deeper depositional environments.

After the Oligocene tectonic phase, a tectonic readjustment occurred in the Early Miocene so that the sedimentary package extended to the sea of the Kuria Muria Bay with a coastline of cliffs at different elevations, defined ridges tilting to the North-West, stacked as tumbled dominos one on top of another, creating overhangs and ledges (Ghezzi *et al.*, 2012).

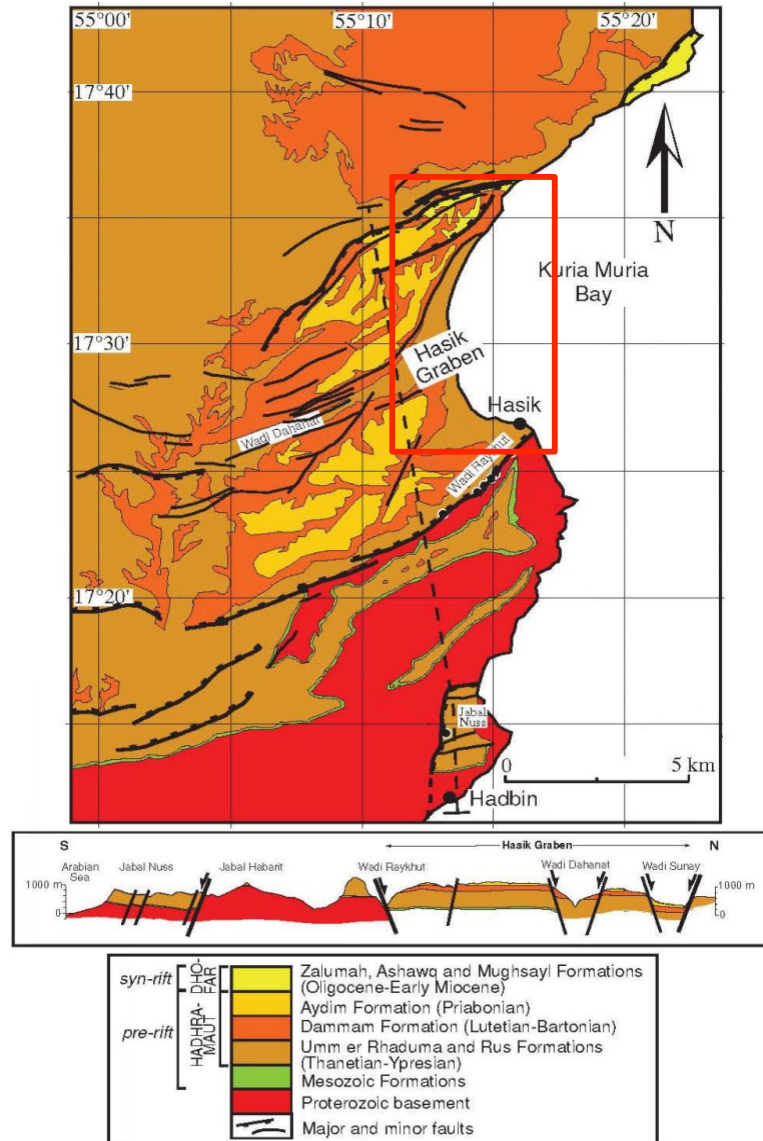


Figure 3.3 Geological map of the “Hasik Graben” area. The red box identifies the study area (from Fournier *et al.* 2004; modified).

At the end of the Early Miocene, the sedimentary conditions become similar to the present, in accordance with the general emersion of the South Arabian plate in that period. Thus, subsequent retrogressive-transgressive marine cycles of the Middle Miocene and the youngest of the Pliocene and Pleistocene combined with a possible late tectonic can be responsible for erosional and depositional phenomena involving the tertiary formations. Finally, not depicted on the map in Figure 3.3 for scale reasons, two quaternary terms outcrop, related to colluvial and alluvial deposits. The quaternary colluvium is particularly interesting for the objective of the present work because it is located on the coastal slope under investigation. It is composed of rock debris accumulated at the foot of the cliffs

caused by landslides below the fault scarps and consists of limestone blocks of up to 30 cubic meters in average size with marl and gypsum inside a silt matrix, extending towards the sea. The thickness is several tens of meters (more than 20 meters). The screes formation is still on-going from the Pleistocene. To conclude, there are also very thin (20-50 cm) alluvial deposits on the Wadi Dahanat floor consisting primarily of boulders emplaced during the last pluvial phase at the end of Pleistocene (Ghezzi *et al.*, 2012).

From the geomorphological perspective, the slope, which is primarily involved through the presence of the above-mentioned colluvial deposit, presents evidences of phenomena of past gravitational instability. According to Ghezzi *et al.*, (2012), these geomorphologic features seem linked to the following causes: i) different phases of the sea level in different eras caused some terraced planes located at different elevations. Consequently, the movement of the collapsed deposits increased, generating new collapses; and ii) the strong supply of sediments eroded by the Wadi Dahanat and its minor tributary are transported to the sea over time.

These characteristics are located particularly in the southern half of the study area, north of the mouth of the Wadi Dahanat. In the northern part of the sector under investigation, evidence of past instability processes involving the quaternary colluvium seem less severe; this can most likely be related to the decreased thickness of the colluvium layers (Ghezzi *et al.*, 2012).

During the period August 2011-June 2012, slope instability processes affected the area involved in the construction of the Hasik - Ash Shwaimiyah road. Because we were interested in the spatial and temporal evolution of the slope dynamics before the beginning of the construction, past information needed to be acquired about the slope under investigation. To reach this aim, InSAR-based techniques have been selected as the most effective for the presented purpose because they are the only techniques able to provide quantitative information on past ground displacements.

3.3. Multi-temporal DInSAR analyses

3.3.1. C-band archive SAR images

The SAR data archives contain very few images related to the study area. In particular, only four multi-temporal images acquired by the ERS-1 and ERS-2 satellites (European

Space Agency – ESA) between 1992 and 1996 were available in the ESA archive (Tab. 3.1). More recent data have been acquired by ESA using the Envisat satellite; however, the best interferometric stack reached only five scenes for the 2003-2004 period (Tab. 3.2).

Tab. 3.1 Available dataset acquired by ERS satellites

	Acquisition date (yyymmdd)	Satellite	Band (wavelength)	Orbital Geometry	Track
1	19920529	ERS-1	C (5.66 cm)	Descending	392
2	19930305	ERS-1			
3	19960422	ERS-2			
4	19960527	ERS-2			

Tab. 3.2 Available dataset acquired by Envisat satellite (ASAR sensor)

	Acquisition date (yyymmdd)	Satellite	Band (wavelength)	Orbital Geometry	Track
1	20030908	Envisat	C (5.62 cm)	Descending	392
2	20031013				
3	20031117				
4	20040510				
5	20040614				

3.3.2. L-band archive SAR images

More archival images have been acquired by the ALOS satellite (Advanced Land Observation Satellite) using the PALSAR sensor (Phased Array type L-band Synthetic Aperture Radar) and archived by JAXA (Japanese Aerospace Exploration Agency).

Nine images, acquired in the period between the end of 2006 and the middle of 2010, were available. We used 4 Fine Beam Single Polarisation (FBS, bandwidth: 28 MHz) images and 5 Fine Beam Double polarisation (FBD, bandwidth: 14 MHz) images. The pixel spacing of the fine beam single polarisation (FBS) data is 4.68 m in the range direction and 3.17 m in the azimuth direction, whereas the pixel spacing of the double polarisation (FBD) images is 9.36 m in the range direction by 3.17 m in the azimuth direction (Chen *et al.*, 2012) (Tab. 3.3). Using the same central frequency, the range bands of the FBS and

FBD images are fully overlapped. This allowed interferometric processing to be performed, combining FBS and FBD images in the same interferometric pair using the common HH polarisation (for this objective, the FBD data needed to be doubly oversampled in range to ensure the same resolution for all images used in the dataset (Chen *et al.*, 2014)).

Tab. 3.3 Available dataset acquired by ALOS satellite (PALSAR sensor)

	Acquisition date (yyyymmdd)	Satellite	Band (wavelength)	Orbital Geometry	Track
1	20061223	ALOS	L (23.6 cm)	Ascending	570
2	20070810				
3	20071226				
4	20080512				
5	20080627				
6	20090630				
7	20090815				
8	20091231				
9	20100402				

The primary difference between the data from the ESA satellites and those acquired by the ALOS PALSAR is represented by the different wavelengths. L-band SAR images from ALOS are characterised by much longer wavelengths (more than 23 cm), four times longer than the C-band data. Using longer wavelengths, the interferograms generated are characterised by higher spatial coherence. Decorrelation is much less severe for temporal, geometrical and atmospheric effects. The so-called “critical baseline” (namely, the value of the B_n above which an interferogram is totally decorrelated) is much higher (several kilometres) (Tab. 3.4). For this reason, a given data-stack whose normal baselines of image pairs are usually largely below this threshold can be fully exploited to obtain useful information.

The critical baseline is given by:

$$B_c = \frac{\lambda R \tan \theta}{2\Delta\rho}$$

where B_c is the critical baseline, λ is the sensor wavelength, R is the slant range distance from the satellite to the reflector on the Earth surface, θ is the incidence angle, and $\Delta\rho$ is the radar range resolution.

Moreover, the same consideration can be applied to the risk of losing information from SAR images acquired with long temporal baselines. Comparing C-band and L-band data, the latter appear considerably resilient to temporal decorrelation effects over the same areas, as quantitatively demonstrated by Wei & Sandwell (2010). Finally, it is notable that the available images belong to an ascending geometry stack and are thus able to provide more appropriate LOS orientation along the observed slope compared with that achievable by descending ERS and Envisat stacks, as illustrated below.

Tab. 3.4 Comparison between ERS/Envisat and ALOS PALSAR data (from Wei & Sandwell, 2010 mod.)

	ERS – Envisat	ALOS PALSAR
Wavelength	~ 56 mm	~ 236 mm
Altitude	790 km	700 km
Look angle*	23 degrees	34.3 degrees
Bandwidth	15.55 MHz	FBS: 28 MHz; FBD: 14 MHz
Critical Baseline	1.1 km	FBS: 13 km; FBD: 6.5 km

*Other look angles are available for ALOS, but 34.3 degrees is the main one

3.3.3. Analyses of archived SAR data

Regarding C-band images, with such a poor data stack, only a few differential interferograms could be computed, even assuming complete connection between the images to generate maximum redundancy of interferograms (images are connected to one another). In this case, considering $N(N - 1)/2$ interferograms to have a complete connection (where N is image number), we had only six and ten interferograms for the ERS and Envisat stacks, respectively (Figure 3.4). Moreover, most of the computed interferograms were characterised by long normal baselines (B_n), which negatively influence the spatial coherence.

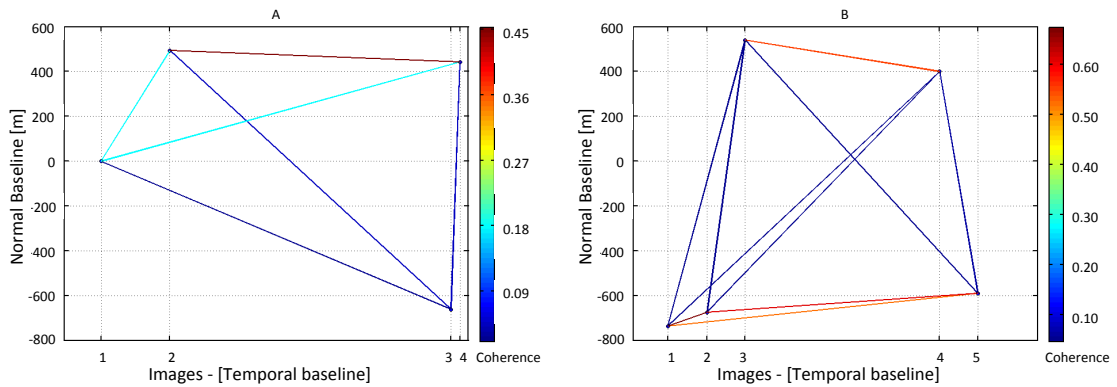


Figure 3.4 Graphs showing images connections related to ERS (A) and Envisat (B) data-stacks. Each dot represents an image in accordance with numeration of Tab. 3.1 and Tab. 3.2. Images are plotted in time (X axis) and space, represented by normal baseline (Y axis). Each line represents an interferogram. Colorbar is related to average spatial coherence of interferogram represented by the line connecting the two dots (i.e SAR images).

Most of the generated interferograms were extremely noisy, primarily because of geometrical decorrelation effects. For this reason, only one ERS and four Envisat interferograms were characterised by an acceptable coherence for the analysis of past displacements. Considering such conditions and the small quantity of available data, the application of A-DInSAR methods was not feasible. Moreover, the analysis of differential interferograms characterised by higher spatial coherence was insufficient to detect and measure the presence of displacements during the period of investigation.

Furthermore, both the ERS and Envisat datasets were acquired along descending orbital paths so that the LOS was characterised by a stronger component perpendicular to the slope under investigation (i.e., the worst condition under which to observe possible displacements along the slope direction) (Figure 3.5).

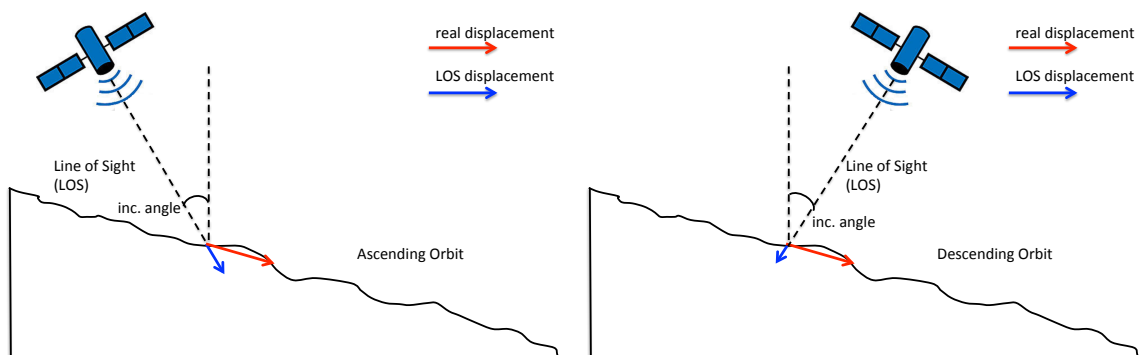


Figure 3.5 Difference between ascending (left) and descending (right) orbits to observe displacements over the studied slope.

With the L-band SAR signal (23.6 cm wavelength) and the greater number of available images, the interferometric results were significantly better than those attained from the C-band data processing (ERS and Envisat). However, even the ALOS PALSAR stack with its potentially high coherent interferograms contains few images, insufficient to perform reliable A-DInSAR analyses. To attain good information from such images, a DInSAR-based approach was adopted, starting from single interferograms. Considering a complete image connection graph (to generate high redundancy), 36 interferograms were created, coupling all images to each other. As can be observed in Figure 3.6, using the L-band signal, very highly coherent interferograms have been obtained, even with the high temporal and normal baselines, compared with those in Figure 3.4. Furthermore, the topographic phase has been subtracted (using an available 20 m resolution DEM), thus providing 36 Differential Interferograms that allowed for the observation of the displacement phase contributions.

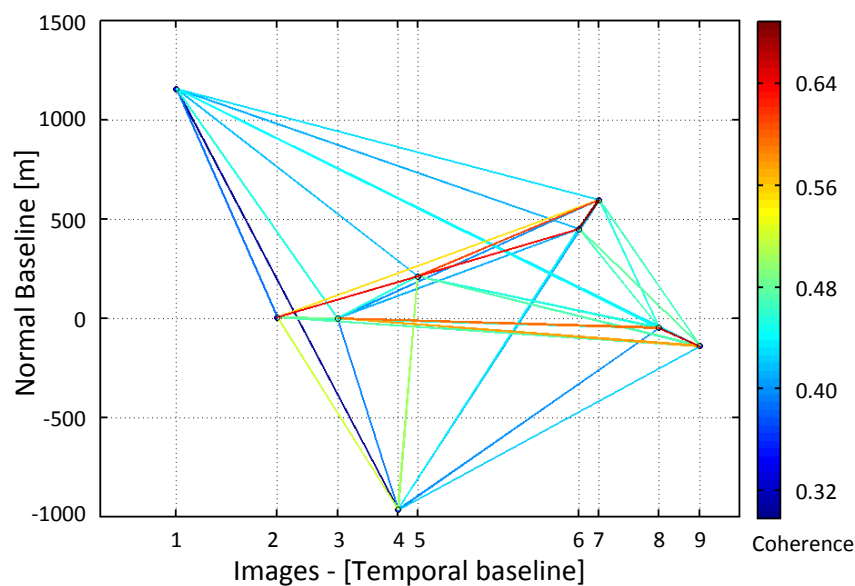


Figure 3.6 Graphs showing image connections related to ALOS PALSAR data-stack. Each dot represents an image in accordance with numeration of Tab. 3.3. Images are plotted in time (X axis) and space, represented by normal baseline (Y axis). Each line represents an interferogram. Colorbar is related to average spatial coherence of interferogram represented by the line connecting the two dots (i.e SAR images).

Because no A-DInSAR analysis was feasible and the area was relatively small, we performed a manual analysis of the best interferograms. The first step to attain reliable results regarding displacement occurrences was the detection and subtraction of the residual topographic component on differential interferograms. In this case, the residual

heights have been estimated using a multi-image approach, more specifically, the Quasi-Persistent Scatterers (QPS) method (Perissin & Wang, 2012). Using the QPS approach (see par. 2.5.1), a sub-selection of points characterised by a very high and stable backscattering signal has been selected, thus estimating the phase related to the residual heights, exploiting all generated interferograms and weighing such pixels on the basis of their spatial coherence value. Local height information, derived from InSAR data, has been used to refine the original DEM to remove this re-estimated topographic component from the newly generated interferograms.

Tab. 3.5 ALOS PALSAR interferograms used for the investigation of past displacements.

ID	Master-Slave	Temporal baseline [days]	Normal baseline [m]
1	20061223-20070810	230	1151
2	20061223-20071226	368	1155
3	20061223-20090630	920	706
4	20061223-20090815	966	560
5	20061223-20091231	1104	1205
6	20061223-20100402	1196	1295
7	20070810-20071226	138	3
8	20070810-20080512	276	970
9	20070810-20080627	322	206
10	20070810-20091231	874	53
11	20070810-20100402	966	143
12	20071226-20080627	184	209
13	20071226-20090630	552	449
14	20071226-20090815	598	595
15	20071226-20091231	736	50
16	20071226-20100402	828	140
17	20080512-20091231	598	916
18	20080627-20090630	368	240
19	20080627-20091231	552	259
20	20080627-20100402	644	349
21	20090630-20090815	46	146
22	20090630-20100402	276	589
23	20090815-20100402	230	735
24	20091231-20100402	92	89

Starting from this redundant dataset, a quality threshold based on a spatial coherence value (>0.5) has been applied, thereby selecting the 24 best interferograms to perform the displacement investigation. In Tab. 3.5, the interferograms used for the further investigation stages are listed. Clearly, despite the selection performed to keep only the

best interferograms, no images have been discarded, and all of them have been used to provide the highest possible temporal coverage.

3.4. Interferometric results

The 24 differential interferograms shown in Tab. 3.5 have been analysed to investigate the interferometric signals to detect and quantify any possible displacements.

We removed the topography as finely as possible using the QPS approach. However, a small residual topographic component may persist. To distinguish and separate that component from the displacement component, a criterion based on a double check was applied:

- i) The phase signal related to the topography is proportional to B_n ; thus, if a given interferometric feature varies proportionally with B_n , it is reasonable to assume that it is due to residual topography;
- ii) Once a given interferometric signal is hypothesised to be in relation with the displacement, it is possible to observe the persistence of the signal using the redundant interferograms because the signal should be temporally congruent with the interferogram data-set, generated by crossing all images. This also aided in understanding the time interval when the displacement processes occurred.

The examination of such interferograms allowed for the detection of some interferometric features (identified as “anomalies”) recursively present in some of them. Such anomalies, whose presence along the interferometric set was apparently random, have been properly interpreted by applying the principles described above. In this way, it was possible to detect three small areas of the investigated slope that were characterised by interferometric features that can be interpreted as displacements that occurred within the examined period. By ordering the interferograms temporally (with the master images sorted in temporally ascending order) and also considering the B_n values, it was possible to identify the interferometric features related to the displacements by discarding those related to the topographic residual phase; moreover, it was possible to define the time interval when the detected displacements occurred.

The three small areas are localized in Figure 3.7, and they are related to portions of the geocoded wrapped interferograms shown in Figure 3.8, Figure 3.9 and Figure 3.10. Once a given interferometric feature was identified (red boxes inside the figures), it was “tracked”

on all of the interferograms, marking those where it appeared. The first analysis of the detected phase signals was to distinguish the residual topographic features from the displacements. To attain this objective, as explained above, we checked the presence/absence of such anomalies in relation to the B_n values. As you can see, the presence of these anomalies is not directly linked to B_n ; interferograms 1, 2, 8, 22 and 23 in Figure 3.8, Figure 3.9 and Figure 3.10 are characterised by large baseline values, but they do not show the presence of such anomalies. In contrast, the detected phase signals are present in the other interferograms independently of B_n ; for example, for all areas, interferograms 10 and 15 are characterised by the above-mentioned anomalies, even with small values of B_n .



Figure 3.7 Localization of three small areas affected by instability processes detected by ALOS PALSAR interferograms.

This approach allowed for the definition of these phase signals due to displacements. Red borders surrounding some figures in Figure 3.8, Figure 3.9 and Figure 3.10 identify interferograms with phase signals caused by displacements.

To confirm this deduction, selected interferograms have also been interpreted from a temporal point of view. In this perspective, redundant use of SAR images allowed the observation of the temporal congruency of the interferometric signals. Because the data

used for this analysis are simple wrapped differential interferograms, atmospheric artefacts, decorrelation effects and general noise could still be present. For this reason, the use of the same image for several interferograms reduces the risk of losing information, which could be masked by such disturbances affecting any single image. Furthermore, as explained in section 3.4, the use of the same SAR image in more than one interferogram has also been crucial in defining with reliable accuracy the time interval when the detected processes occurred.

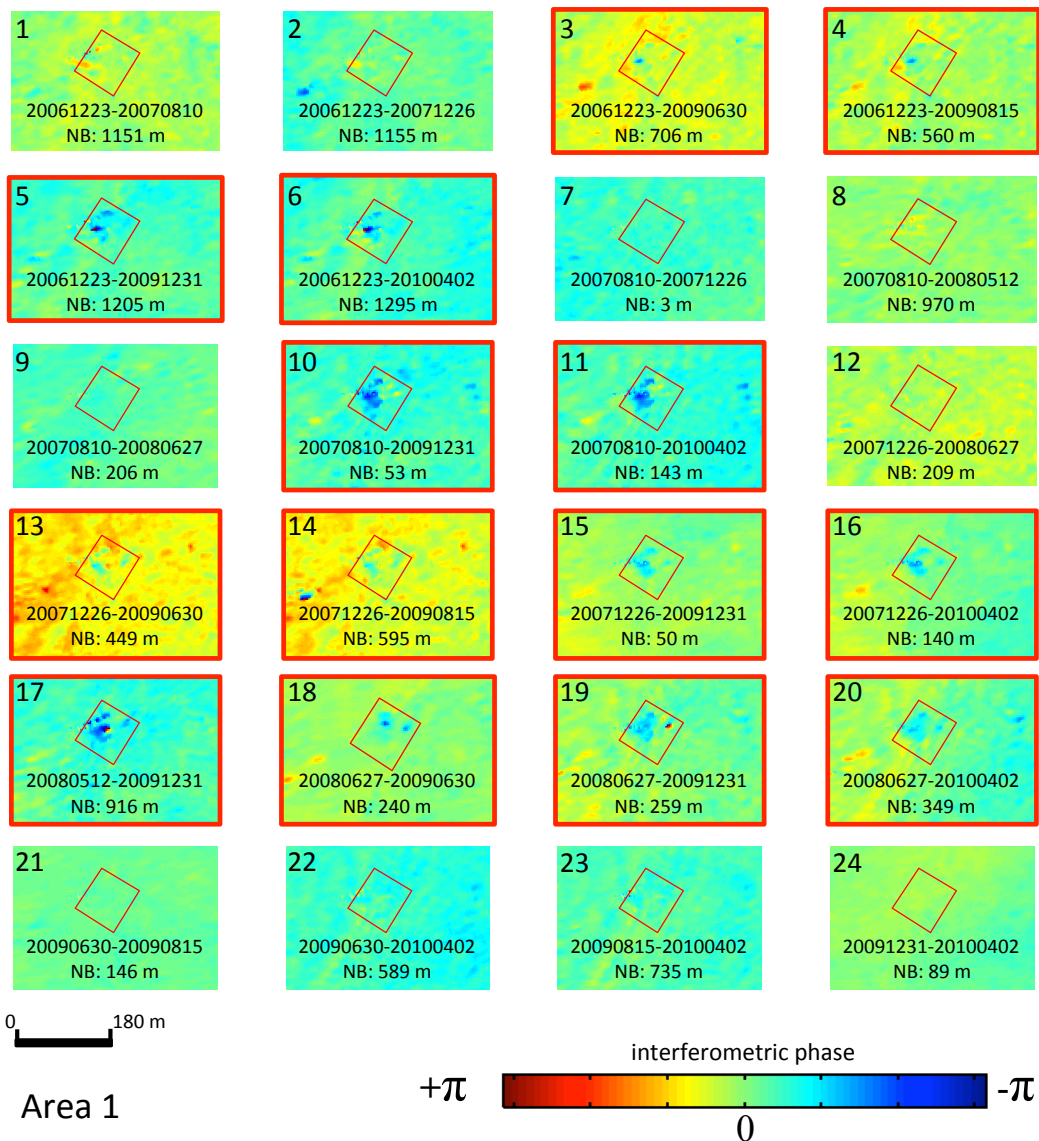


Figure 3.8 Interferometric anomaly detected in the area 1 (inside red boxes). The red bounds indicate the presence of anomaly, interpreted as displacements, in the given interferogram.

In Tab. 3.6, all interferograms used for phase signal analysis and interpretation are reported as crosses between available images. Dark grey cells indicate an interferogram discarded because of the coherence below the threshold value; light grey cells indicate a null interferogram (i.e., master and slave images are the same); green cells indicate the absence of a phase signal related to a displacement; and red cells represent a displacement detected in the three areas where interferometric anomalies have been recognised. This graphic representation also helps to temporally define the instability phenomena, which occurred in a well-identified time interval between June 27th 2008 and June 30th 2009.

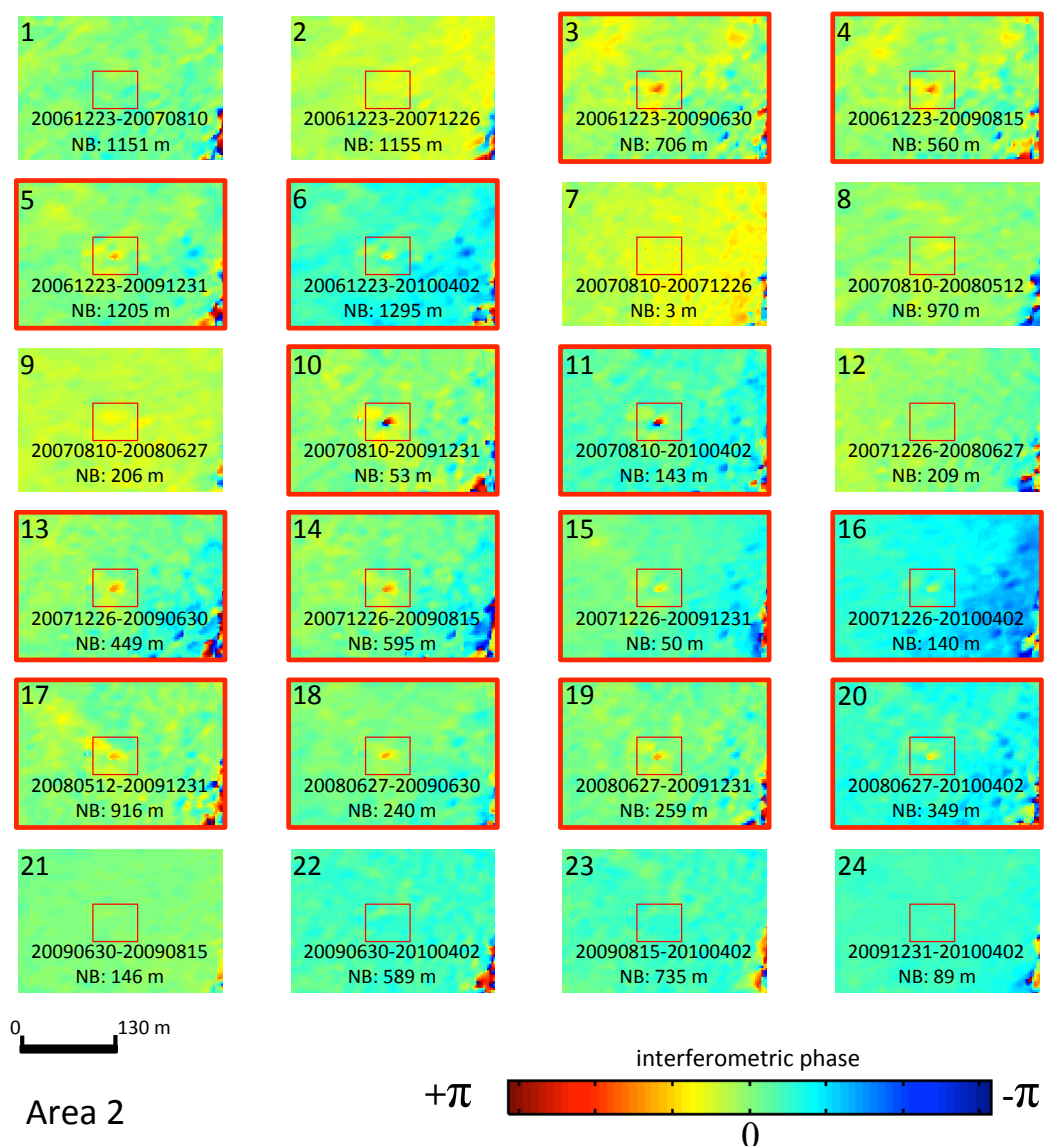


Figure 3.9 Interferometric anomaly detected in the area 2 (inside red boxes). The red bounds indicate the presence of anomaly, interpreted as displacements, in the given interferogram.

None of the generated interferograms computed by pairing images acquired before June 27th, 2008 show any anomalies that may be related to displacements. The same results is obtained for images acquired after that date. However, by pairing images acquired before and after this date, we obtained interferograms characterised by the presence of observable displacements in the phase signal. These results are confirmed by all of the interferograms computed by using all possible combinations. Therefore, in the time interval between June 2008 and June 2009, some instability processes occurred in the three identified areas.

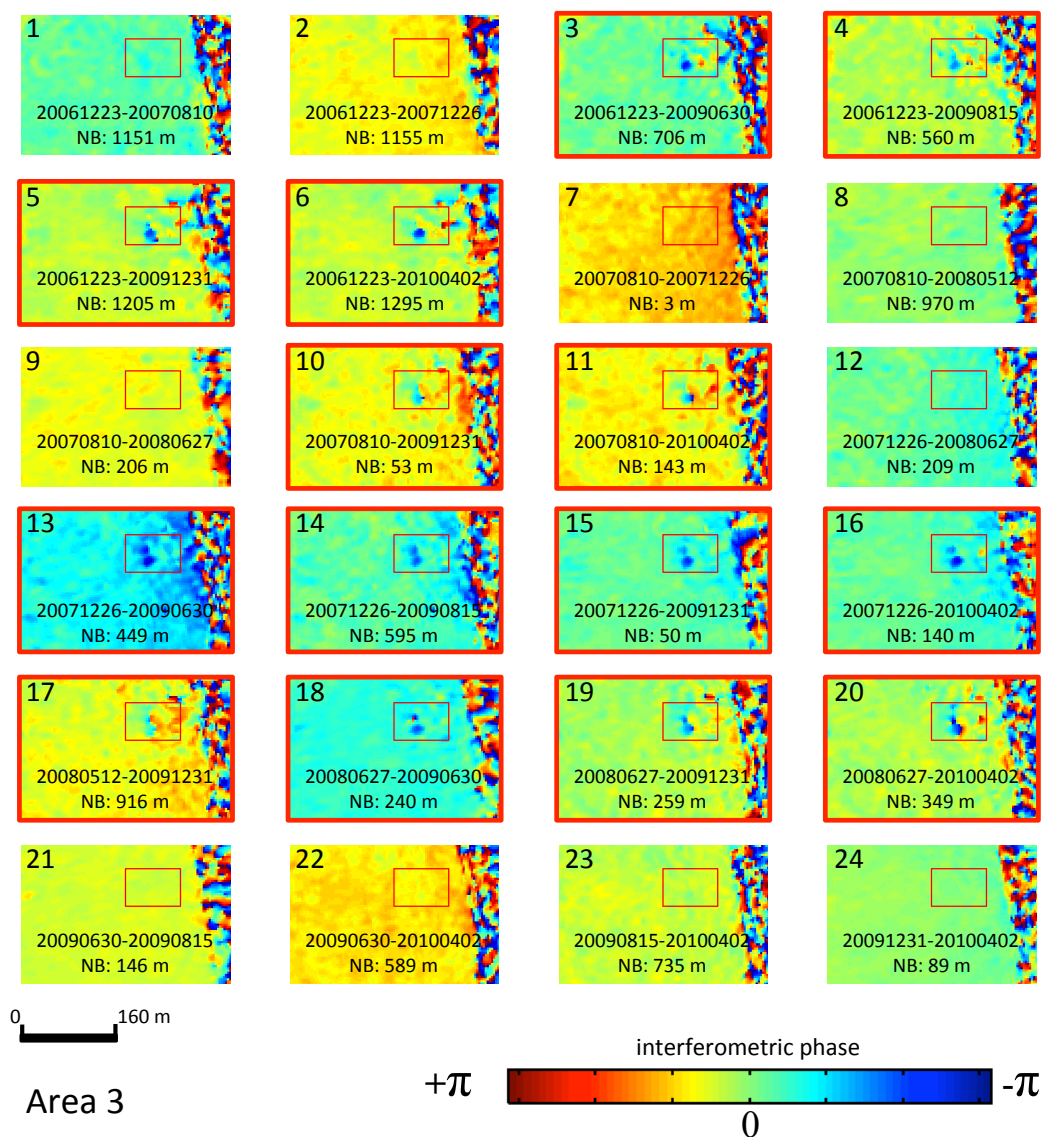





Figure 3.10 Interferometric anomaly detected in the area 3 (inside red boxes). The red bounds indicate the presence of anomaly, interpreted as displacements, in the given interferogram. The belt with casual coloured pattern on the right is due to the sea surface, which is characterized by null coherence.

Tab. 3.6 Temporal distribution of detected interferometric anomalies along interferograms time series. Green boxes identify absence of anomalies; red boxes identify presence of anomalies; dark grey boxes identify discarded interferograms in accordance with Tab. 3.5. Light grey boxes identify null interferograms because of coincidence between master and slave images.

		SLAVE IMAGES								
		20061223	20070810	20071226	20080512	20080627	20090630	20090815	20091231	20100402
MASTER IMAGES	20061223	Light grey	Green	Green	Dark grey	Dark grey	Red	Red	Red	Red
	20070810	Light grey	Light grey	Green	Green	Green	Dark grey	Dark grey	Red	Red
	20071226	Light grey	Light grey	Light grey	Dark grey	Green	Red	Red	Red	Red
	20080512	Light grey	Light grey	Light grey	Light grey	Dark grey	Dark grey	Dark grey	Red	Dark grey
	20080627	Light grey	Light grey	Light grey	Light grey	Light grey	Red	Dark grey	Red	Red
	20090630	Light grey	Light grey	Light grey	Light grey	Light grey	Light grey	Green	Dark grey	Green
	20090815	Light grey	Light grey	Light grey	Light grey	Light grey	Light grey	Light grey	Dark grey	Green
	20091231	Light grey	Light grey	Light grey	Light grey	Light grey	Light grey	Light grey	Light grey	Green
	20100402	Light grey	Light grey	Light grey	Light grey	Light grey	Light grey	Light grey	Light grey	Light grey

		
Absence of interferometric features related to displacements	Presence of interferometric features related to displacements	Discarded interferogram for low coherence

Considering the results shown in Figure 3.8, Figure 3.9 and Figure 3.10, the phase signals can be considered to quantitatively estimate detected displacements starting from the angular values of the wrapped phase. Because the PALSAR sensor operates with a 236 mm wavelength (Tab. 3.4), the maximum detectable phase difference (equal to 2π and represented by the transition from red to blue colour in the interferograms) corresponds to a displacement equal to $\lambda/2$ (118 mm) along the LOS. Using the very high coherence attained, these weak, small and localised indications of movements were clear enough to be quantitatively estimated. The interferometric phase difference between the anomalies and the surrounding pixels has been considered. Area 1 (Figure 3.8), in the northern part of the study area, is approximately 90x70 m, located near the tectonic line coincident with the coastal rock cliff. Considering all of the analysed interferograms, a 40-45 mm LOS displacement away from the satellite was detected. Area 2 (Figure 3.9), smaller than the previous area, is very localised (approximately 40x40 m), showing slightly smaller displacements (approximately 30 mm along the LOS). In this case, the displacements are in the direction away from the satellite. Area 3 (approximately 50x50 m) is very near the

coast and is located on a portion of the slope involved in the landslide that occurred in the period August 2011-June 2012. Because of the small dimensions of the area affected by displacements in the period under investigation and because the detected displacements are very small (approximately 35 mm along the LOS in the direction away from the satellite), it is not possible to directly relate the previously observed displacements with the wider instability process that affected the slope in 2011-2012.

3.5. Discussion

The methodology used to investigate past displacements for the present case study is based on a classical approach of SAR interferometry, which is the direct examination of computed interferograms. Many automated algorithms to extract information from SAR data-stacks exist; however, they are likely not capable of achieving the results herein shown. A-DInSAR methods could not provide trustable and reliable results by using such poor data-stacks, especially in the very difficult conditions of this case, with very small displacements circumscribed in restricted areas, the presence of non-linear displacements, low temporal image frequency, and the absence of further supporting information. Detailed work manually analysing phase signal contributions through a slope-oriented approach allowed us to extract more information than expected from the available data.

We began by manually distinguishing the topographic components from the displacement phase contributions. It could be argued that the height estimation (to refine the DEM used to compute the differential interferograms) was partially performed using automated methods, but that was not the case for the displacement estimation. This is because also with the few available images, the estimation of heights remains a linear problem dependent on the normal baseline and thus more easily accomplished. In contrast, the estimation of displacements is much more controlled by the number of images.

The low temporal resolution of the available dataset did not allow better definition of the temporal development of the detected phenomena; thus, we have to accept a 1-year approximation for such events. Furthermore, we do not know if the detected displacements developed as single, impulsive events, or if they are the result of slow processes that developed over a longer period (several weeks or months). At the timescale of the adopted dataset, the detected displacements can be considered “impulsive” because they were not

distributed throughout the entire period of the images. In addition, for this reason, such phenomena would most likely not be detected by an automated A-DInSAR analysis, even with a larger dataset.

The use of the L-band data, acquired by the ALOS PALSAR satellite, also played a key role in the attainment of the results. In addition to the advantages in terms of the high coherence discussed in section 3.3.3, the use of these data has the additional advantage of being less dependent on phase ambiguity due to high, rapid displacements. In such circumstances, with displacements that occurred in a time interval not covered by many images, or with rapid, impulsive movements, the risk of losing information due to wavelength limits was very high. Other data, such as C-band (wavelength: ~ 56 mm) or even X-band (wavelength: ~ 30 mm) data, which are more affected by phase ambiguity problems, would most likely not be able to provide such information with $\lambda/2$ values equal to ~ 28 mm and ~ 15 mm, respectively.

3.6. Conclusions

The evolution of instability processes affecting a coastal slope in the Sultanate of Oman has been defined by using satellite SAR interferometry. Thanks to archive data provided by the Japanese ALOS PALSAR satellite, an investigation based on the combination of DInSAR and QPS techniques allowed us to achieve quantitative results about surface displacements occurred within the time-span covered by the SAR images (December 2006-April 2010).

The approach used in this work allowed us to overcome the limitation caused by the limited number of images in the area, which was not sufficient to perform A-DInSAR analyses. The QPS method has been used to obtain a more accurate DEM to better discriminate the displacement phase signal from the topographic information.

A manual interpretation of the generated interferograms has been carried out to properly observe the occurred displacements. The application of an automated algorithm, in fact, could easily disguise them because they were not continuous in space and time. More specifically, the used approach was carried out by analysing temporal (i.e. acquisition dates of the images) and geometrical (i.e. normal baseline) parameters characterising all interferograms that were computed with the highest possible redundancy. The phase signals related to displacement detected in the interferograms have been analysed in terms

of their relation with the normal baseline and the congruency with their temporal distribution along the whole dataset.

The slope instability processes have been defined in time (occurrence between June 2008-June 2009), and the related displacements have been quantitatively estimated. The proposed approach demonstrates the capability to derive information about past displacements by satellite SAR images also in case when advanced interferometric techniques are not feasible due to the limited number of images in the dataset. Therefore, it can be considered a useful investigative solution also in remote and not urbanized areas where a limited knowledge on geomorphological and geological settings is available and where monitoring data about past evolution of displacement phenomena do not exist. It can also provide an early prior indication that can be deepened during in-situ investigations related to major construction on large areas.

Acknowledgments:

The present work has been carried out thanks to the European Space Agency in the framework of the Cat-1 project “Landslides forecasting analysis by time series displacement derived from Satellite and Terrestrial InSAR data” (Id 9099) and Rocksoil S.p.A., which provided basic geological data.

4. EXTENSIVE A-DINSAR AND GEOMORPHOLOGICAL STUDY OF LANDSLIDES EVOLUTION: BASIN-SCALE AND SINGLE PROCESSES INVESTIGATION

4.1. Introduction

In the last 40 years, much work has been completed to develop and apply several mapping techniques to well represent the distribution and features of slope movements. This is typically a many-sided issue and is affected by several factors, such as the availability of the diagnostic data, the scale of the analyses and the final objective of the performed investigation (Varnes, 1974, 1984; Rockaway, 1976; Parise, 2001; Guzzetti *et al.*, 2012). A suitable cartographic representation of landslide phenomena is the first step in addressing such a hazard for a given area. Depending on the final use, several types of landslide mapping can be performed, such as landslide inventory, landslide typology and landslide state of activity maps. When this work is performed only heuristically (i.e., based on the expertise and knowledge of terrain conditions of a geomorphologist), it can be partially affected by some limitations of the data used (e.g., airborne optical images, which are a very common tool in this field).

If a landslide inventory map represents a snapshot of the territory at a given moment (Parise, 2001), i.e., the date of the air photo dataset or field surveys, a state of activity map requires assumptions about the spatial and, especially, temporal evolution of the given processes. Therefore, data that provide quantitative evidence about displacements that have occurred represent a valuable source of information for state of activity assessments.

Recently, the contribution of remote sensing techniques to natural hazards risk reduction has dramatically increased. Satellite InSAR, in particular, has proven to be a reliable methodology to study ground deformations, and today, it can be applied both in monitoring and to attain information related to a given area or specific deformation processes (Massonnet *et al.*, 1993; Kampes 2006; Lauknes & Shanker 2010; Bozzano & Rocca, 2012).

Satellite Advanced Differential Synthetic Aperture Radar Interferometry (A-DInSAR), namely Persistent Scatterers Interferometry (PSI), Small Baseline Subset (SBAS) and similar techniques (Ferretti *et al.*, 2001; Berardino *et al.*, 2002; Perissin & Wang, 2012) have greatly increased the range of research and monitoring applications since their

development in the early 2000s. Because of the increased practical fruition of the results provided by such techniques, A-DInSAR is becoming a reality today and is performed not only by scientific experts but also by professionals involved in natural hazards management and large infrastructure. This important objective is also directly related to the ease of integration of A-DInSAR results with data obtained by classical monitoring and investigation techniques. The possibility provided, for example, by PSI has led to the development of radar-interpretation (Farina *et al.*, 2007; Cigna *et al.*, 2011), which allowed the management of ground deformation process issues (landslides, in particular) with a new information source. Furthermore, satellite InSAR is able to provide results about past ground displacements. This specific feature causes InSAR (and A-DInSAR techniques in particular) to be a valuable technique for attaining information for ground deformation estimation in a quantitative sense and for wide areas. At present, such results are not achievable with comparable accuracy using any other techniques.

As noted by other authors (Cigna *et al.*, 2011), InSAR data need to be integrated with other investigation techniques and prior information to take advantage of this tool. Field surveys and interpretation of aerial photos and other monitoring data (both ground based and remote sensing) are useful not only to properly interpret InSAR results but also to attain basic information about the investigated area to design suitable InSAR analyses (Notti *et al.*, 2010; Mazzanti *et al.*, 2011; Strozzi, *et al.*, 2013; Akbarimehr *et al.*, 2013).

A study area in central Italy has been investigated in-depth to define the spatial and temporal evolution of landslides. The area is affected by many landslide processes, characterised by different features in terms of size, typology, orientation and direction of movements. However, most of these processes have proven to be suitable for being studied by selected techniques also because their typical velocity of deformation is not too high to be observed by satellite A-DInSAR. In this case study, the key role played by conventional and non-conventional A-DInSAR analyses is discussed. Moreover, a combination of several remote sensing and field survey investigations has been performed for more complete and comprehensive landslide mapping. Furthermore, the extensive use of A-DInSAR results allowed us to define in detail the local kinematics of some landslide phenomena in time and space.

4.2. The study site

The investigated area (approximately 20 km²) is located in the eastern sector of the central Apennines, near the villages of Casacanditella, Filetto and San Martino sulla Marrucina (Abruzzi region, Italy) (Figure 4.1). The area is situated in the Periadriatic zone facing the Maiella relief (approximately 20 km from the Adriatic coast). It is a typically hilly area with N-S-trending valley floors, incised by the Dendalo and Vesola San Martino streams, with absolute heights ranging between approximately 460 m above sea level (a.s.l.) on the surrounding hills and 150 m a.s.l. on the stream floor, thus generating, on average, moderate slope energy.



Figure 4.1 Geographical location of the study area

4.2.1. Geological-structural characteristics

From a structural standpoint, the investigated area lies along the outer margin of the Apennine chain (Bigi *et al.*, 1997), slightly west of the Ortona-Roccamonfina line (Di Bucci & Tozzi, 1992). This roughly NNE-SSW-trending alignment is the zone of junction between the two large arcs forming the Apennine thrust-and-fold belt system (Mostardini & Merlini, 1986; Di Bucci & Tozzi, 1992; Patacca & Scandone, 2007). The chain thus

consists of wide E-dipping thrust sheets and thrusting calcareous lithotypes over arenaceous-clayey deposits (Miccadei, 1993; Scisciani *et al.*, 2001).

In the investigated area, the bedrock is composed of a thick marine succession of the upper Pliocene-Pleistocene p.p., known in the literature as the Mutignano Formation (Cantalamesa *et al.* 1986; Bigi *et al.* 1997; Calamita *et al.* 2002). In its lower part, the succession holds grey-blue marly clays, often interbedded with sands that become increasingly frequent and thick moving upwards. In its upper part, it contains grey and ochre silty sands, with pelitic levels and occasional arenaceous and conglomeratic intercalations.

Fluvial and lagoonal deposits of Pleistocene p.p.-upper Pleistocene p.p. age occur along the top portions of reliefs and near morphological terraces (Demangeot, 1965; Fanucci *et al.*, 1996; Farabollini & Nisio, 1997). These deposits embed polygenic conglomerates in a sandy-silty groundmass, with local sandy layers and clayey and peaty intercalations.

Extensive Holocene fluvial and detrital-colluvial deposits are observed along fluvial incisions and slopes (Demangeot, 1965; Fanucci *et al.*, 1996). These terrains consist of clayey-silty and sandy-silty deposits, frequently evolving into gravels and pebbles or cobbles.

Structurally, the investigated area has numerous high-angle normal and strike-slip faults (Miccadei, 1993; Bigi *et al.*, 1997; Calamita *et al.*, 2002), clearly dislocating the bedrock lithotypes. These faults, covering a small surface area, have throws of metres to tens of metres. The primary fault systems have approximately N-S, E-W, SW-NE, SE-NW and SSE-NNW directions (Bigi *et al.*, 1997; Currado & Fredi, 2000), although non-systematic faults with different orientations are also found. The above described tectonic features progressively downthrow the Mutignano Formation towards the main valley floors. Finally, the formation has a generally monoclinial and gently NE-dipping pattern, and its strata have an inclination of 5° to 15° (Figure 4.2).

4.2.2. Geomorphological characteristics

The geomorphology of the Periadriatic sector of Abruzzi is strongly controlled by its local geological-structural setting and by the recent evolution of the Apennine chain (Demangeot, 1965; Centamore *et al.*, 1997). The above-mentioned tectonic features govern the configuration of the leading drainage lines and morphological ridges of the investigated

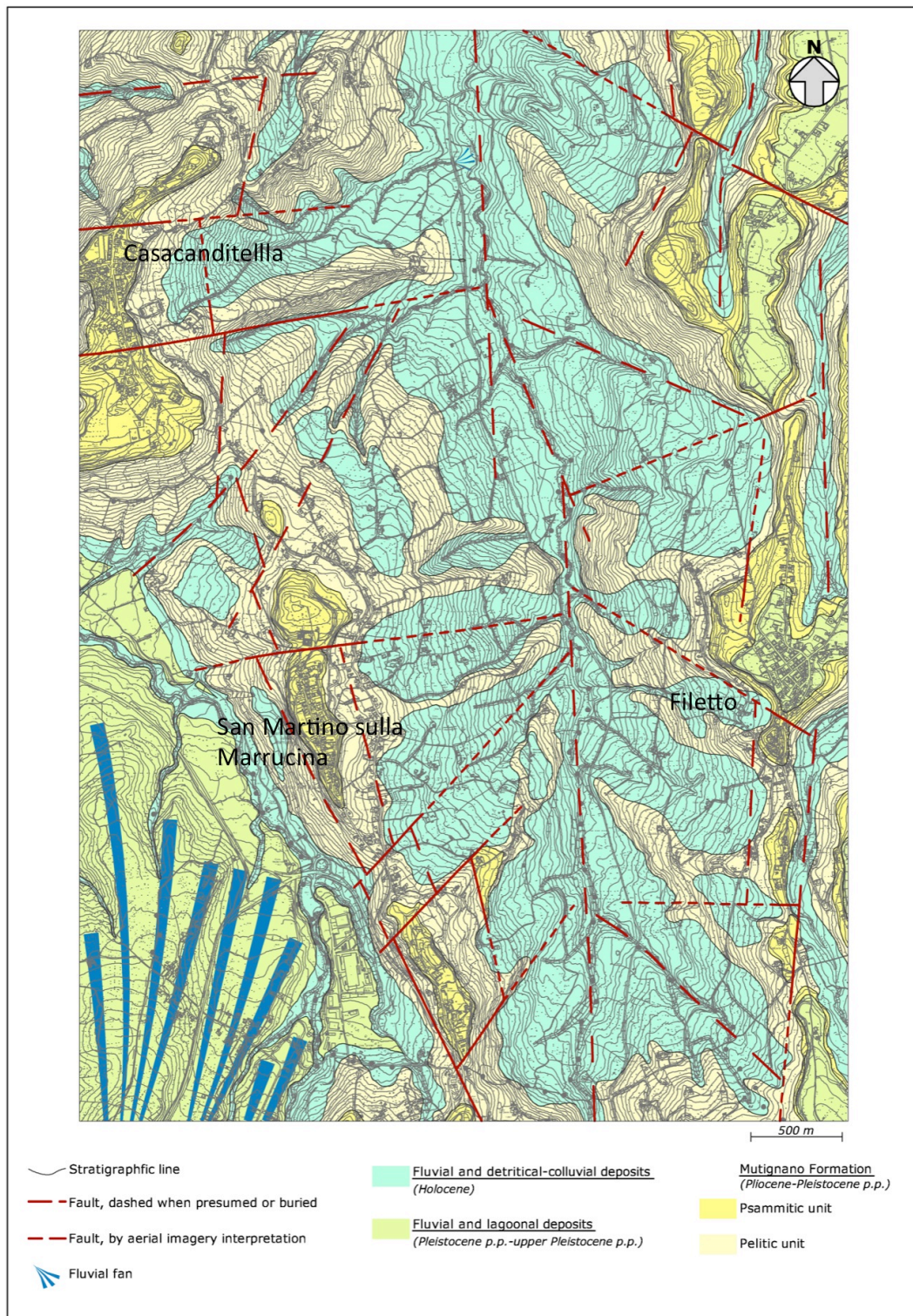


Figure 4.2 Geological map of the study area

area (Bigi *et al.*, 1995; Farabollini & Nisio, 1997). In particular, the shaping of the reliefs and the geomorphological evolution of this sector of the region are largely dependent on slope movements (D'Alessandro & Pantaleone, 1987; Buccolini *et al.*, 1994; Centamore *et al.*, 1997).

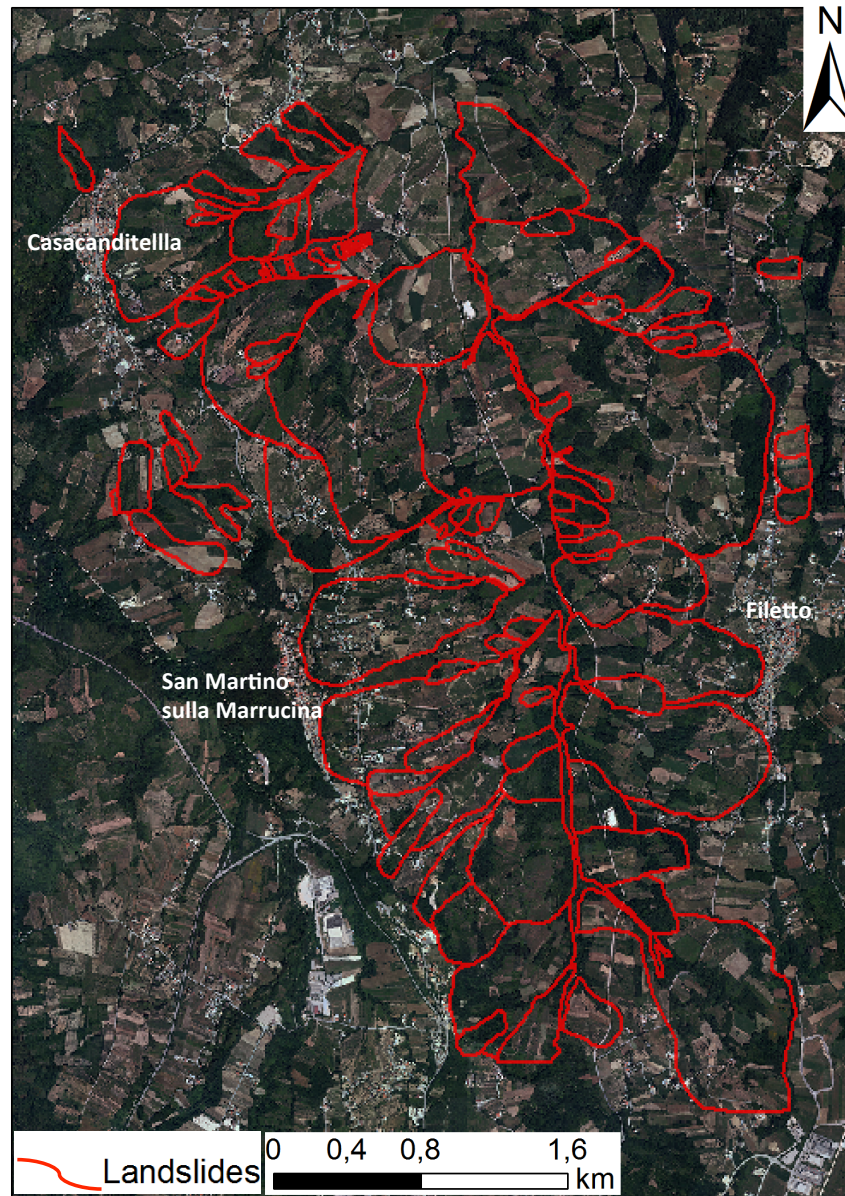


Figure 4.3 Red polygons show mapped landslides from aerial photos interpretation and geomorphological field surveys

The investigated area is affected by a large number of landslides and slope deformations (Buccolini *et al.*, 1994), especially reaching the Dendalo stream valley floor (Figure 4.3).

These processes originate from various geological and geomorphological factors (i.e., tectonic features, soil characteristics, surface water dynamics, land uses, and seismicity). In this scenario, slope instabilities generally arise along tectonic lines and in surface erosion areas (D'Alessandro & Pantaleone, 1987; D'Alessandro *et al.*, 2003). The distribution and features of landslides are directly related to the geology of the area and to its high-angle tectonic lines (D'Alessandro *et al.*, 2003). Indeed, these lines act as kinematic releases for unstable masses, which follow their direction in the detachment areas or along the sides of the masses being deformed. Conversely, the pattern of the rupture surface in the intermediate-low sectors of the landslide bodies depends on the setting layout of the bedrock. Furthermore, landslide typologies are of course influenced by outcropping terms. Because of the presence of different types of soils, primarily characterised by the presence of silty sands and pelitic terms generally belonging to the Mutignano Formation, the typical instability processes detected in the study area can be classified as slides, earth-flows and complex landslides.

4.3. Landslide mapping

4.3.1. Methods

A detailed mapping of landslides was performed using geomorphological field surveys and the interpretation multi-temporal aerial photos. The primary objective was to properly define a landslide inventory for the study area, characterising each detected phenomena in terms of landslide typology and the state of activity related to more recently available data. Using a multi-temporal dataset, the spatial and temporal evolution of the detected slope instability process has been defined.

The interpretation of multi-temporal aerial photos has been performed to define the morphological features and evolution of the detected landslides. Analyses have been performed on four datasets related to different periods: 1954 (Average Scale 1:33,000), 1987 (A.S. 1:33,000), 2002 (A.S. 1:13,000), and 2007 (A.S. 1:5,000). Stereoscopic analyses of image pairs allowed for the mapping of the main landslide bodies as well as geomorphological and hydrographical features that are also related to the temporal morpho-evolution of the active processes in the area.

The multi-temporal interpretation analysis was complicated by the complex geomorphological structure of the area and the characteristics of the different datasets. Therefore, it was not always possible to identify and map all geomorphological elements.

4.3.2. Results

An analysis of aerial photos from 1954 to 2002 combined with field surveys allowed us to identify and map 97 landslides within the study area. Landslides affect most of this portion of the Dendalo stream basin and were classified as slides (15 processes), earth-flows (41 processes) and complex mass movements (41 processes) (*sensu* Varnes, 1978) (Figure 4.4).

In general, the multi-temporal aerial photos analyses showed the presence of current slope instability phenomena since 1954, indicating that the detected landslides are pre-existing and, in many cases, quite old. These phenomena could be placed into the context of the complex geological, structural and geomorphological conditions of the area, and they are not directly connected with human activities in the area in recent decades.

The landslide deposits are related to the mobilisation of the pelitic and psammitic lithologies of the Mutignano Formation, especially on the middle and lower portions of the slopes. In the mainly pelitic areas, the geomorphological elements related to the largest landslide phenomena, such as niches, scarps and counterslopes, are highly altered and degraded and often modified by the strong anthropic activity in the area. Landslide areas range from a few hundreds of square metres to several square kilometres. The slides and complex landslides are the widest and deepest phenomena, with failure surfaces often in the range of several tens of metres. Conversely, the earthflows are less wide and deep, and their mobilised masses have a thickness of several metres.

Displacement mechanisms are well identified using landslide crowns patterns (usually evident even if partially affected by deterioration), the presence of clear counterslopes and landslide terraces. The detected phenomena are primarily characterised as complex, wide landslide systems, in which it is not always possible to identify and bound individual instability phenomena. Finally, local processes related to viscous deformation of coverage (creep and/or solifluction) affect the steeper slopes or portions of slopes near the landslide areas. The evolution rates of the processes are generally limited because the identified landslides show moderate signs of reactivation and not always visible at the scale of the analysis.

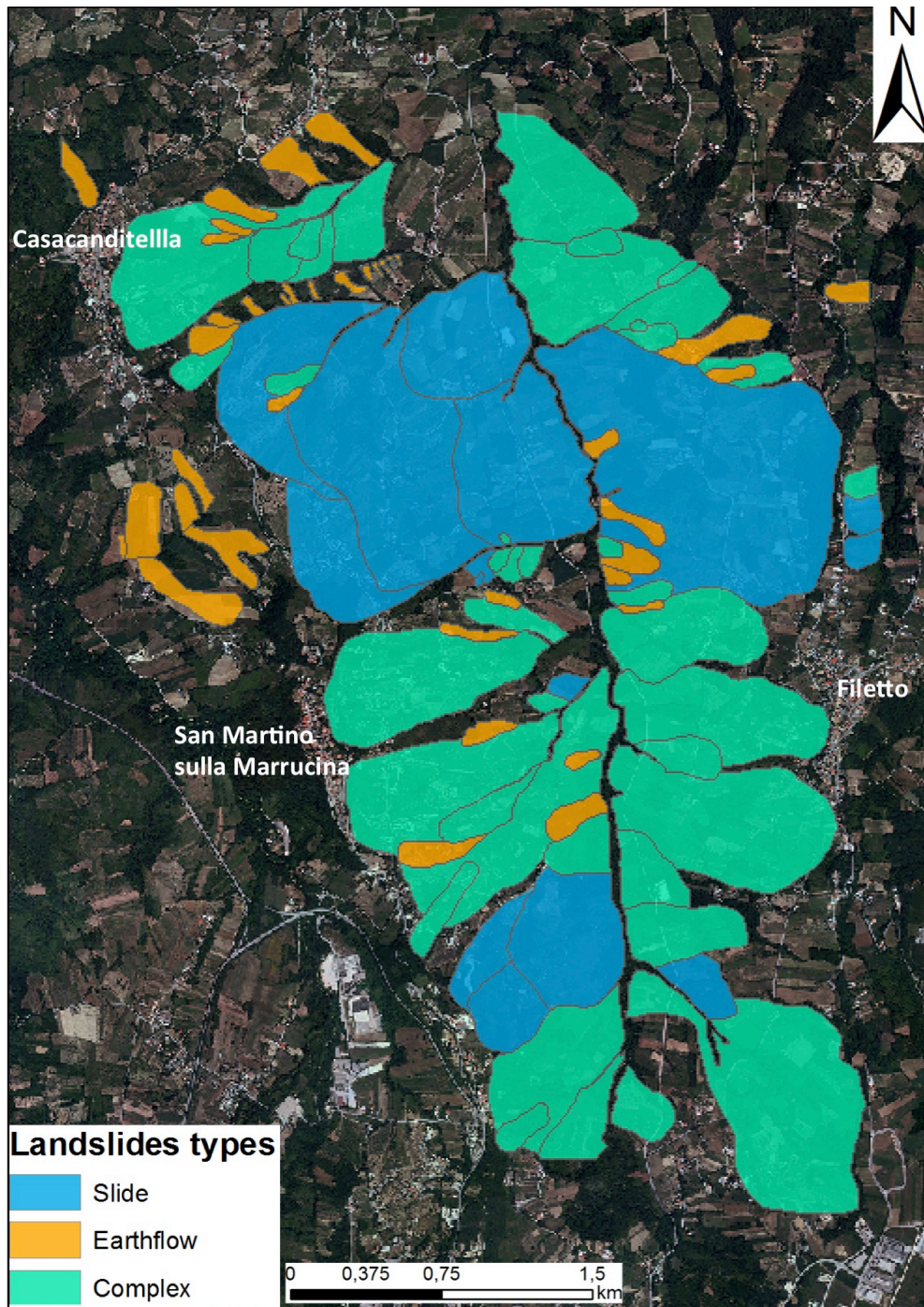


Figure 4.4 Landslides mapped in the study area, divided in accordance to Cruden & Varnes classification (1996).

Based on these investigation methods, the state of activity appears to be generally dormant, with a return time of a few years to some tens of years. The stabilised phenomena are

represented by very extensive landslide movements along the Dendalo stream valley floor. Using field surveys and multi-temporal aerial photos, we could detect some active

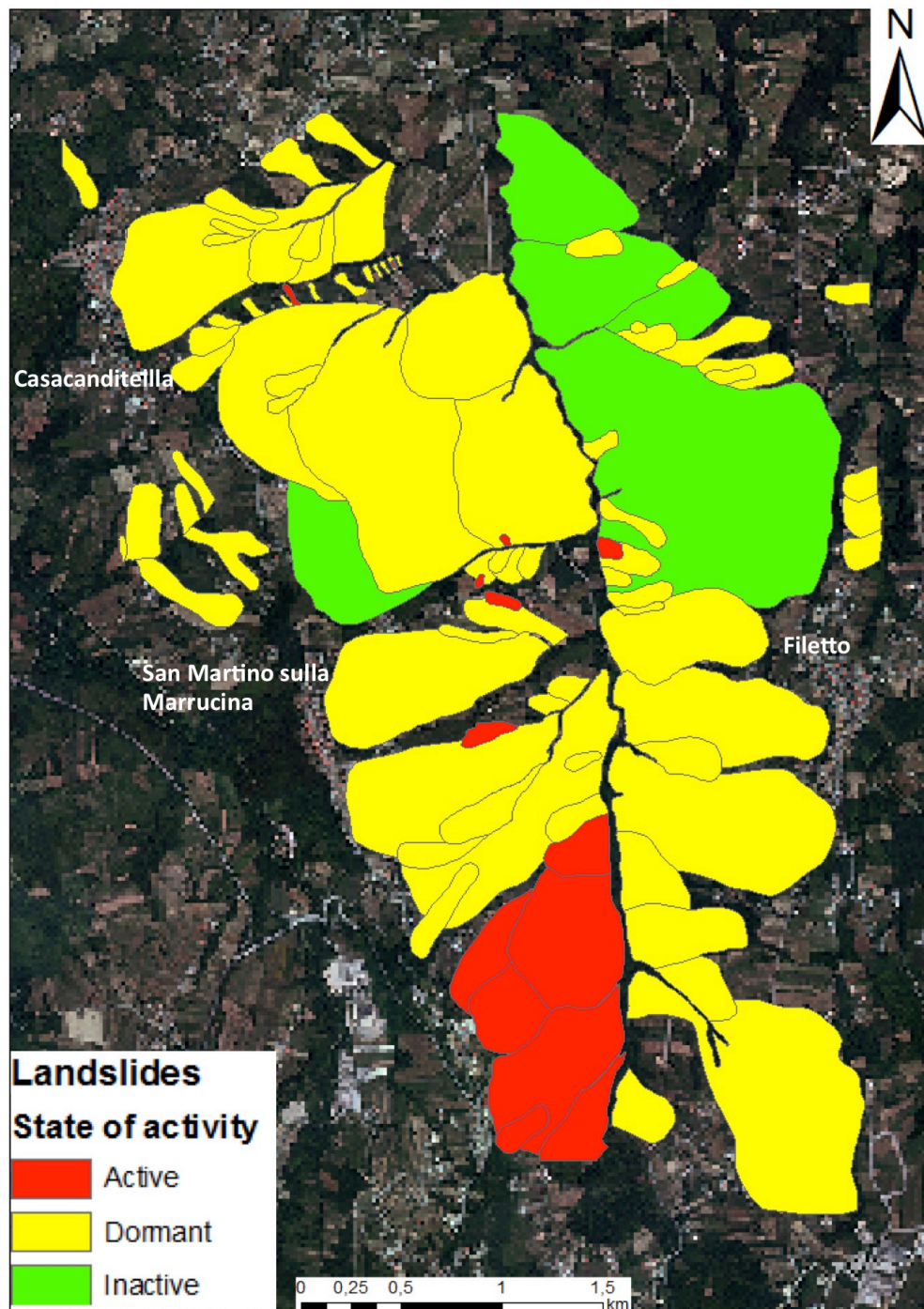


Figure 4.5 Landslide state of activity deduced by geomorphological elements observed by aerial photos interpretation and field surveys.

or suspended phenomena, represented by some fairly shallow landslides and by the system of slides and complex slides occurring SE of the village of San Martino sulla Marrucina

(Figure 4.5). Their stage of activity is generally advanced or senile, exhausted only for the inactive and more ancient phenomena. The distribution of activity is mostly constant or retrogressive and rarely multidirectional.

4.4. A-DInSAR analyses

Information about the temporal and spatial evolution of landslide processes (landslide mapping, spatial evolution, state of activity) attained using multi-temporal aerial photos represents the first stage of a large-scale slope instability investigation (Canuti & Focardi 1986; Gonzalez-Diez *et al.*, 1999; Guzzetti *et al.*, 1999; Parise & Wasowski, 1999; Wieczorek, 1984).

However, this widely used methodology has several limitations: i) it is strongly discontinuous in time (the availability of data depends on the presence of archived aerial photos acquired in the same area over time); ii) as in our case study, datasets are often heterogeneous in terms of spatial scales as well as film type (the availability of black and white and colour photos); iii) the definition of the states of activity of several processes are directly related to the presence of geomorphic elements (this aspect is crucial if anthropic activities such as agriculture occur in given area); iv) the identification of diagnostic elements is strongly affected by operator subjectivity; v) the results are only partially quantitative and not highly accurate (Cigna *et al.*, 2012).

To define in detail the deformational behaviours of slopes in the study area, we performed some A-DInSAR analyses. The primary objective was to improve the knowledge of the spatial and temporal evolution of landslide processes attained from the interpretation of multi-temporal aerial photos.

4.4.1. Basic principles and applications

Over the last two decades, classical DInSAR analyses, performed by coupling SAR images to generate differential interferograms (i.e., interferograms after the removal of topographic contributions derived from an external Digital Elevation Model – DEM), have been largely adopted as a tool to investigate ground deformation processes.

Using this technique, two complex SAR images acquired over the same area allow the detection and measurement of deformation processes that have occurred during the time interval between acquisitions, using information carried by the phase signal characterising

every pixel value. DInSAR has proven to be a very useful methodology to analyse several ground deformation phenomena, such as coseismic and postseismic deformations (Massonnet *et al.*, 1993, 1994), volcanic deformation processes (Massonnet *et al.*, 1995), and ice and glacier dynamics (Goldstein *et al.*, 1993, Kwok & Fahnestock, 1996). Landslide processes have also been studied using the DInSAR technique (Strozzi *et al.*, 2005, 2010; García-Davalillo *et al.*, 2014, Jebur *et al.*, 2013). However, several limitations affect this technique. First, we have to consider the presence of the atmosphere phase screen (APS), which is related to signal delay effects induced by atmospheric variations during the images acquisition period. Other sources of errors are the presence of residual topographic contributions, which can affect the phase signal, and decorrelation effects (both temporal and geometrical), which can prevent the observation of displacement information or reduce the accuracy of the results.

Advanced DInSAR (A-DInSAR) techniques have been developed over recent years as an effective solution to overcome the above limitations of standard DInSAR analysis (Ferretti *et al.* 2001, 2011; Berardino *et al.*, 2002, Hooper *et al.*, 2004, Lauknes, 2004; Kampes, 2006, Van Leijen & Hanssen, 2007, Perissin *et al.* 2008, 2012). All of these approaches are basically characterised by the exploitation of large, multi-temporal data-stacks to generate several interferograms, thus achieving higher redundancy of interferometric results. The approaches used can primarily be grouped into two categories: SBAS (Small Baseline Subset) approaches, in which interferograms are generated by coupling SAR images on the basis of the temporal and normal baselines characteristics, and Persistent Scatterers Interferometry (PSI) approaches, based on the selection of pixels within the SAR images with high, stable radar backscattering responses over time. These so-called Persistent Scatterers (PS) are generally represented by points characterised by high coherence over long time intervals (Ferretti *et al.*, 2001; Hooper *et al.*, 2004; Kampes, 2006). Generally, constructed structures, such as buildings, bridges, dams, railways, or pylons, or natural elements, such as outcropping rocks or homogeneous terrain areas, can represent good PSs. Unlike the SBAS approach, standard PSI is based on the generation of interferograms using a common master SAR image. Point-like scattering pixels remain coherent for the entire observation period, and they do not suffer from temporal and geometrical decorrelation effects, thus also allowing the generation of interferograms using image pairs characterised by long temporal and normal baselines. Using this principle, almost all

images that constitute a given stack can be used to perform multi-temporal A-DInSAR analyses. The latter point is crucial for the investigation of past displacements because, in this case, information can be attained only from archived SAR data, and it is fundamental to not waste the possible contributions of any SAR acquisition. Every image contributing to an A-DInSAR analysis represents “one sample” in a given time series of displacement. For some deformation phenomena, such as landslides, it is very important to attain as detailed a time series as possible. From this perspective, PSI and other A-DInSAR techniques not only represent methodologies that can overcome the typical limitations of DInSAR but also an opportunity to fully take advantage of SAR data archived by national and international Space Agencies, that since 1992, thanks to European Remote Sensing (ERS1) mission by European Space Agency (ESA), quite regularly started to collect data on several areas worldwide, so creating a valuable archive for present and future investigation related to past displacements.

However, PSI and other A-DInSAR techniques are affected by some limitations. First, because only objects which are good “radar reflectors” can be analysed, they have an inability to attain information over highly vegetated areas. This aspect is not secondary as landslides often involve non-urban areas, and, if any corner reflector had been installed, there is no way to overcome this issue for past-oriented A-DInSAR analyses. Moreover, because of the cyclic nature of the phase signal, it is not possible to observe very rapid displacements. More specifically, there is a strong dependence on SAR sensor wavelength (λ) and revisit time; in particular, if no prior information is available, it is not possible to measure displacements faster than $\lambda/4$ between two consecutive SAR acquisitions (14 mm for A-DInSAR analysis performed using ERS and Envisat archived SAR data from ESA, which are in the C band with a wavelength of ≈ 56 mm) (Ferretti *et al.*, 2005). Furthermore, satellite SAR interferometry is affected by the capability of observing displacements only along the so-called Line of Sight (LOS), which is the sensor-target direction. This has many consequences: first, it is difficult to observe displacements as they diverge from the direction parallel to the LOS (displacements which are perpendicular to the latter are not observable). However, the possibility of combining PSI results attained from ascending and descending orbital geometric data acquired over the same area allows the derivation of vertical and horizontal (nearly East-West) movement directions. In contrast, the North-South horizontal component is not detectable, and indeed the system sensitivity to this

direction is too low because it is almost parallel to the orbital path (Colesanti & Wasowski, 2006).

4.4.2. A-DInSAR data processing

For the present case study, we performed A-DInSAR analyses of past displacements using four SAR data-stacks from the ESA archive ranging from 1992 to 2010. More specifically, ERS1/2 data were selected for the 1992-2001 period, and Envisat data were selected for the 2002-2010 period. Large-scale analyses have been performed on a portion of the SAR images frame (approximately 11x11 km) covering an area greater than the study area. For both periods, we analysed both ascending and descending datasets. In this case, because of the N-S oriented basin, we had to contend with the east and west aspects of the slopes; thus, to properly observe the possible displacements on all slopes, we had to select datasets acquired in ascending and descending orbital geometries (Tab. 1). Moreover, an external DEM (resolution of 30x30 m) was used to compute the differential interferograms (i.e., to subtract the topographic phase component from the interferometric phase) and to geocode the PS results.

Tab. 4.1 Archived data stacks selected for the A–DInSAR analyses

Satellite sensor	ERS Descending	ERS Ascending	Envisat Descending	Envisat Ascending
Used images	71	47	47	54
Covered period	Jun. 1992 - Jan. 2001	Jun. 1995 - Dec. 2000	Nov. 2002 – Sep. 2009	Feb. 2003 – Sep. 2010
Master	June 26, 1997	June 16, 1998	August 18, 2005	October 18, 2006

We performed the interferometric analyses using Sarproz (Perissin *et al.*, 2011), which was specifically developed for multi-image InSAR analyses, such as PS (Ferretti *et al.*, 2001) and QuasiPS (QPS) (Perissin & Wang, 2012). Two primary approaches have been applied: large area analyses over the entire study area and local scale analyses for selected landslide processes. The former was performed to attain more general information for the refinement of landslide mapping and assessment of the past state of activity. Small area (or local scale) analyses were otherwise performed to increase knowledge of single process dynamics.

For every dataset, all images have been related to a single master image; more specifically, the selected masters are reported in Table 4.1. The master image has been selected by considering the normal and temporal baselines to reduce decorrelation effects. Once all slave images have been co-registered to the master image, the reflectivity map (i.e., the multi-temporal amplitude value for each pixel) and the amplitude stability index (ASI) have been generated:

$$ASI = \left(1 - \frac{\sigma}{\mu}\right)$$

where σ and μ are, respectively, the standard deviation and the mean of amplitude for every pixel throughout the multi-image data stack. ASI has been used as a quality estimator for the selection of PS candidates (PSC) in the PSI procedure.

The proper multi-image interferometric analysis has been performed with a combined technique, based on PS and QPS (Perissin & Wang, 2012) integration. In particular, this hybrid approach is performed by taking advantage of two different image connection graphs used for the different methodologies. As is standard for the PS method, the so-called “star” graph has been used (Figure 4.6A), thus connecting all slave images to a single master image to generate interferograms. This connection is based on a temporal continuity and improves the capability of unwrapping the phase signal to generate a reliable displacement time series. Moreover, by using the QPS method (Perissin & Wang, 2012), we also connected the same images using the Minimum Spanning Tree (MST), which is a weighted graph to connect images to maximise spatial coherence (Figure 4.6B). Interferograms obtained from the images connected in this way may provide wider information if compared with those computed starting from the star graph because of the higher number of coherent scatterers.

The interferometric phase signal, $\Delta\varphi_{int}$, is the result of multiple contributions. For the sake of simplicity, we here indicate only the following terms:

$$\Delta\varphi_{int} = \Delta\varphi_{topo} + \Delta\varphi_{displ} + \Delta\varphi_{atmo} + \Delta\varphi_{noise}$$

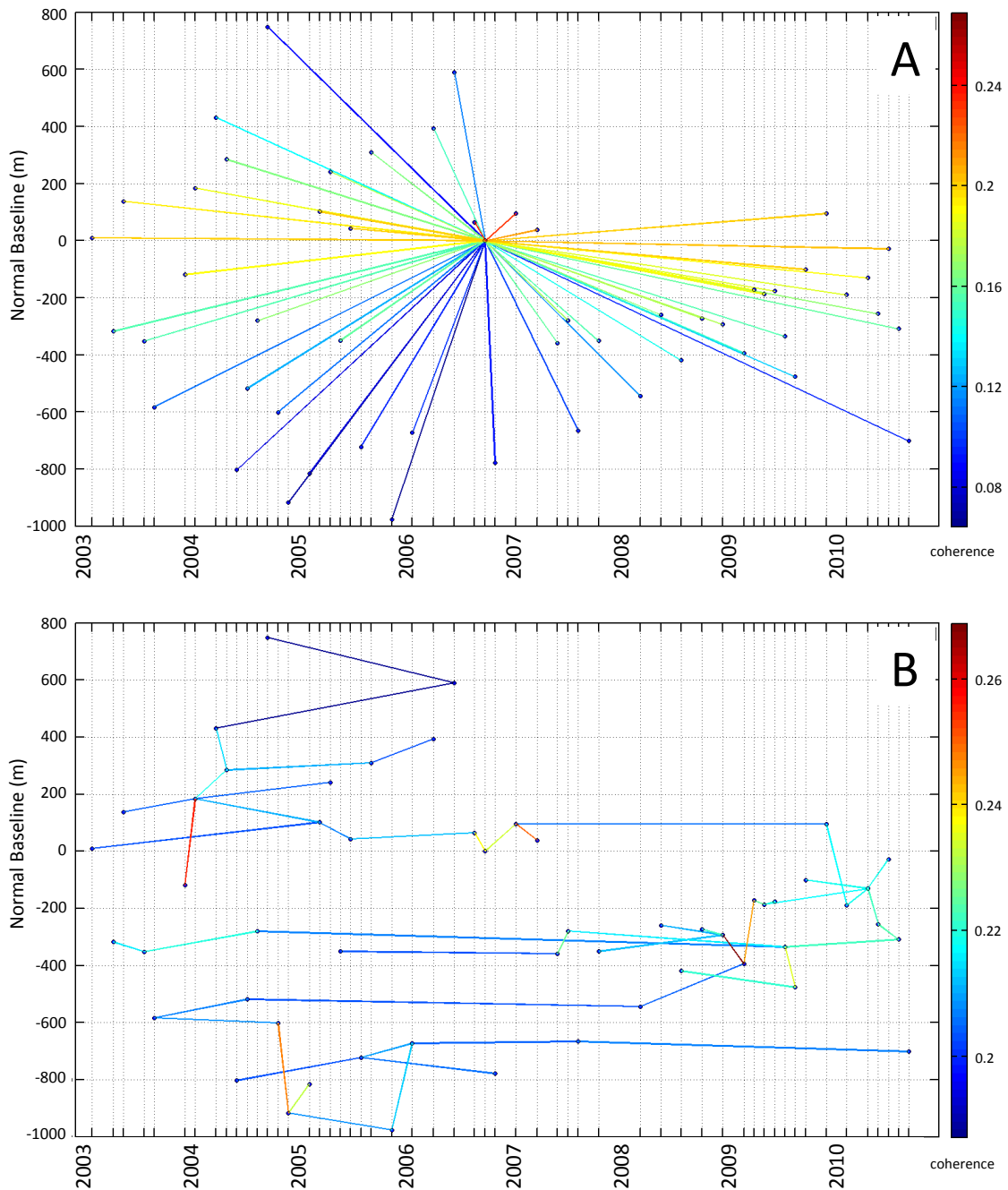


Figure 4.6 Graphs used to connect images relating to temporal baseline (X axis) and normal baseline (Y axis). Every dot represents an image, while every line represents an interferogram. Colours from blue to red show increasing value of spatial coherence. It is worth noticing different values of spatial coherence achievable from 'star' graph (A) and Minimum Spanning Tree (MST) graph (B), respectively. In particular minimum values, are considerable higher for MST graph. The example is referred to the Envisat descending dataset.

where $\Delta\phi_{\text{topo}}$ is the contribution of the residual topographic height (H) after DEM subtraction from interferograms, $\Delta\phi_{\text{displ}}$ is the searched displacement (D) information, $\Delta\phi_{\text{atmo}}$ is the disturbance caused by the atmospheric phase screen (APS), and $\Delta\phi_{\text{noise}}$ is the

non-removable phase disturbance. To properly estimate the displacement (D) and the topographic height (H) values, we selected a set of PS candidates (PSC) using an ASI threshold to choose very stable pixels in terms of the amplitude signal over the analysed period.

All PSCs were then connected to create a redundant network, and H and D were estimated along the connections starting from a linear model to infer unknown displacement. Once we found H and D values for every connection, those values were integrated over the PSCs to estimate the APSs (one for every used image) starting from the residual phase components. Once the APSs have been attained, a second step of parameter estimation is performed on a much larger set of points, which will represent the final step of the PSs after a final temporal coherence threshold.

In addition to the large-scale analyses described above, we also performed some “small area” analyses focused on specific portions of the study area. Our objective was to improve the knowledge of the deformation processes of specific landslides. The primary differences related from the previous methodology are i) neglecting APS because of the smaller area under investigation; in areas less than $\approx 1 \text{ km}^2$, we can assume that the atmospheric effects are homogeneous (Hanssen, 2005) (this avoids the risk of displacement information being wrongly estimated as atmospheric disturbance); ii) the non-linear behaviour of deformation (acceleration and deceleration), which is crucial for properly describing the landslide processes, can often be disregarded by automated analyses. Here we want to stress that a deeper investigation is required to analyse and interpret the interferometric results, and sometimes this may be attained only by manually exploring time series and, when necessary, reprocessing them with slightly different parameters.

4.4.3. A-DInSAR results

In Figure 4.7, the A-DInSAR results are related to the ERS and Envisat periods. PSs are shown as coloured dots. Colours are related to displacement rates (mm/year) along the LOS. Dots from yellow to red show displacements away from the satellite, and dots from light blue to dark blue indicate displacements towards the satellite. Green dots represent stable points. Red polygons indicate landslide bodies mapped through the interpretation of aerial photos and field surveys as in Figure 4.3.

The A-DInSAR results cover 27 landslides of the total of 97 affecting the study area (less than 30% of the number of phenomena). However, it is worth noticing that such landslides are very large and cover more than 80% of the surface affected by instability processes within the study area. The landslides not covered by the PS results are mainly represented by small and very small earthflows located in secondary valleys, where no buildings or other structures as potential good radar targets are present.

We want to focus mainly on specific portions within the entire study area. First, due to local morphological and geological features, the main urbanised areas are settled on hilltops, offering many good scatterers as potential PSs (also because the local incidence angle of the satellite sensors was not affected by geometrical distortions on these almost flat areas). Starting from interpretation of aerial photos and field surveys, we knew that almost all detected landslide processes seemed not to affect such villages. This information was also confirmed by the A-DInSAR results, which primarily show stable PSs over the urbanised areas (see ellipses A, B and C in Figure 4.7).

Moving down from hilltops, the slopes degrade gently to the streams. Especially on the western slopes, many PSs showing displacement are present in both the ascending and descending geometries. Because of the availability of the multi-temporal archive data (here, both aerial photos and satellite SAR), the evolution of the state of activity of the detected landslides has been assessed. As stated above (par. 4.3.2), starting from the analyses of the airborne optical images and field surveys, a given state of activity has been assumed for each landslide (Figure 4.5) based on geomorphological criteria. Several field surveys have been performed to evaluate the state of activity, and very similar results were attained in 2010, 2011 and 2012, suggesting a very slow displacement pattern for landslides characterised as “dormant”. Furthermore, using the ERS and Envisat A-DInSAR results, which provided quantitative data (i.e., the detection of targets affected by displacements), the landslide state of activity for the two analysed periods has been assessed.

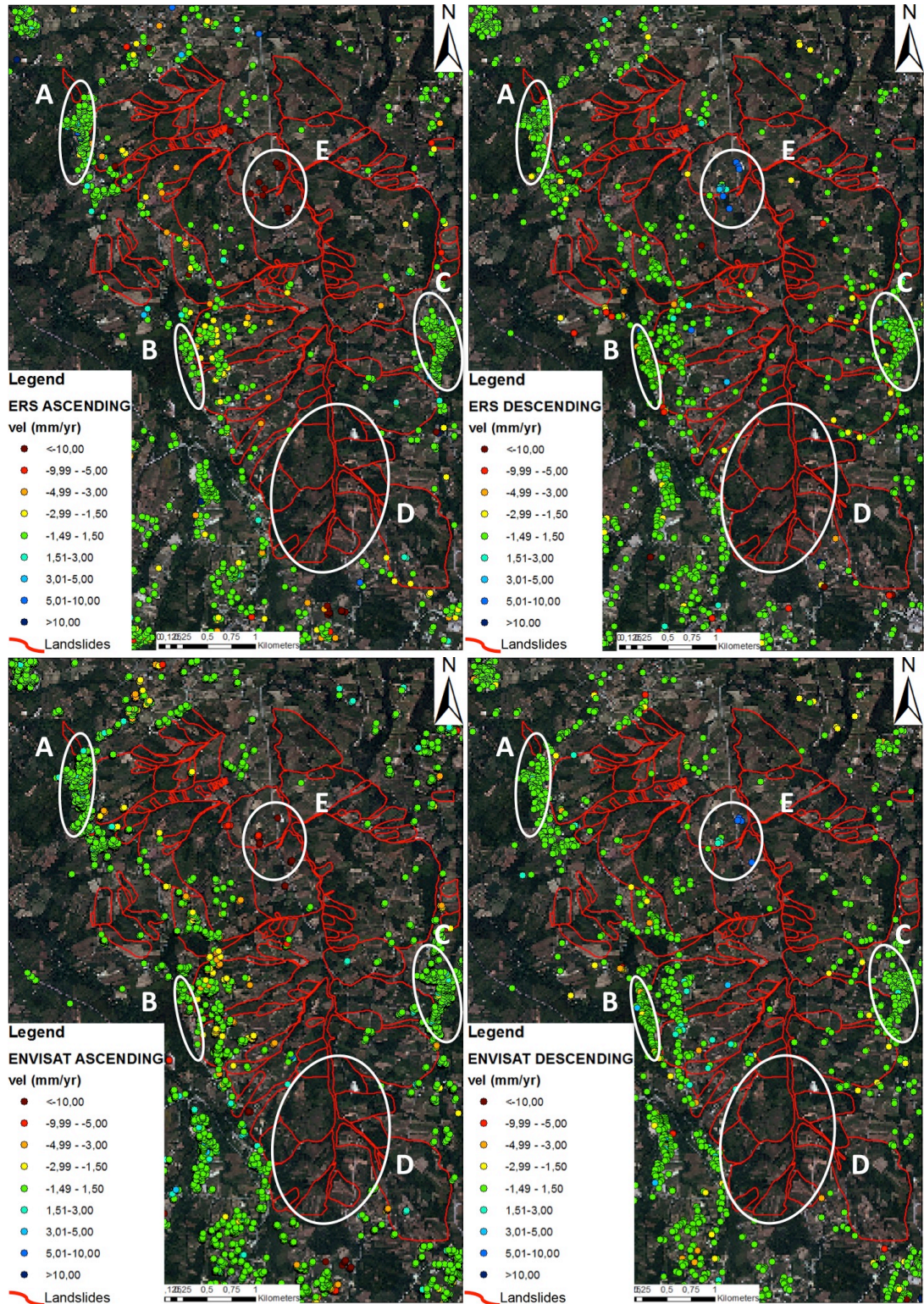


Figure 4.7 A-DInSAR results from the large scale analyses. PSs are presented as coloured dots. Colours from yellow to red state displacements away from the satellite, while dots from light blue to dark blue state displacements toward the satellite. Values are expressed in millimetre/year. Red polygons indicate landslide bodies mapped thanks to aerial photos interpretation and field surveys. A, B and C ellipses indicate urbanized areas. D ellipse indicates an area where no PSs have been detected because of absence of good scatterers. E area indicates the area affected by strong horizontal displacements discussed in par. 4.4.4.

Tab. 4.2 State of activity matrix based on combination of double orbital observation geometries (ascending and descending)

		Orbital geometry 2		
		Unstable PS	Stable PS	No enough PS
Orbital geometry 1	Unstable PS	Period of activity	Period of activity	Period of activity
	Stable PS	Period of activity	Period of inactivity	Undefined activity
	No enough PS	Period of activity	Undefined activity	Undefined activity

In this study, we propose an approach based on the observation of double orbital geometries to assess the period of activity for both the ERS (1992-2001) and Envisat (2003 – 2010) datasets. In Tab. 4.2, the basic operating principle of the proposed method is explained. A quite similar approach has been used by Cigna *et al.* (2012) to assess the reactivation and state of activity of landslides comparing different PSI datasets. The primary difference here is that the input data are not differentiated in time (e.g., ERS and Envisat), but they are contemporary (e.g., both ERS or Envisat) and belonging to different orbital acquisition geometries (i.e., ascending and descending).

Because landslides in the herein studied basin are located on both west and east facing slopes, even if PS data are available for both dataset results, displacements are sometimes visible in only one of them because of the direction of the LOS. Because of this, considering both geometries allows the detection of displacements that might go unseen with only one geometric condition. The state of activity matrix is quite preventive, and thus the detection of unstable PSs, even in only one geometry, is enough to assess the related landslide as “active” in that period. With the same logic, the detection of stable PSs in only one geometry is not sufficient to consider the landslide as “inactive” in the considered period. Moreover, the inactivity period is considered as such only when the presence of stable PSs is confirmed in both geometries. In Figure 4.8, the results from the activity matrix application are shown. For both the ERS and Envisat periods, green polygons define landslides characterised by the presence of stable PSs, whereas red polygons identify the presence of unstable PSs. Empty polygons identify landslides with missing or insufficient PSs.

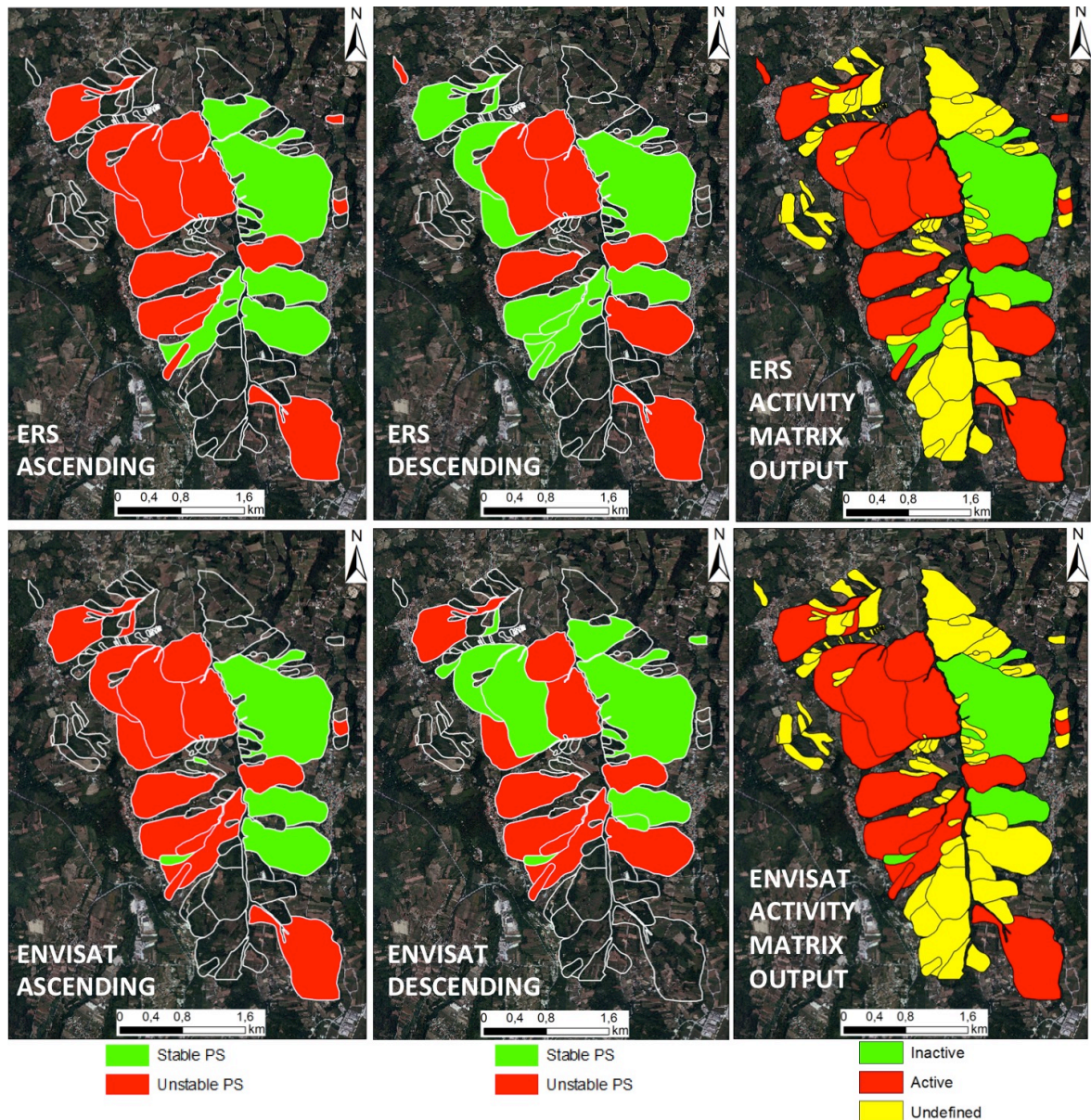


Figure 4.8 Results from the activity matrix applied to both ERS (1992-2001) (up) and Envisat data (2003-2010) (down). On the left PS results from ascending dataset, while in the centre PS results from descending dataset are shown. Green polygons identify presence of stable PSs within the mapped landslide; red polygons identify presence of unstable PSs; empty polygons show missing or insufficient PSs. On the right: state of activity derived from both orbital geometries combination as result of state of activity matrix. Colour codes are the same used for the state of activity matrix in Tab. 4.2.

Several deformation rate thresholds to define whether a landslide process is reactivated have been chosen by many authors (Cascini *et al.* 2010; Farina *et al.* 2006; Meisina *et al.* 2006; Cigna *et al.*, 2012). As a general rule for this case study, only PSs characterised by velocities greater than 2 mm/yr have been selected as active period markers, but case-by-case evaluations have been made based on geomorphological reasons and issues strictly related to local A-DInSAR results. Because deformation phenomena trends are extremely

slow or very slow (*sensu* Cruden & Varnes, 1996) also because the phenomena are primarily in the senile evolutionary stage, a state of activity definition based only on geomorphological features is often not easy. However, slow displacements typical of post-failure residual deformation are most likely best observed by A-DInSAR (Colesanti & Wasowski, 2006). The opportunity to observe and quantitatively measure past displacements using archived SAR data significantly altered the likelihood of defining the real temporal evolution of such phenomena.

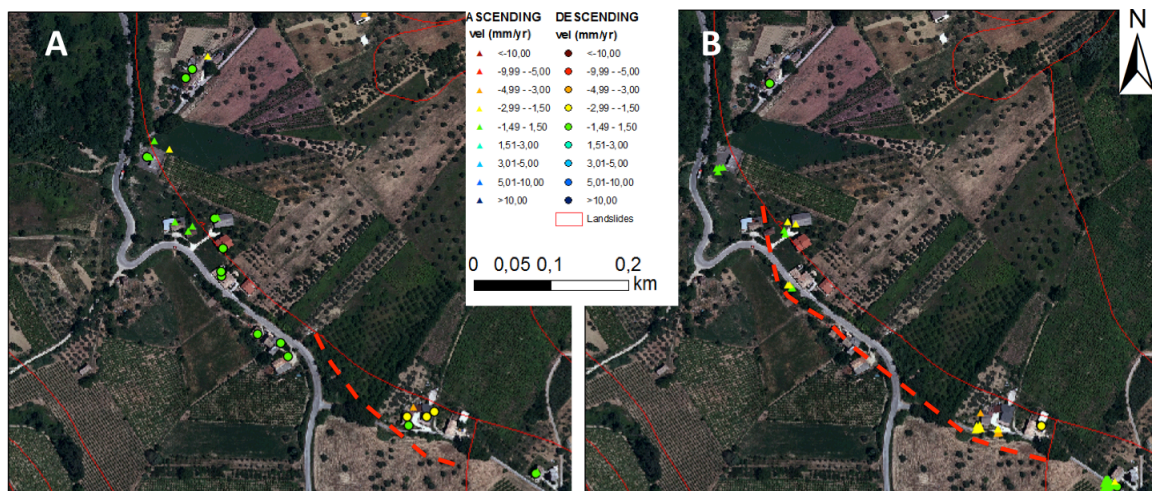


Figure 4.9 Example of crown retrogression for a large slide in the north-western part of the study area. In A: ERS (ascending and descending) results are shown (1992-2001); in B: Envisat (ascending and descending) results (2003-2010). The example shows progressive evolution of the phenomenon expansion over time. The dotted line shows hypothetical new bounds for the mapped landslide.

The A-DInSAR results were also useful in defining spatial changes over time. An example, representative of the interpretation that has been performed for several individual processes, is shown in Figure 4.9. A large slide, belonging to a more generalised slope deformation phenomenon comprising several coalescent bodies, experienced a gradual retrogression, detected by PSs affected by displacements from 1992 (the beginning of the period covered by the ERS data) to 2003 (the beginning of the Envisat observation period). This outcome (confirmed in the results of different datasets) is a confirmation of the role played by A-DInSAR in the slope dynamics investigation. The detection and quantitative measurement of past displacements allow for overcoming the limitations of the basic investigation methods, which usually are anchored on the need to detect not always easily observable geomorphological effects.

4.4.4. Characterisation of the landslide kinematics

In addition to increasing observable displacements over the whole area, the combination of both ascending and descending datasets has revealed other very useful things. In many cases, detection of deformation affecting the same area by both geometries was also useful to better define the real kinematics. For this purpose, it is interesting to note that some areas are characterised by the presence of PSs with different directions of displacement depending on the dataset orbital geometry. This is particularly evident in a small area very near to the Dendalo stream (ellipse E in Figure 4.7) where two groups of PSs show this behaviour. Especially for the northern group of PSs in the ellipse, the area appears more flat than it really is (also due to some anthropogenic elements which changed the local surface appearance); therefore, if only one acquisition geometry was used, a seriously wrong interpretation of the results would most likely have been attained. Using only the ascending dataset, the area appears affected by a subsidence-like process (movement away from the satellite), whereas the descending results show an uplift-like process (movement towards the satellite). Moreover, this behaviour is present in both the ERS and Envisat datasets.

The real reason for this behaviour is related to specific landslide kinematics, which are strictly affected by horizontal displacement. The area is on a very gentle slope (from 2 to 7 degrees) that marks the foot of a large landslide composed of several coalescent bodies. Vertical displacements are characterised by similar LOS deformation rates on both ascending and descending datasets, whereas strong differences between the results of the two datasets reveal the presence of horizontal components. The combination of the double-geometric datasets allowed the derivation of the vertical and horizontal (E-W) directions of movements (Figure 2.14) (Tofani *et al.*, 2013).

Considering the slope aspect, oriented nearly east, it was possible to use these results to interpret real local displacements along the entire slope in terms of orientation and magnitude (Figure 4.10). The results clearly highlight the overall slope deformation behaviour, primarily characterised by horizontal displacements, especially near the landslide foot, as is normal for this type of earth slide. This behaviour is confirmed in both the ERS and Envisat observation periods. Moreover, the portion of the landslide affected by a few highly vertical components is located very near to the crown of the lowest mapped landslide body, during both the ERS and Envisat periods. In addition, this effect is

congruent with the process kinematics affecting this landslide portion. The displacement rate is higher on this crown than on the crown of the upper landslide body, and the foot displacement rate, displays a similar pattern, both suggesting a more intense deformation affecting the lower part of the slope.

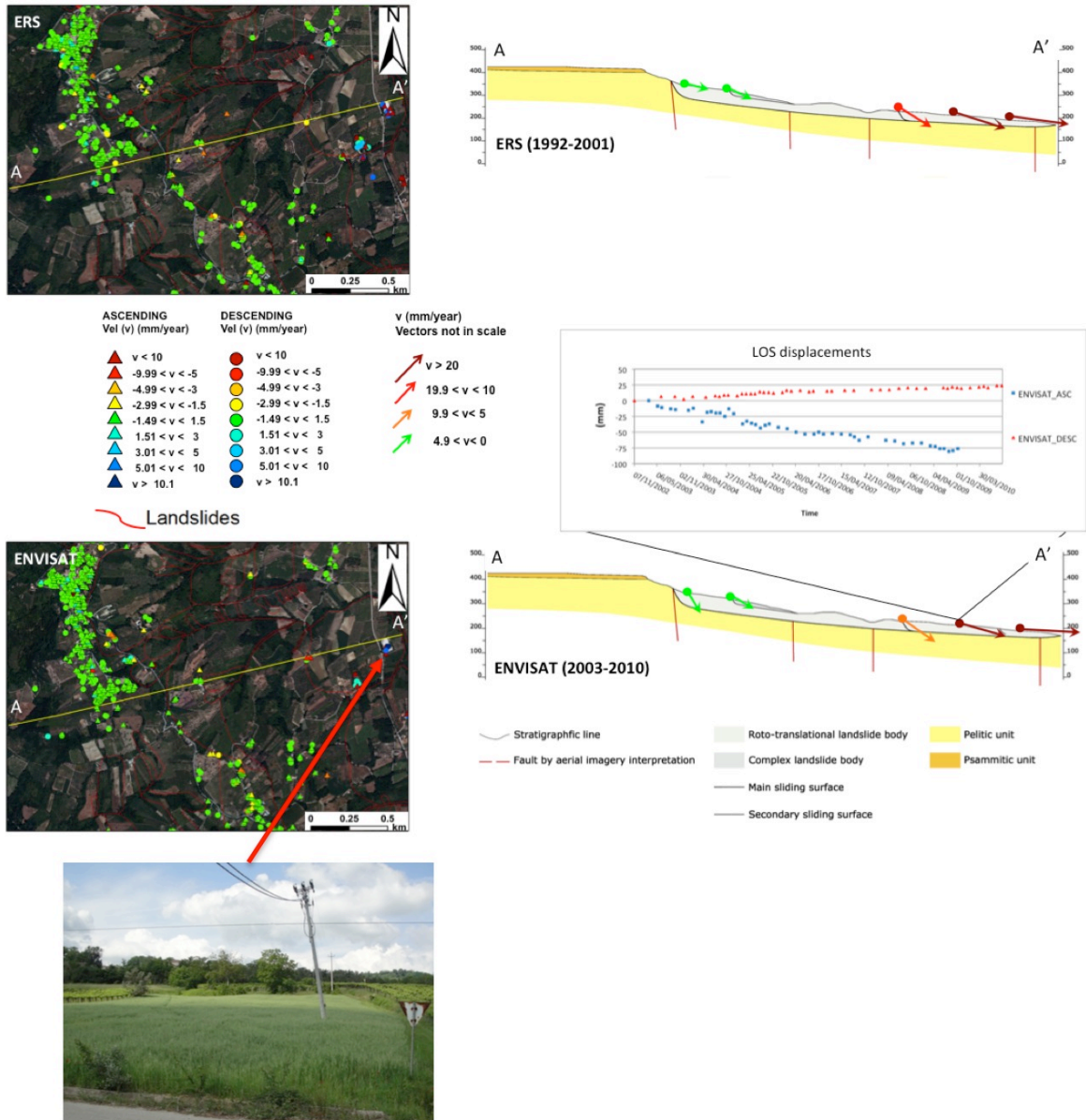


Figure 4.10 Section 1 - Section of an investigated landslide characterized by strong horizontal component. In A and B: ascending and descending PS results related to ERS and Envisat datasets respectively. The yellow line A-A' identifies the landslide section track drawn beside for ERS (up) and Envisat (down) periods. Coloured vectors represent displacements along the slope taking into account vertical and horizontal components derived by combining ascending and descending results. In the box, two time series of displacement related to ascending (blue) and descending (red) PSs used to derive the indicated displacement vector for the Envisat period. The picture shows a pylon affected by instability near the landslide foot.

Another similar example is shown in Figure 4.11 for a slide located in the centre of the basin. In this case, lower displacement rates have been found for both the ERS and Envisat periods.

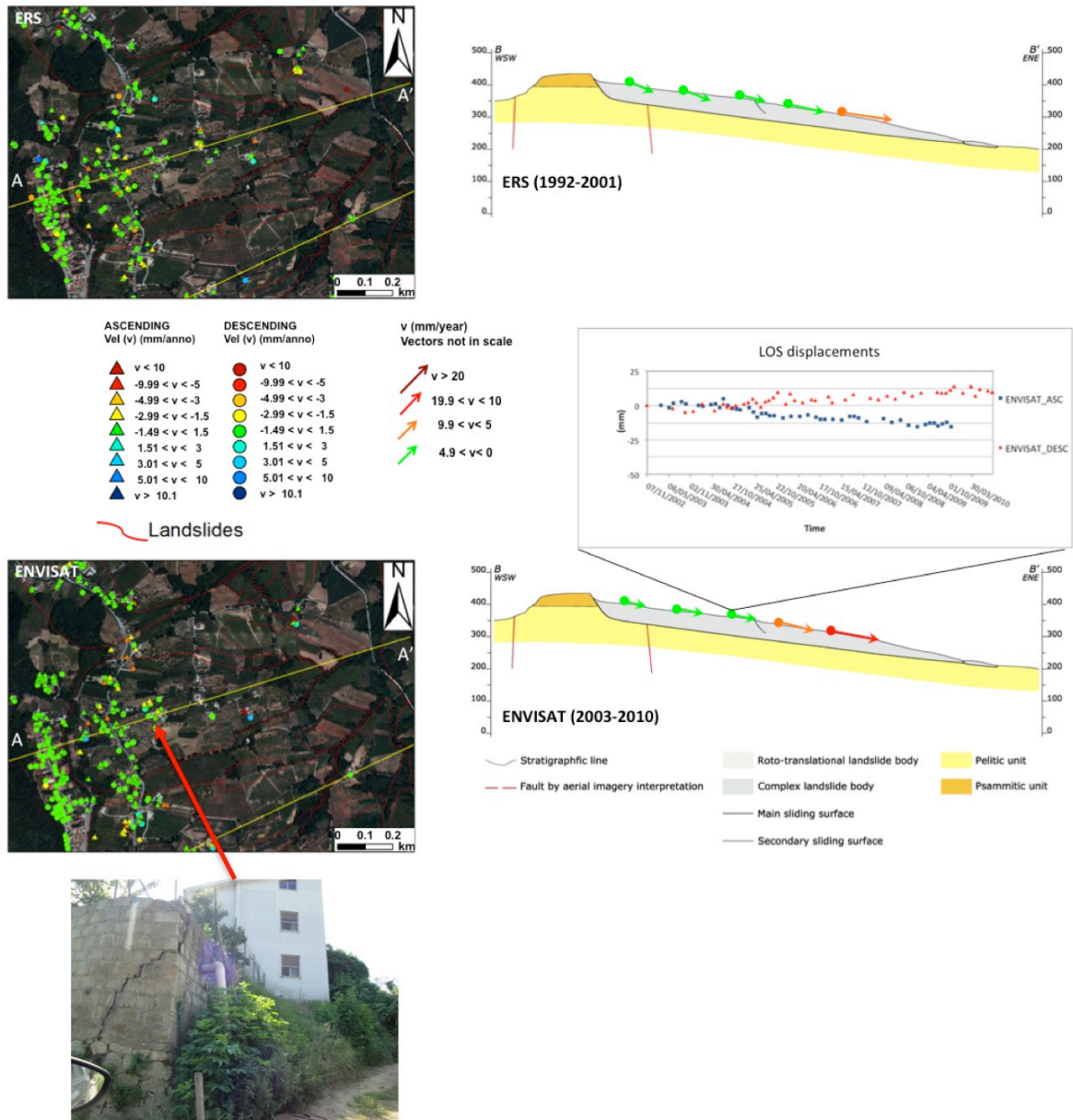


Figure 4.11 Section 2- Section of an investigated landslide characterized by strong horizontal component. In A and B: ascending and descending PS results related to ERS and Envisat datasets respectively. The yellow line A-A' identifies the landslide section track drawn beside for ERS (up) and Envisat (down) periods. Coloured vectors represent displacements along the slope taking into account vertical and horizontal components derived combining ascending and descending results. In the box, two time series of displacement related to ascending (blue) and descending (red) PSs used to derive the indicated displacement vector for the Envisat period. The picture shows a wall on the landslide area, affected by a fracture.

According to the aerial photo interpretation and field surveys, this process is caused by one single phenomenon, with no coalescent bodies or evidence of the presence of secondary failure surfaces. Indeed, the A-DInSAR results show more homogeneous deformation behaviour along the slope with a small vertical component near the crown area and with a main displacement direction sub-parallel to the maximum slope line.

The investigation of the dynamics of single processes has also taken advantage of the local-scale manual analysis. Figure 4.12 shows a displacement time series discovered using this approach. The displacement time series clearly shows an first active phase (February 2003 – December 2005), a stable phase (January 2006 – November 2007) and a reactivation phase (March 2008 – August 2010). Such a PS target could have been discarded by an automated analysis because the time series deviates from a linear model typically used in such analyses. However, the information conveyed by its behaviour is fundamental to better understand the landslide dynamics.

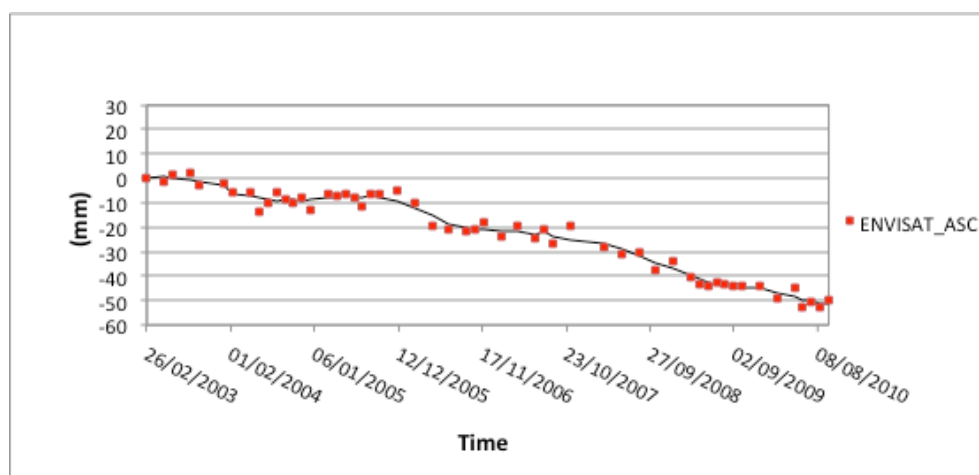


Figure 4.12 Time series of displacement achieved by using the new algorithm properly designed for non-linear deformation.

4.5. Discussion

As described above, A-DInSAR was revealed to be an excellent enhancement to the understanding of the processes under study. However, using these results, we can deduce some other general considerations less related to the present case study. A general look at the results of the entire study area (Figure 4.7) reveals more detailed A-DInSAR information attained for the east-facing slopes than for the opposite slopes. As stated by several authors (Colesanti & Wasowski, 2006; Colombo *et al.*, 2006; Notti *et al.*, 2010; Mazzanti *et al.*,

2011; Cigna *et al.*, 2012; Wasowski & Bovenga, 2014), several factors can affect the quality of A-DInSAR results for a given area. These factors are related to the SAR system features and the geomorphological local conditions (Mazzanti *et al.*, 2011). In the context of ground deformation phenomena, this point is crucial for landslides, where the investigated displacements are characterised by various directions of movement (vertical and horizontal) and also depend on slope orientation. Considering the study area and the presence of both west- and east-facing slopes, we partially controlled for this limitation by using double geometric investigation (ascending and descending orbits). The application of the state of activity matrix (Tab. 4.2) based on both ascending and descending contemporary datasets allowed for a better definition of the effective state of activity during the investigated periods (Figure 4.8). If compared with the results shown in Figure 4.5, the outcomes of the state of activity matrix provide more detailed information about the effective state of activity for the landslide processes mapped in the study area. A higher number of landslides were revealed as “active” in the investigated period (Figure 4.8) based on the information attained using geomorphological data (Figure 4.5). The state of activity derived using the interpretation of aerial photos and field surveys represents a sort of snapshot of a given condition at a well-defined moment. In this regard, the A-DInSAR investigation allows the observation of several processes in a wide area over a much longer time interval (even in the past). In this way, it is possible to assess a well-defined condition, related to the state of activity based not on observable effects on the ground, but starting from quantitative data related to the process itself (i.e., existing displacements), which are also less subjective. Moreover, it is well to remember that the activity matrix presented here is based on double and independent dataset results for each period (ascending and descending orbital geometries), thus allowing a more reliable outcome. Moreover, the topographical effects related to steepness and slope orientation (able to cause radar distortions on the images used) are not dramatic in the present case study. However, the results are insufficient for analysing all of the landslide processes. In the area investigated herein, the lack of PSs in some areas is primarily linked to the presence of only a few targets characterised by good radar scattering behaviour. Figure 4.13 shows that the distribution of buildings and artificial structures in the area fits well with the PS distributions in Figure 4.7. In a strongly vegetated area, such as this one, is evident as the presence of good scatters affects the A-DInSAR results more than any other radar or

geomorphological parameter. As stated by Hanssen (2005), A-DInSAR is an ‘opportunistic’ technique; thus, when such a methodology is used to study non-urban areas (which is a very common and likely scenario for areas affected by landslide processes), the role played by potential good scatterers is fundamental. Even if with low density, in fact, it is very important to have available some PSs in order to cover landslide bodies as more distributed as possible. An example of detection without PSs is visible in the D ellipse in Figure 4.7, where no PSs are detected because no good scatterers are present. Consequently, several landslides that were recognised as active by the interpretation of multi-temporal aerial photos and geomorphologic field surveys have unfortunately not had their past displacements investigated by A-DInSAR data.

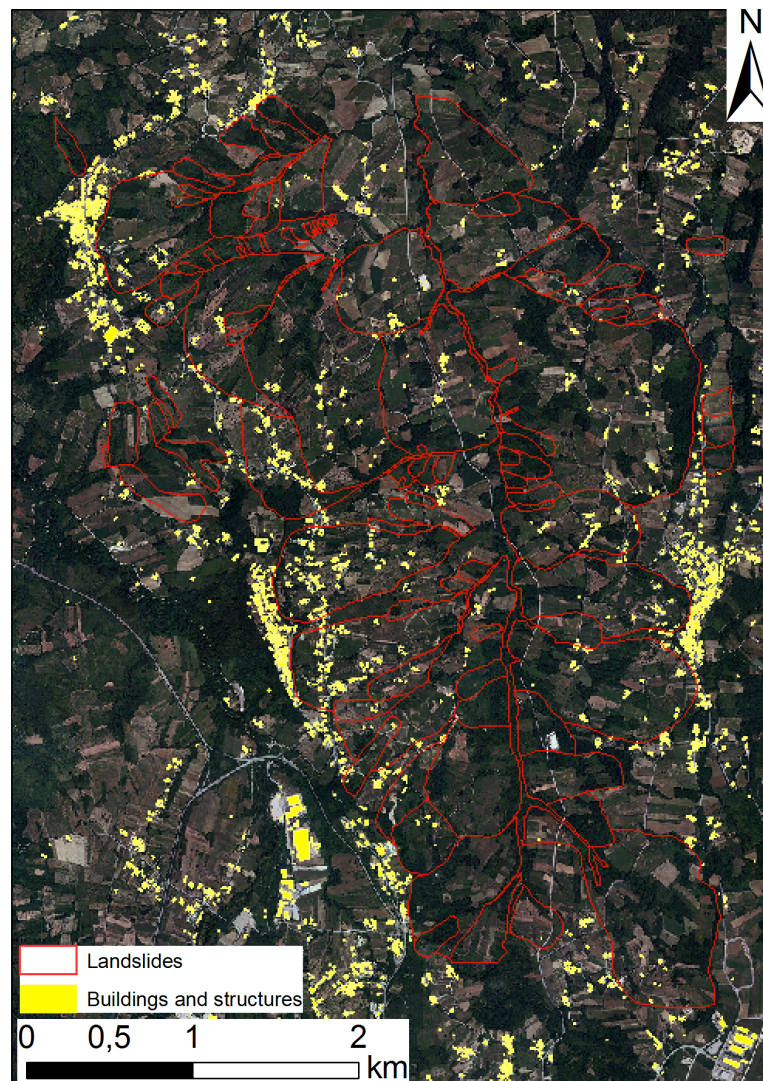


Figure 4.13 Map showing distribution of buildings and structures over the study area. Elements like these, represent potential good scatterers, hence PSs. It is worth to notice that west-facing landslides are interested by less potential scatterers if compared with those on the opposite side of basin portion.

4.6. Conclusions

In-depth remote sensing analyses, together with geomorphological field surveys, have been performed to extensively characterise landslide processes severely affecting a wide portion of the Dendalo stream basin. The interpretation of multi-temporal aerial photos allowed for the definition of the spatial and temporal evolution of the instability processes over the last 5 decades. Analyses of geomorphological features represented the initial step towards attaining a basic knowledge of the number, typology, extension and mapping of these phenomena.

Substantial improvement of knowledge has been attained using the A-DInSAR technique based on a mixed PSI/QPSI technique. The SAR data from the ESA archive have been analysed to extract information related to past displacements. We analysed almost 220 SAR images divided into 4 datasets covering approximately 18 years of deformational history of the investigated area. Every SAR dataset is subject to an independent A-DInSAR processing; therefore, the results attained represent a separate source of information. In this sense, the congruent redundant A-DInSAR results over same areas can be considered more robust and reliable.

Greater than 80% of the overall area affected by instability processes has been successfully investigated using A-DInSAR. Using both the ascending and descending datasets for both the ERS (1992-2001) and Envisat (2003-2010) periods enabled the observation of the deformational processes on both of the facing slopes, considering the satellite LOS and expected directions of movement of the slopes. The primary results have been attained on the western slopes, where more PSs were available. Taking advantage of these data, a landslide activity matrix has been adopted to assess past activity periods affecting the detected phenomena for an investigation that is complementary to the geomorphological-based techniques. Moreover, the double geometric combination also allowed the definition of the near-real landslide kinematics for those phenomena characterised by the presence of sufficient scatterers. Finally, the combination of different observation geometries avoided the misleading interpretation of some processes in ambiguous geomorphological conditions. We can state that the investigated portion of the basin is characterised by widespread slope deformation phenomena. The hilltops, where urban settlements are located, appear to be essentially stable over the analysed period.

Local scale analyses have been performed to improve the comprehension of the investigated processes. Compared with other ground deformation processes, landslides are characterised by strong spatial discontinuity. As a differential technique, A-DInSAR is based on the principle that essentially one point should be considered stable. From this perspective, local scale analyses performed with a manual approach represent an efficient methodology for InSAR investigations if sufficiently supported by detailed knowledge of the processes. Satisfying results have been attained in the detection of non-linear deformation processes. To conclude, we can say that differences in landslide characteristics (e.g., dimensions, types, presence of single or coalescent bodies, orientation, and typical velocity) also reflect slightly different deformation behaviours in terms of both kinematics and activity style.

Acknowledgments: The present work has been carried out thanks to the European Space Agency in the framework of the Cat-1 project “Landslides forecasting analysis by time series displacement derived from Satellite and Terrestrial InSAR data” (Id 9099). Grateful thanks also go to Geoservizi S.r.l. for providing information about basic geological data.

5. UNDERSTANDING THE SUBSIDENCE PROCESS OF A QUATERNARY PLAIN BY COMBINING GEOLOGICAL AND HYDROGEOLOGICAL MODELING WITH SATELLITE INSAR DATA: THE ACQUE ALBULE PLAIN CASE STUDY

5.1. Introduction

Ground subsidence is a common process occurring on the ground surface. Subsidence can be controlled by natural processes, such as volcanic activities (Lu *et al.*, 2002), but quite often it can be triggered or accelerated by human activities.

Underground excavations (e.g., mining and tunnelling) and new settlements on the ground surface are likely the most common anthropogenic factors causing local scale subsidence (Jung *et al.*, 2007; Guéguen *et al.* 2009; Samsonov *et al.*, 2013). However, fluid and gas exploitation are most commonly associated with regional scale subsidence involving square kilometre areas (Dixon *et al.*, 2006; Meckel *et al.*, 2006; Teatini *et al.*, 2011). Groundwater exploitation is likely the most challenging process as it generally affects large cities that require huge quantities of water for human activities. These processes have been extensively reported worldwide for several important cities, such México City (Cabral-Cano *et al.*, 2008; Osmanoglu *et al.* 2011; Chaussard *et al.*, 2014), Bangkok (Phien-Wej *et al.*, 2006), Shanghai, Tianjin, Beijing, China (Xue *et al.*, 2005), Lhokseumawe, Medan, Jakarta, Bandung, Blanakan, Pekalongan, Bungbulang, and Semarang, Indonesia (Chaussard *et al.*, 2013), Taipei, Taiwan (Hung *et al.*, 2011), Florence (Colombo *et al.*, 2003), Prato (Raucoules *et al.*, 2003), and Bologna (Modoni *et al.*, 2013).

In some cases, subsidence can be on the order of some meters with velocities of some decimetres per year, thus quite often causing damage to buildings and infrastructure. In other cases, more minor displacements can be revealed only by instrumental analyses. Among the ground displacement measurement techniques, satellite Differential InSAR (Gabriel *et al.*, 1989; Massonnet *et al.*, 1993; Bürgmann *et al.*, 2000; Ferretti *et al.*, 2000, 2001; Hooper *et al.*, 2004; Salvi *et al.*, 2004, Kampes, 2006) has provided over the last decade an incomparable stimulus to the study of such ground deformation processes. The opportunity to retrieve extensive displacement information over large areas with a spatial resolution of a few meters and a millimetre accuracy has allowed analyses at an

unprecedented level of precision (Amelung *et al.*, 1999; Fruneau & Sarti, 2000; Tesauro *et al.*, 2000; Hoffmann *et al.*, 2001; Burbey, 2002; Damoah-Afari *et al.*, 2008; Raucoules *et al.*, 2007, 2009; Heleno *et al.*, 2011; Osmanoglu *et al.*, 2011; Bock *et al.*, 2012). Furthermore, the availability of SAR data archives in some areas since 1992 represents a great opportunity to explore past processes and to analyse them, taking advantage of the most recent evidence and with the most advanced scientific knowledge of the subsidence process.

Obtaining information on ground or building displacement is a key feature for performing detailed and quantitative evaluations of the state of subsidence processes, but several additional studies are required to gain a comprehensive knowledge of the mechanism controlling such processes, especially for the purposes of prediction and assessment of future expected events. Recent studies have focused on the investigation of relationships between the subsidence process and geological, geotechnical and hydrogeological features of the area to shed light onto the expected future evolution of the instability process, thus supporting sustainable management (Tomás *et al.*, 2010; Budhu, & Adiyaman, 2010; Bru *et al.*, 2013; Raspini *et al.*, 2013).

This study follows the above-described approach, thus focusing also on the impact of human actions and groundwater exploitation on the subsidence process and its effects on buildings and infrastructure.

The study area is located between the municipalities of Tivoli and Guidonia in the Province of Rome (Lazio Region, Central Italy) where open pit travertine mines and hydrothermal waters represent the main economic activities (Figure 5.1).

This area, located in the hinterlands of Rome, has been affected by urban development during recent decades. After the recent edification of the area, structural damage to buildings has been recorded since the mid-1980s, with a strong intensification at the beginning of the 2000s, sometimes leading to the evacuation of houses and public buildings. The damages were primarily caused by a generalised subsidence process characterised by differential settlement that acted strongly on the buildings.

In this Chapter, to better understand the observed processes, we first describe a detailed geological model obtained by interpolating data from several available and purposely drilled boreholes and the 1954-2008 piezometric variations reconstructed through an inherited numerical model based on previous surveys. We then quantify the subsidence

process affecting the overall area from 1992 to 2010 using the Advanced DInSAR (A-DInSAR) methodology, combining the ERS-1/2 and Envisat interferograms from the ascending and descending tracks. Finally, we discuss the causes and time evolution of the observed subsidence, focusing on specific areas of the basin, where the availability and the detail of all of the above information have allowed us to better understand the observed phenomenon and its relationships with the considered environmental variables.

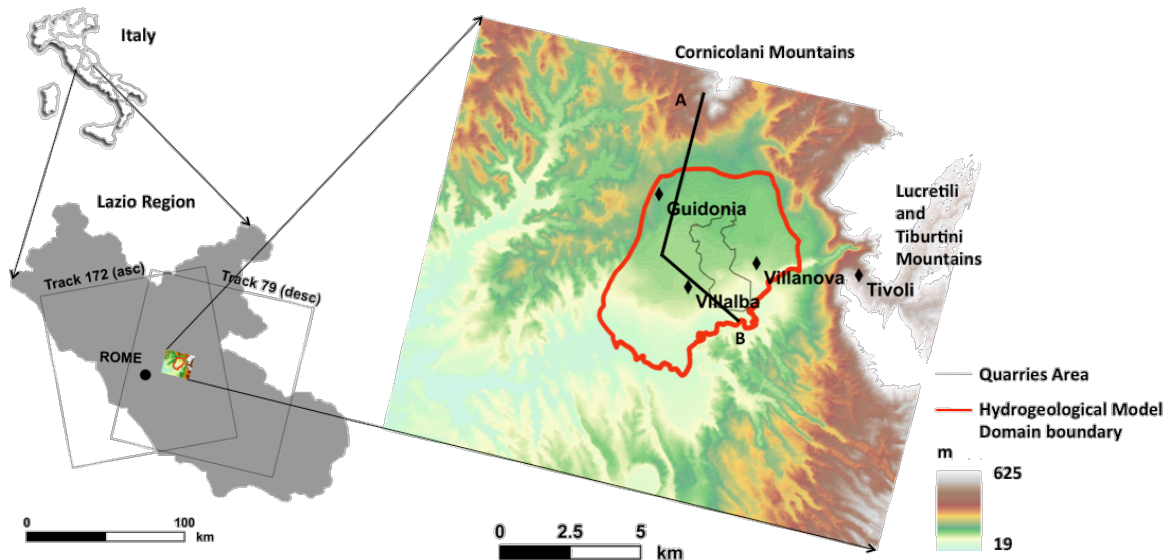


Figure 5.1 Location map of the Acque Albule Basin and model domain boundary within Italy and the Lazio Region. Ascending and descending ERS/ENVISAT frames are outlined in black. Region of interest is enlarged in the right figure. A-B cross-section is represented in the geological sketch of Figure 5.6.

5.2. Study site

The study area, known as Acque Albule Basin, is situated to the east of Rome, in central Italy. With a surface of approximately 30 km², it is mostly urbanised. The territory is quite flat, with elevations gently decreasing from approximately 80 m a.s.l. in the north to approximately 40 m a.s.l. in the south.

The primary industrial activity of this area is Travertine quarrying, performed since the ancient Roman age; after the second world war, this activity increased, thus involving a wide portion of the central part of the basin (Figure 5.2).

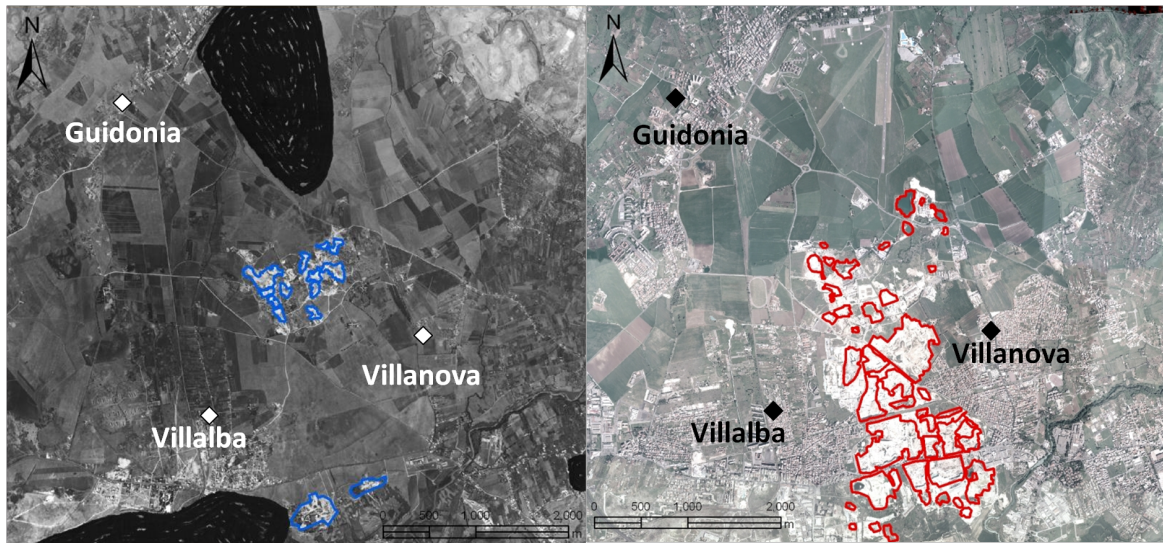


Figure 5.2 Evolution of the quarries activities in the plain. The left orthophoto represents the plain in 1954: the perimeter of each pit is shown in blue; some obscured areas are depicted such as the Guidonia airport to the north, as required by the military regulations at the time. The right orthophoto represent the plain in 2005: the perimeter of each pit is shown in red. It is clear the huge expansion of the quarries area (from Strappaveccia, 2007).

Strappaveccia (2007) analysed the evolution of human activities in the plain from 1954 to 2005 through a multi-temporal analysis of photographs and orthophotos of the area. The analysis showed that the quarry areas increased from 0.4 km² (1954) to 2.8 km² (2005) and also showed a progressive deepening of the quarry floors, from 14 m (1993) to 18 m (2005) below the original ground level. The estimated total volume of travertine quarried from 1954 to 2005 is approximately 50 Mm³.

Due to the local hydrogeological setting, the deepening of travertine extraction implies significant water pumping to keep the water table below the bottom of the quarries. Considering the activities of the quarries and the related dewatering, additional information was collected about the piezometric features and the water extraction in the area over recent years.

Piezometric levels under undisturbed conditions were derived from Lombardi (2005) using piezometric measurements taken in 1969 when quarrying activities were not particularly intense and no significant water pumping was necessary. The results showed that the piezometric levels were located in proximity to the topographic surface.

Piezometric measurements taken on the plain were collected for the years 1994, 1998, 2003, 2006, 2007 and 2008.

Furthermore, in 2006, the CERI (Research Centre on Prediction, Prevention and Mitigation of Geological Risks of the Sapienza University of Rome) installed four multi-level electrical piezometers in two boreholes (S16 and S17) (Figure 5.3) located close to the open pit area. The piezometric heads show a downward trend during the time interval 2006-2008, attributed to the increased pumping of water from the nearby quarries. In March 2007, the CERI research group, in coordination with the regional authorities, measured the perimeter of each pit, its piezometric level, the quarry floor elevation and the location and characteristics of the active pumps. Among the 19 active and inactive quarries examined, eight quarries that apply dewatering programs were identified (Figure 5.3).

Regarding the volumes of water extracted to allow travertine mining, the data show a progressive increase in pumping over time. Lombardi (2005) estimated a flow rate of 1 m³/s in the 1970s.

Flow measurements in the channels (Figure 5.3) built to transport the water drained from the quarries to the Aniene River are available only since 1998. Tab. 5.1 summarises the flow data derived from unpublished technical reports and bachelor and PhD theses listed in the table.

Tab. 5.1 Total Volume of water drained from the quarries to the two canals

	Pastini channel m³/s	Longarina channel m³/s	Total m³/s
1998 (Brunetti, 2010; Carucci, 2010)	0.64	1.520	2.150
2006 (Capelli & Mazza, 2006)	0.797	1.634	2.431
Jan 2008 (Sbarbati, 2008)	1.574	1.634	3.208
Feb-Mar 2008 (La Vigna, 2012)	1.752	2.546	4.298

The continuous pumping from the quarries has resulted in the progressive reduction of the flow from two springs, Regina Lake and Colonnelle Lake (well known as Acque Albule springs), whose thermal waters are used by several spas, which are the second source of income for this area. Since July 2007, an artificial recharge of 0.5 m³/s was activated by the Regional Civil Protection Department with the purpose of raising the water level of Regina Lake. The plan consists of two wells, located 1.4 km north of the lake, which extract a flow of 0.25 m³/s each. This water is fed into Regina Lake through an underground pipeline (Prestininzi, 2008).

A careful examination of the available data shows that a generalised lowering of the water table affects a wide portion of the Acque Albule Basin, whereas a more significant dewatering (and related piezometric level lowering) involves the areas surrounding the travertine quarries. The piezometric map of Bono (2005) shows a decrease in groundwater level of between 5 to 10 m in the Villalba area in 2005, where major damages to structures occurred, whereas in the areas of the quarries, that decrease is up to 30 m (Figure 5.4).

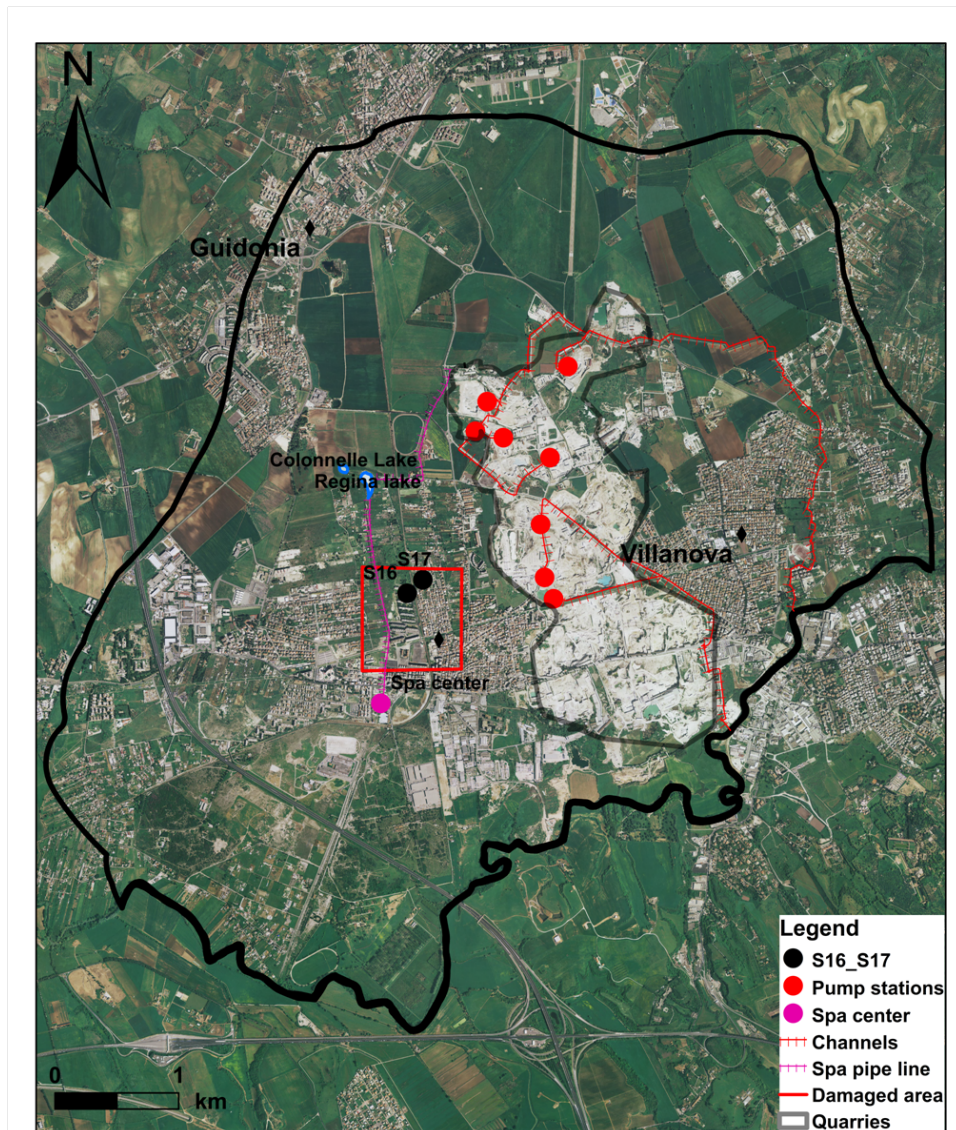


Figure 5.3 Location of the main features in the area of interest.

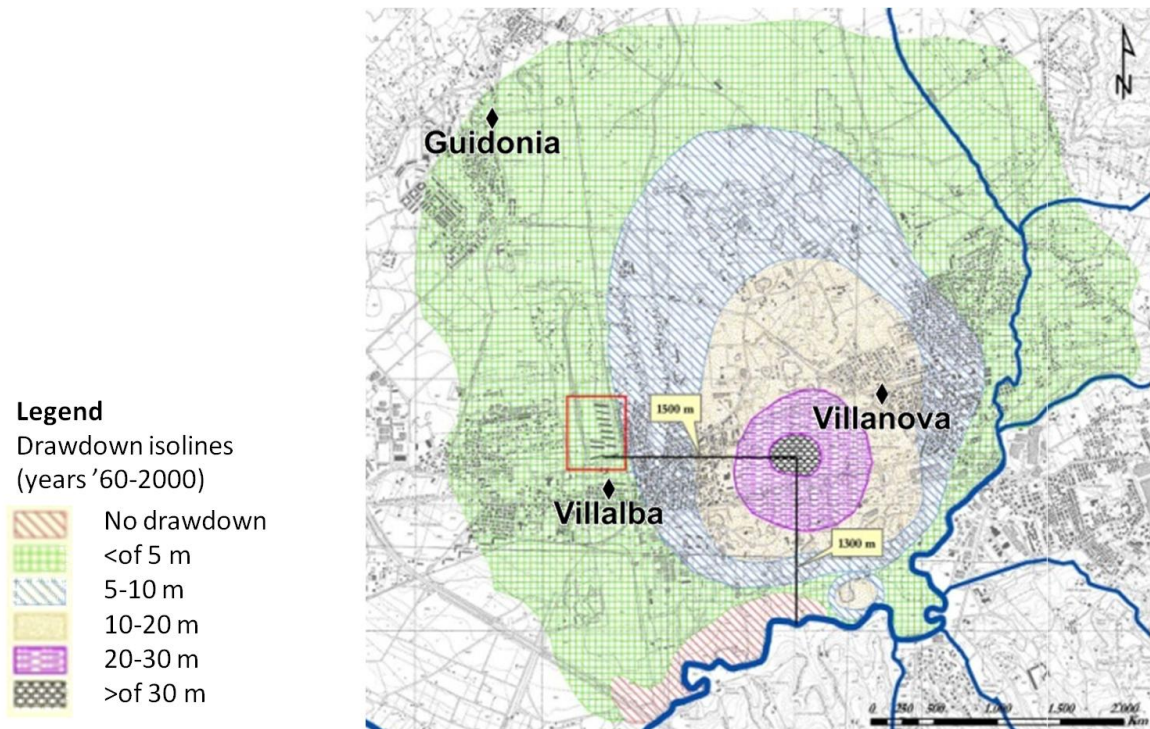


Figure 5.4 Groundwater level fluctuation between 1960s – 2000 according to Bono (2005). The red box indicates the most damaged area.

5.2.1. Geological setting

The Acque Albule Basin is a morphotectonic depression, whose formation and development is related to the Plio-Quaternary activity of strike-slip tectonic elements (Figure 5.5). The basin is bounded to the north and east by calcareous ridges (Cornicolani, Lucretili and Tiburtini Mountains) and to the west and south by the distal slopes of the Colli Albani volcanic edifice and the hilly roman area, both composed of pyroclastic deposits. The Aniene River, the left tributary of the Tiber River, flows from NE to SW and marks the southern margin of the basin.

The morphotectonic depression, whose bedrock features Meso-Cenozoic limestone, hosted the deposition of Plio-Pleistocene alluvial, lacustrine and volcanic deposits. These deposits are in turn covered by a thick (up to 80 m) travertine cover, well known since the Ancient Roman age by the name of *Lapis Tiburtinus*. This cover, whose precipitation and growth occurred in several phases between 115-130 thousand years ago (Faccenna *et al.*, 1994; Billi *et al.*, 2007; Faccenna *et al.*, 2008), connected with water table oscillations in the basin, is strictly connected with a deep hydrothermal circulation into the Meso-Cenozoic limestone. The travertine is primarily composed of thick, cemented banks with variable

degrees of porosity and fracturing. Palaeosol levels, clayey layers and karstic cavities and conduits locally interrupt the continuity of the travertine plateau.

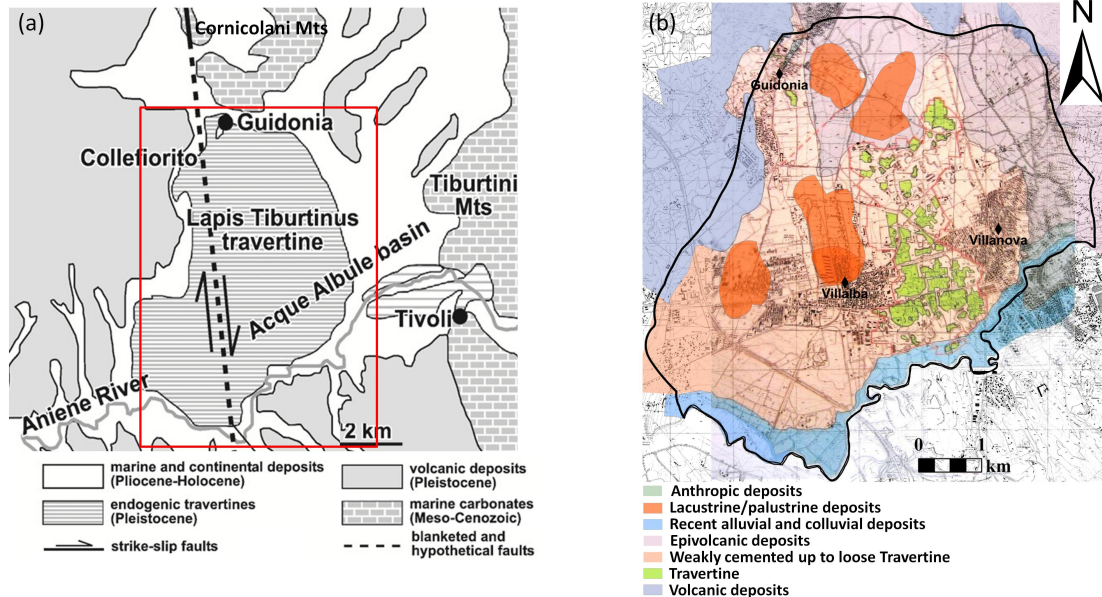


Figure 5.5 In (a) we show the geological map of the study area including the Acque Albule basin (from Faccenna *et al.*, 2008). The red box in (a) represents the area in (b) where the geological map of the Acque Albule Basin is shown (Funciello *et al.*, 2005, modified). Geology is overlaid on a topographic map (1:10.000 scale).

A discontinuous cover of a weakly cemented up to loose travertine, composed of clasts interspersed in a sandy-silty matrix, marks the last phase of travertine deposition.

Finally, the karst collapses in the uppermost part of the travertine sequence caused the formation of morphological depressions, which hosted a lacustrine-palustrine environment with the deposition of sandy silts, clay-loam (with high percentage of organic matter) and peats immediately below the present ground level.

The above geological schematic reconstruction suggests complex vertical and lateral relationships among markedly different lithologies (i.e., cemented travertine, loose travertine and lacustrine/palustrine deposits) in the first 10-20 m below the ground level. The lithostratigraphic setting of the first meters of the subsoil is then characterised by significant variations both vertically and horizontally. The roof of the travertine is strongly articulated by erosion and karst dissolution, such that it is possible to shift from situations in which the travertine reaches the ground surface to areas in which the most recent lacustrine-palustrine deposits fill previous sinkholes with thicknesses up to approximately

20 meters. To define a reliable geological model up to this depth, 97 borehole stratigraphic logs were collected in a georeferenced database, which allowed us to attain fairly detailed information on the spatial distribution of the different deposits in the study area at different resolutions. A low-resolution geological model (average information density of approximately 3 logs per square kilometre) was constructed at the basin scale, and a high-resolution model (average information density of nearly 1 log per ha) was produced for the most damaged area.

With reference to the geotechnical properties, an initial, preliminary model can be based on the results of site and laboratory investigations, both original and derived from the work by Prestininzi (2008). This model features five litho-technical units: 1) anthropic land cover; 2) sandy silts, clay-loam (with high organic content) and peats; 3) weakly cemented up to loose travertine (silts, sandy silts and gravels in a silty matrix); 4) intensively fractured travertine; and 5) travertine banks.

Tab. 5.2 Geotechnical parameters: Saturated unit weight and dry unit weight (γ_{sat} , γ_d), Relative Density (Dr%), Effective stress friction angle (ϕ') Blow count (N_{SPT}), Cone resistance (q_c) Undrained cohesion (C_u); Drained deformation modulus (E') (from Prestininzi, 2008).

Geotechnical Unit	DR %	γ_d (kN/m ³)	γ_{sat} (kN/m ³)	ϕ'	N_{SPT}	q_c (MPa)	c_u (kPa)	E' (MPa)
I Anthropic covers	30	14.5	18.8	26	9	-	-	13
II Sandy silts, clay-loam (with high organic content) and peats.	-	13.3	18.1	-	2	-	12.7	1.5
III weakly cemented up to loose travertine, composed by clasts interspersed in a sandy-silty matrix.	20	14.7	18.8	23	5	-	20.0	1.75
IV Fractured travertine	-	23.9	-	29	-	54	-	6200 **
V Travertine	-	23.9	-	30.5*	-	110	-	9300 **

* Strength detected by UCS tests and assumed equal to 1/3 of q_c ; **Parameter derived by applying of Hoek and Brown criterion

To characterise the geotechnical properties of the different deposits, CPTU tests and heavy penetration tests (DPSH) were performed; furthermore, oedometric tests were performed on high quality samples from the clay and peat levels. Based on the geotechnical features, five different geological-technical units were identified; their main geotechnical parameters are summarised in Tab. 5.2

Unit 1 is very variable in thickness (0 to 3 meters) and composition; its technical parameters are thus difficult to summarise.

Units 2 and 3 are characterised by poor mechanical parameters, especially in terms of strength and deformability, as they are loose/unconsolidated and often highly compressible. Moreover, these units are very heterogeneous from both a stratigraphic and geotechnical perspective.

Units 4 and 5 are characterised by high values of unconfined compressive strength (approximately 100 MPa for the rock matrix and 50 MPa for the rock mass) as well as by high values of deformation modulus (derived by applying the Hoek and Brown criterion).

The low values of relative density ($D_r\%$), blow count (N_{SPT}) and cone resistance (q_c) distinguished the second and third geotechnical units (namely, organic clay-loam and peat and loose travertine sandy silts) as “compressible”.

Starting from the detailed geological model attained by interpolating the available stratigraphic logs, a simplified map of thicknesses of compressible levels has been derived, showing a high variability of thickness, ranging from tens of centimetres where travertine is outcropping up to more than 20 meters in the central part of the basin. However, some positive anomalies (i.e., high thickness) are recorded at some points in the western and northern areas (Figure 5.12c).

The spatial distribution of the thickness of these deposits is in accordance with the description of Maxia (1950); in the areas of greater thickness of the “compressible” deposits, he reported the presence of small lakes and wetlands, currently masked by the intense urbanisation of the area.

5.2.1. Hydrogeological setting

The complex geological setting described above determines the complex multi-level groundwater circulation in the region (Figure 5.6). Specifically, the Meso-Cenozoic limestone hosts a deep aquifer fed laterally by the deepest part of the surrounding

carbonate ridges, outcropping east and north-east of the basin (Figure 5.5). The groundwater at these levels is thermalised due to the rise of deep fluids from the supply system of the Colli Albani volcanic complex, which outcrops southward. The aquifer is confined at the top by clayey-sandy Pliocene and Pleistocene deposits acting as an aquitard/aquiclude and therefore providing a piezometric level that is at times higher than the ground level.

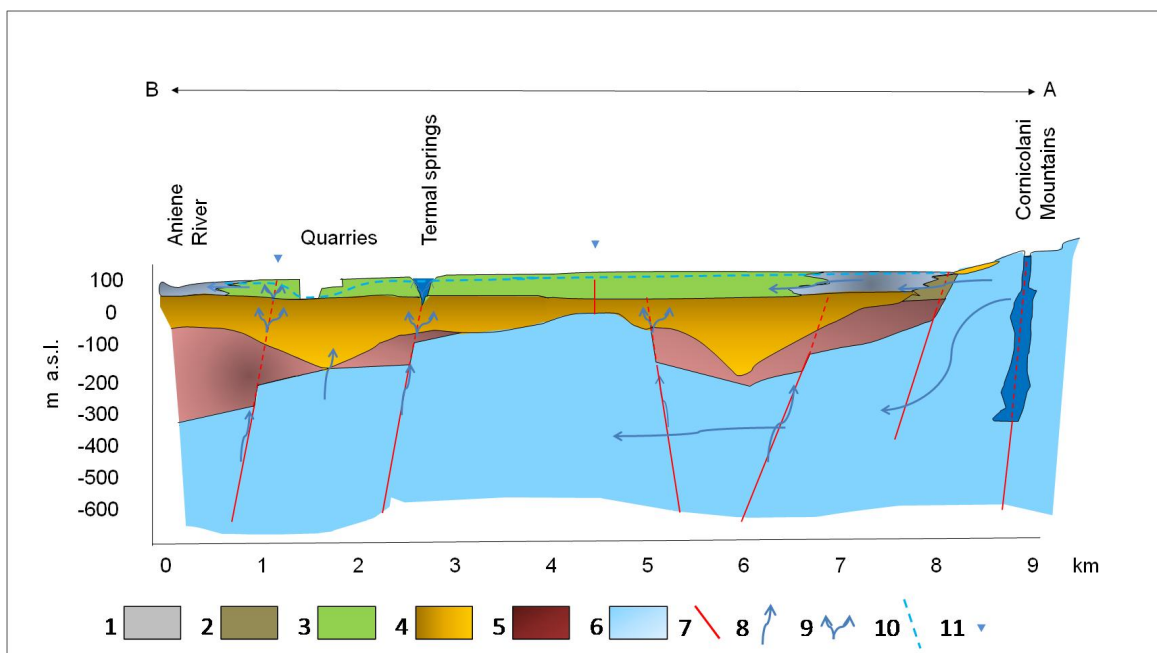


Figure 5.6 Cross sections A–B is located on Figure 5.1. 2D view of the geological and hydrogeological conceptual model for the Acque Albule Basin. Key to legend: 1) recent alluvial and colluvial deposits; 2) Debris; 3) Travertine and lacustrine/palustrine deposits; 4) Pleistocene alluvial, lacustrine, and epivolcanic deposits; 5) Pliocene marine deposits; 6) Carbonatic bedrock; 7) Fault; 8) Flow direction; 9) Groundwater overspill; 10) Water table level; 11) Confined water table level. Modified after Capelli *et al.*, (2005b).

The aquitard separates the deep aquifer from the most superficial one hosted in the travertine plateau, which is directly fed by rainfall (characterised by an effective infiltration of 275 mm/y) and laterally fed by the above mentioned surrounding carbonate ridges (with an estimated flow of 4 m³/s). Furthermore, this superficial aquifer is partially fed by the upwelling of thermalised waters (and gas) coming from the deep aquifer and passing through the tectonic discontinuities that drove the formation of the basin itself (Faccenna *et al.*, 2008; Boni *et al.*, 1986; Capelli *et al.*, 1987; Faccenna, 1994; Capelli *et al.*, 2005a) (Figure 5.5). Several springs with significant discharge, such as Acque Albule, Bretella and Barco springs, demonstrate the huge potential of this aquifer, whose water

originates from the ascent of hydrothermal fluid from the deeper aquifer. Therefore, with the travertine aquifer, the Aniene forms a "global system" in which the two hydraulic units are characterised by continuity and reciprocal exchanges (Boni *et al.* 1986; Bono, 2005; Carucci, 2010).

The hydrodynamic parameters of the superficial travertine aquifer were estimated by pumping tests and recovery tests. The estimated conductivity is $5.3 \cdot 10^{-3}$ m/s with a specific yield of 0.01, and the estimated transmissivity is $2.7 \cdot 10^{-2}$ m²/s (Rosella, 2007; Petitta *et al.* 2011; Brunetti 2010; Brunetti *et al.* 2013; Carucci *et al.* 2012).

5.2.1.1. Groundwater numerical modelling

In the framework of the PRIN project 2009 (“*Analysis, monitoring and control of geological instability interacting with human activities*”), Franchi (2012) investigated the evolution of the underground water circulation using a 3D groundwater flow model, which was developed using Visual MODFLOW 4.2 (Waterloo Hydrogeologic Inc., 2006) as the pre- and post-processor of the finite-difference code MODFLOW2005 (Harbaugh, 2005) to reconstruct the “time history” of the dewatering process over time and space. In this section some details about the hydrogeological model used to infer the subsidence process are presented.

The Acque Albule model was calibrated and validated with respect to the hydraulic conductivity field following a two-step procedure: i) as a steady state model representing quasi-natural conditions, reproducing the average natural heads prior to well exploitation; and ii) as a transient model, reproducing the extraction-influenced flow system conditions, from 1954 to 2008, which were substantially determined by pumping and thermal activities. The models were calibrated with a trial-and-error procedure.

The domain of the model covers 32.5 km² and circumscribes the travertine aquifer system, including the extraction area of the quarries, the area affected by subsidence and the urban settlements of Villanova, Villalba and Guidonia.

The average size of the cells is 50x50 m, with a grid refinement of up to 10x10 m in the areas of the quarries, Regina Lake and Barco and Bretella springs, to better represent the features of the groundwater flow in the areas of interest. The final grid therefore comprises 309 rows and 262 columns.

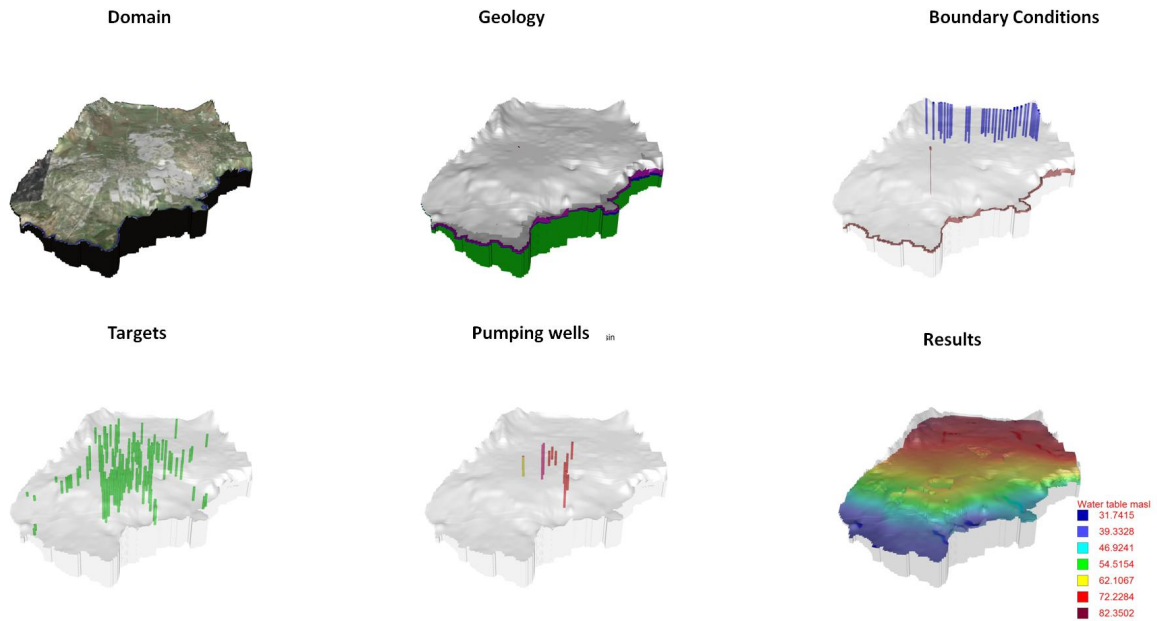


Figure 5.7 Processing chain for obtaining the 3D hydrogeological finite-difference model. The model domain has been defined and 3D geology has been derived from 97 boreholes. Once boundary condition has been defined, the model has been calibrated on the basis of available data (targets). Finally, the “time history” of the water levels has been derived (redrafted after Franchi, 2012).

Following Brunetti *et al.* (2013), the model considers three hydrostratigraphic units (i.e., three layers). The first layer was the sum of the first and second units of the geotechnical model described previously, the second layer corresponds to the third unit, and the third layer groups the fourth and fifth geotechnical units of that model. The geometry was obtained by the interpolation of the stratigraphic data, using the Inverse Distance Weighted method (IDW). The elevation of the bottom of the travertine (third layer) was derived from Brunetti (2010). The topography was derived from the digital elevation model of the Lazio Region with a spatial resolution of 20 m.

The main groundwater inflow to the travertine aquifer along the northern margin was simulated by a constant flow boundary condition using the MODFLOW Well Package applied in the form of wells injecting water at rates equal to the lateral recharge from the Cornicolani and Lucretili mountains ($4 \text{ m}^3/\text{s}$. Boni *et al.* 1986; Capelli *et al.* 1987; Carucci *et al.* 2012; Brunetti *et al.* 2013).

A constant head boundary condition equal to the hydrometric heights was assigned to the cells, corresponding with the main thermal discharge zone of Regina Lake and the Barco and Bretella springs. Hydrothermal water entering the system from the deep carbonate aquifer beneath Regina Lake was represented via a constant head boundary condition

assigned to the second and third layers. A constant head boundary condition representing groundwater discharge was assigned to the top layer of the model, coinciding with the location of the Aniene River along its southern flanks (Figure 5.7). No-flow boundaries were assigned along the eastern and western sides of the domain.

Effective infiltration was considered uniform over the whole domain. In the steady state, undisturbed conditions, the effective infiltration was assigned to the uppermost active cells as a constant flux of 274 mm/y (Brunetti *et al.*, 2013). In transient conditions, the effective infiltration recharge was assigned only for six months of the year, from November to April, and it was considered to be negligible for the remaining months based on the rainfall pattern of central Italy outlined by Dragoni (1998).

Tab. 5.3 Calculated hydraulic conductivity

Zone	k_x (m/s)	k_y (m/s)	k_z (m/s)
First and second Geo-technical unit	$1.5 \cdot 10^{-7}$	$1.5 \cdot 10^{-7}$	$1.5 \cdot 10^{-7}$
Third Geo-technical unit	$3 \cdot 10^{-4}$	$3 \cdot 10^{-4}$	$3 \cdot 10^{-4}$
Fourth Geo-technical unit	$4 \cdot 10^{-2}$	$4 \cdot 10^{-2}$	$4 \cdot 10^{-2}$
Fifth Geo-technical unit	$5 \cdot 10^{-4}$	$5 \cdot 10^{-4}$	$5 \cdot 10^{-4}$
Aniene River bed	$2 \cdot 10^{-4}$	$2 \cdot 10^{-4}$	$2 \cdot 10^{-4}$
Height conductivity conduit	1	1	1
Aniene deposits	$1.21 \cdot 10^{-5}$	$1.21 \cdot 10^{-5}$	$1.21 \cdot 10^{-5}$

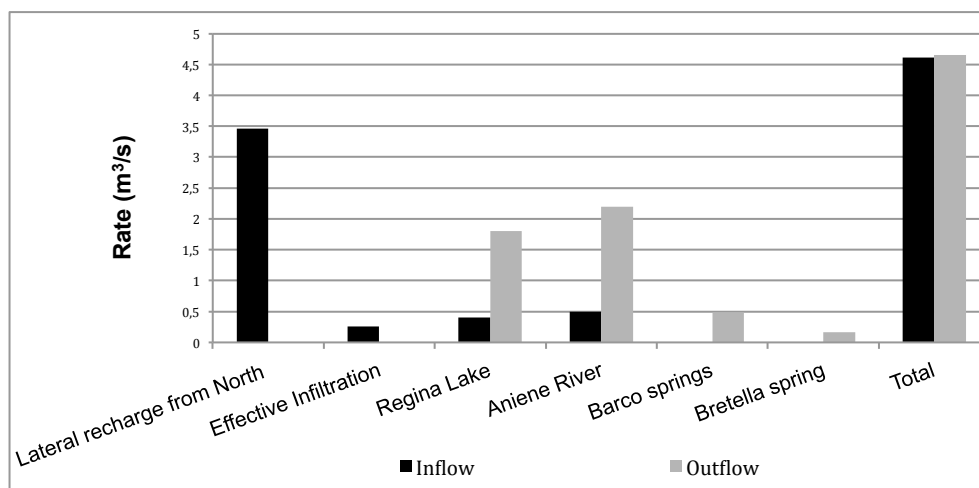


Figure 5.8 Inflow and outflow rates in steady state condition.

The goal of the steady model was to simulate the undisturbed flow conditions represented by the piezometric field in 1954, when the mining activities were concentrated in a very limited area (Strappaveccia, 2007). The targets, i.e., the observed values, used for calibration were taken from Maxia (1950). The calibration process was performed, primarily focusing on the hydraulic conductivity of the travertine, by using horizontal hydraulic conductivity (k) and transmissivity (T) derived from the pumping test described above. Specifically, five different classes of permeability have been defined with varying values, from a minimum of 10^{-7} m/s to a maximum of 10^{-3} m/s. Following Brunetti (2010), a higher conductivity value, $7 \cdot 10^{-2}$ m/s, was then assigned to specific areas: i) the northern and north-eastern boundaries where the travertine aquifer is fed by the inflow from the Cornicolani and Lucretili carbonate aquifer; ii) along the north-south fault passing through Regina Lake; iii) in the quarries area, with a general trend reflecting the jointing of travertine, as explicated by Capelli *et al.* (2005b). Moreover, a high conductivity value ($k = 1$ m/s) was also assigned to a conduit that preferentially drives hydrothermal fluids from a deep aquifer, directly feeding Regina Lake.

The performed calibration led to the values of hydraulic conductivity summarised in Tab. 5.3 and the resulting mass balance shown in Figure 5.8.

The agreement between the model and the observation (MAE = 0.753; RMSE = 1.06 m) has been considered satisfactory for the purpose of the present study.

The validation step was performed in transient conditions. Both the initial conditions of the piezometric heads and the conductivity values assigned to the model were derived from the previous calibration step. All piezometric data available and described in Section 5.2 were used as the targets for the calibration. The elevation of the pit floors for the years 1954, 1985, 1993, and 2001 derived from Strappaveccia (2007) and those obtained from Rosella for 2007 were considered indicative of the piezometric heads necessary to allow the mining activity.

We considered eight pumping wells corresponding to the main pumping stations that were individuated during the quarry monitoring survey performed in March 2007 (Rosella, 2007; Brunetti, 2010). The quantity of water pumped by each quarry was assumed to be proportional to the number of active pumps. The uncertainty of the extractions from the quarries is primarily due to the uncertainty of the evolution of this budget term during the period between two successive measurements (see Tab. 5.1 and Section 5.2). The

dewatering rates for the single wells were assigned and adjusted using a trial-and-error procedure.

The pumping station installed at Regina Lake to supply the water demand from thermal activity was simulated through a well that removed water from the domain at a rate of $0.700 \text{ m}^3/\text{s}$. Two wells extracting water at a rate of 250 l/s each were used to simulate the Civil Defence well field. The water extracted through these wells flows into Regina Lake. This feature was embedded into the model via an injection well of 500 l/s .

As an example, Figure 5.9A and B show the time series calculated for the piezometers at S16A compared with the observed values (Figure 5.3).

The trend calculated for the period 2006-2008 correctly reproduces the observed decreasing trend.

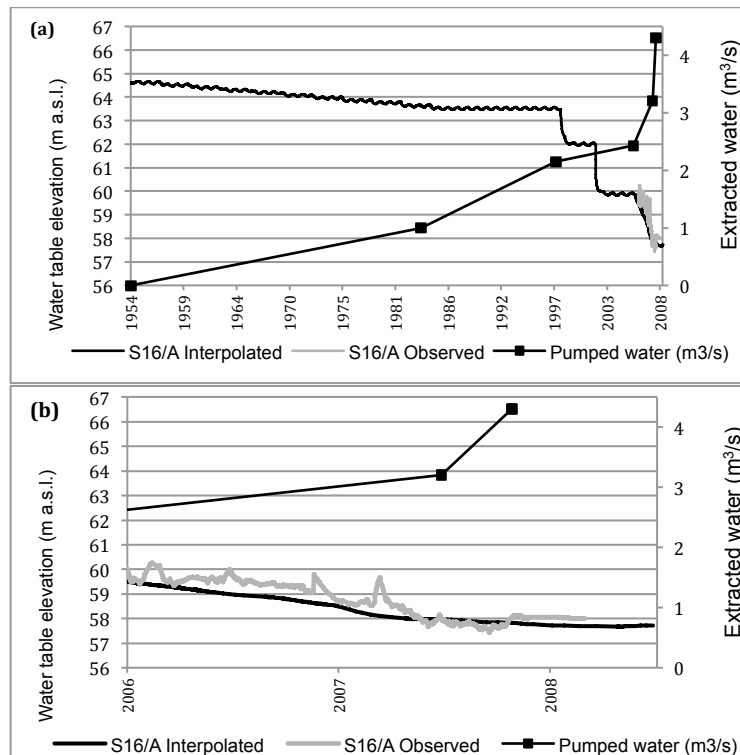


Figure 5.9 Time series of groundwater elevation at S16 compared with the total pumped water: (a) simulated water level in the whole period (1954-2008); (b) zoom on the period between 2006 and 2008.

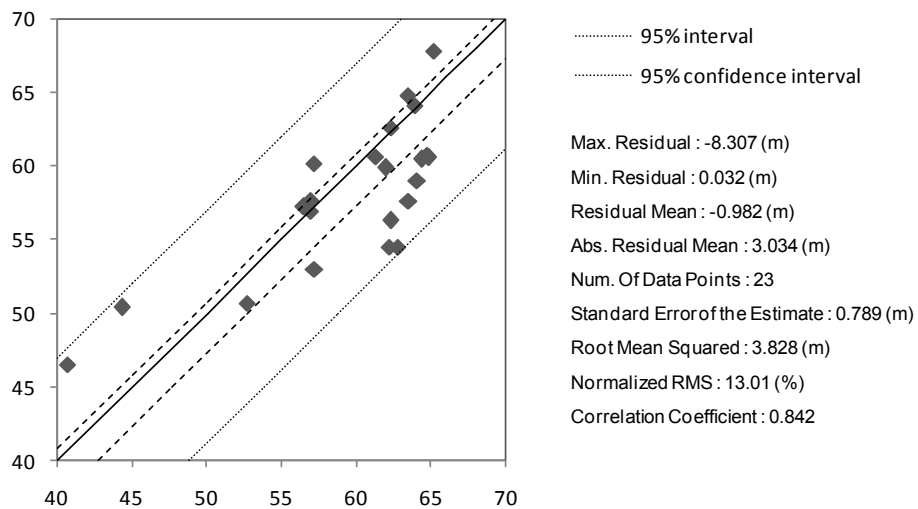
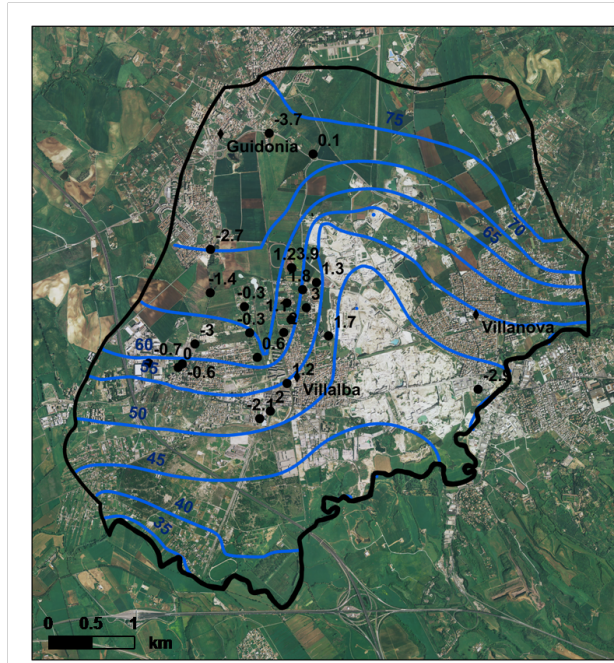


Figure 5.10 Piezometric surface calculated for the year 2003 and scatter chart "simulated values vs. observed values" related to March 2003. The point values indicate difference between the piezometric height measured and that for the targets.

The piezometric survey of 2003 (Petitta & Del Bon) was chosen to show the validation results. The comparison of the observed and simulated heads (Figure 5.10) shows good agreement for the points in the area of damage and the area of interest; the calculated values at the targets located distant from the central part of the model show higher values of residuals (mean error = -0.98 m, standard deviation = 3.8 m and correlation coefficient = 0.84).

5.3. Advanced DInSAR analyses

Advanced Differential Interferometric SAR (A-DInSAR) analyses were performed to acquire information regarding past displacements that affected the ground surface over the entire investigated area beginning in 1992. A-DInSAR is the only technique able to provide quantitative past displacement information with a high spatial density and millimetre accuracy. A-DInSAR techniques can take advantage of more than 20 years of archived SAR images. From this perspective, they represent an important tool for the detection and estimation of past displacements. These techniques have been successfully applied in earth deformation investigation, in particular for urban subsidence (Burbey, 2002; Damoah-Afari *et al.*, 2008; Raucoules *et al.*, 2007; Heleno *et al.*, 2011; Osmanoglu *et al.*, 2011; Bock *et al.*, 2012).

5.3.1. Performed analyses

To attain subsidence information this is distributed as well as possible in time, 198 ERS and Envisat archive SAR images in both the ascending and descending acquisition geometries and spanning from June 1992 to September 2010 (Tab. 5.4) have been provided by the ESA in the framework of the CAT-1 project “Geological reconstruction and monitoring in recently urbanised areas affected by subsidence.” The SAR data present temporal gaps between the two stacks of images, ERS and Envisat. Specifically, for the ascending geometry, we do not have data from 12/11/2000 through 15/11/2002, whereas for the descending geometry, the temporal gap goes from 19/02/2001 to 09/11/2002. Moreover, the ERS data-stack has a non-negligible time gap in the time interval November 1993 - May 1995.

Tab. 5.4 SAR data sets used in this work: time span, incidence angles θ (degree), azimuth ϕ (degree) and number of available SAR images N .

<i>InSAR set</i>	<i>Time span</i>	ϕ (degrees)	θ (degrees)	N
ERS , Track 172 (ascending)	28/4/1993 - 2/9/2000	-16	23	29
ENVISAT, Track 172 (ascending)	16/11/2002 - 21/8/2010	-16	23	51
ERS , Track 79 (descending)	11/6/1992 - 18/2/2001	161	23	68
ENVISAT, Track 79 (descending)	10/11/2002 - 15/8/2010	161	23	50

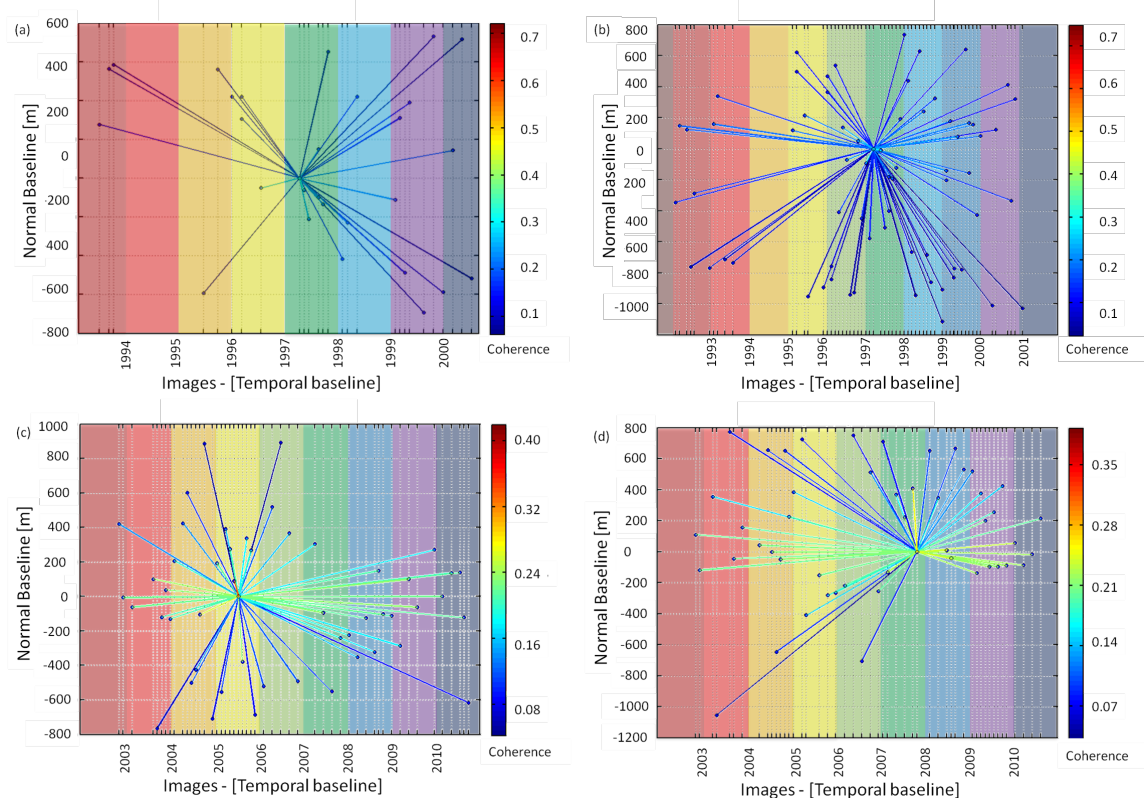


Figure 5.11 Graphs used to connect images relating to temporal baseline (X axis) and normal baseline (Y axis). Every dot represents an image, while every line represents an interferogram. Every image is connected to a master one, approximately in the centre of the graph space. Line colours from blue to red show increasing value of spatial coherence. The four datasets are respectively: ERS ascending (a), ERS descending (b), Envisat ascending (c), Envisat descending (d).

In this study, we obtained ground subsidence measurements using proprietary procedures implemented in SARproz (Perissin *et al.*, 2011). Specifically, we adopted a hybrid approach based on the PS InSAR (Ferretti *et al.* 2001) and Quasi-PS InSAR (QPS) techniques (Perissin & Wang, 2012), which are based on having no redundant interferograms computed by connecting SAR images in order to maximise spatial coherence. The core idea of the hybrid approach is to take advantage of the temporal continuity coming from the standard PS InSAR techniques to aid phase unwrapping and thus to obtain more robust time series of displacements. However, interferograms computed from the SAR images connected with the QPS approach are characterised by higher spatial coherence, increasing the achievable information from the analysed set of points.

Four available data-stacks of images were cropped to extract a 10 km x10 km subarea, and they were then processed independently by selecting a single master image and by co-registering all slave images with respect to it (Figure 5.11).

The analysis was performed through two main approaches:

- i) full-site processing that allowed us to derive deformational trends of the entire area; and
- ii) local-scale processing on some specific areas of interest, to analyse displacement time series point-by-point, thus also identifying non-linear deformation behaviours over time.

5.3.1.1. Full-site analyses

For the full-site analyses, PS candidates (PSC) were selected based on a combination of several quality parameters related to radar signal stability, such as reflectivity, Amplitude Stability Index (ASI, i.e., the amplitude coefficient of variation) and the spatial coherence. A network of PSC was created to estimate the preliminary height and velocity parameters to retrieve and remove the Atmospheric Phase Screen (APS). After the APS removal, a second estimation of parameters was performed on a wider set of points, selected based on a spatial coherence and ASI combination criterion. At the end of the PS analyses, all PSs with temporal coherence above a reliable threshold (primarily dependent on the number of images analysed in the data-stack) were selected.

For each PS, the LOS velocity, displacement time series and heights have been computed using a linear deformation trend model. Displacements have been related to a reference point located outside the Acque Albule Basin where the carbonate bedrock outcrops. The absence of compressible layers allowed us to assume that the geological and geotechnical conditions in this area had prevented the onset of the subsidence process that has occurred in the Acque Albule Basin.

5.3.1.2. Local-scale analyses

Local scale analyses have been performed on some portions of the basin involved in the dewatering process following the outcomes derived from the geological setting and hydrogeological modelling described in 5.2.1.1. In particular, the primary objective of the

local scale approach was to perform in-depth A-DInSAR analyses characterised by a stronger control on the single PS displacement time series.

We separately analysed some sectors of the basin with an area less than 2 km² (Figure 5.18). These sectors have been identified based on a geological-geomorphological criterion: each includes stable areas (where Alban volcanic deposits and/or Plio-Pleistocene marine deposits outcrop) and a portion of the plain where compressible deposits outcrop.

This method helped us select reference points, which were located in the stable areas mentioned above. PSCs were then chosen based on an ASI threshold value of greater than 0.6. In this approach, we did not perform the estimation and removal of APS as we assumed the atmospheric perturbations were negligible, with a correlation distance of less than 1 km (Hanssen, 2005). In this way, we avoided the risk of losing displacement phase components wrongly considered to be atmospheric artefacts. Moreover, the displacement estimation has been performed via a low pass filter in the time domain, specifically designed to detect and measure non-linear deformation behaviours. As expected, the PSs are primarily located in urban areas.

The final results have been selected by applying a high temporal coherence threshold, thus selecting only pixels characterised by a temporal coherence greater than 0.8 to attain only reliable time series.

5.3.2. Results of A-DInSAR analyses

The subsidence rates of the full-site processing data are summarised in Figure 5.12 (ERS period) and Figure 5.13 (Envisat period); to improve the visibility of the results, the PS were averaged within a regular grid (cell dimensions: 50 m x 50 m). In (a) and (b), we show the averaged LOS velocity map obtained for the ascending and descending geometries. Because the results from both geometries were available, the vertical and horizontal components could be derived. The global deformation process expressed a primarily vertical direction of displacement with a negligible horizontal component, as expected for a subsidence process. In (c), the so-derived vertical component of deformation is depicted. In the LOS displacement maps (a and b), negative velocities (from yellow to red) represent movements away from the satellite, and positive velocities (from light blue to dark blue) represent movement towards the satellite. In the vertical

displacement map (c), negative velocities (from yellow to red) represent downward movements (i.e., subsidence), and positive velocities

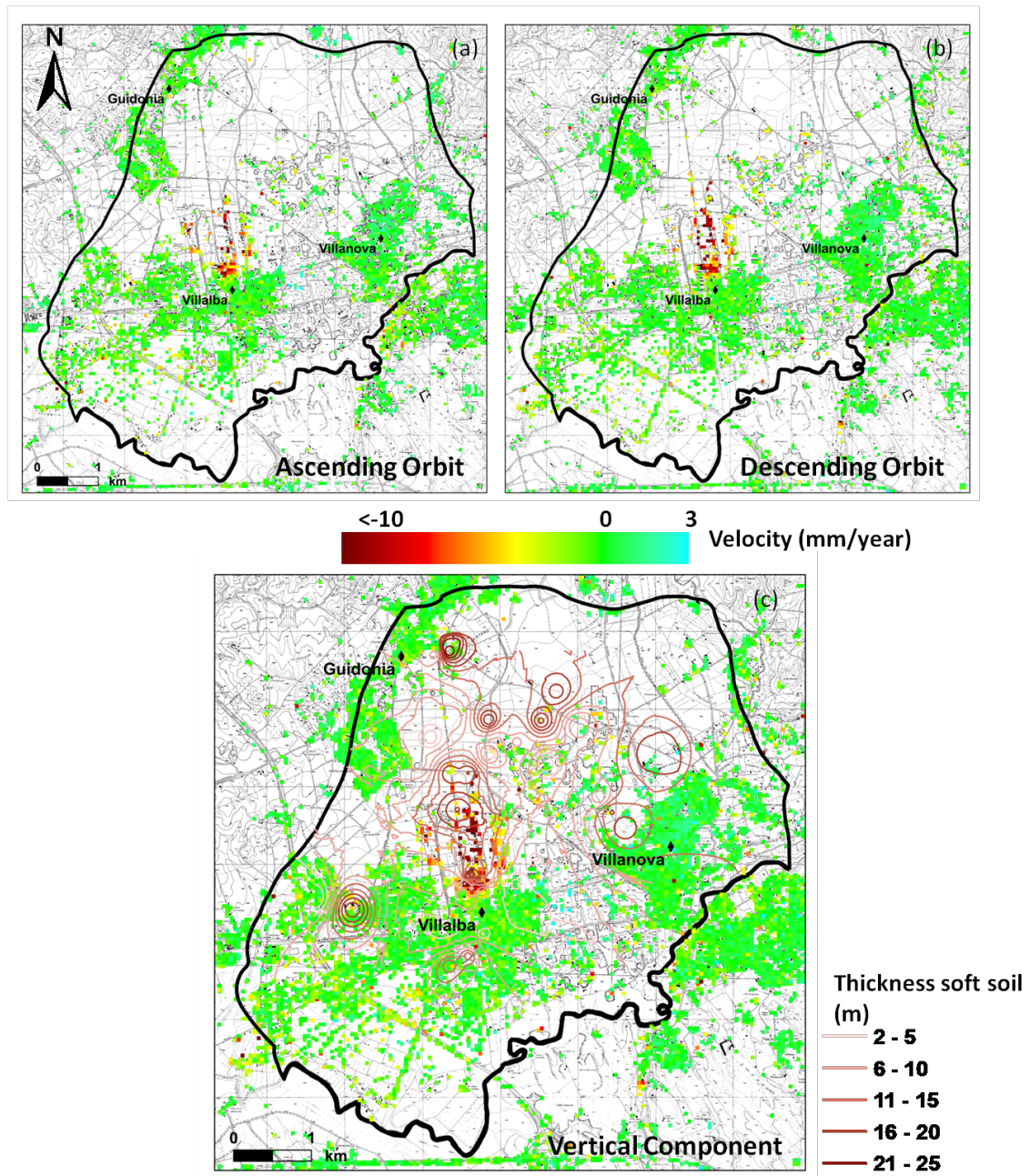


Figure 5.12 Average 1993–2000 velocity maps of the Acque Albule Basin. In (a) and (b) we reported LOS velocities. Vertical component (in millimetre/year) have been extracted using ascending and descending acquisition (c). In LOS displacement maps (a and b), negative velocities (from yellow to red) represent movements away from the satellite while positive velocities (from light blue to dark blue) represent movement towards the satellite. In vertical displacement map (c), negative velocities (from yellow to red) represent downward movements (i.e. subsidence) while positive velocities (from light blue to dark blue) represent upward movements (i.e., uplift). Green points indicate stable areas. In (c) surface geology contours of the compressible deposits is shown. Ground subsidence is clearly visible on vertical deformation map. In (b) we reported the reference point (pink circle) located outside the Acque Albule Basin where the carbonate bedrock outcrops.

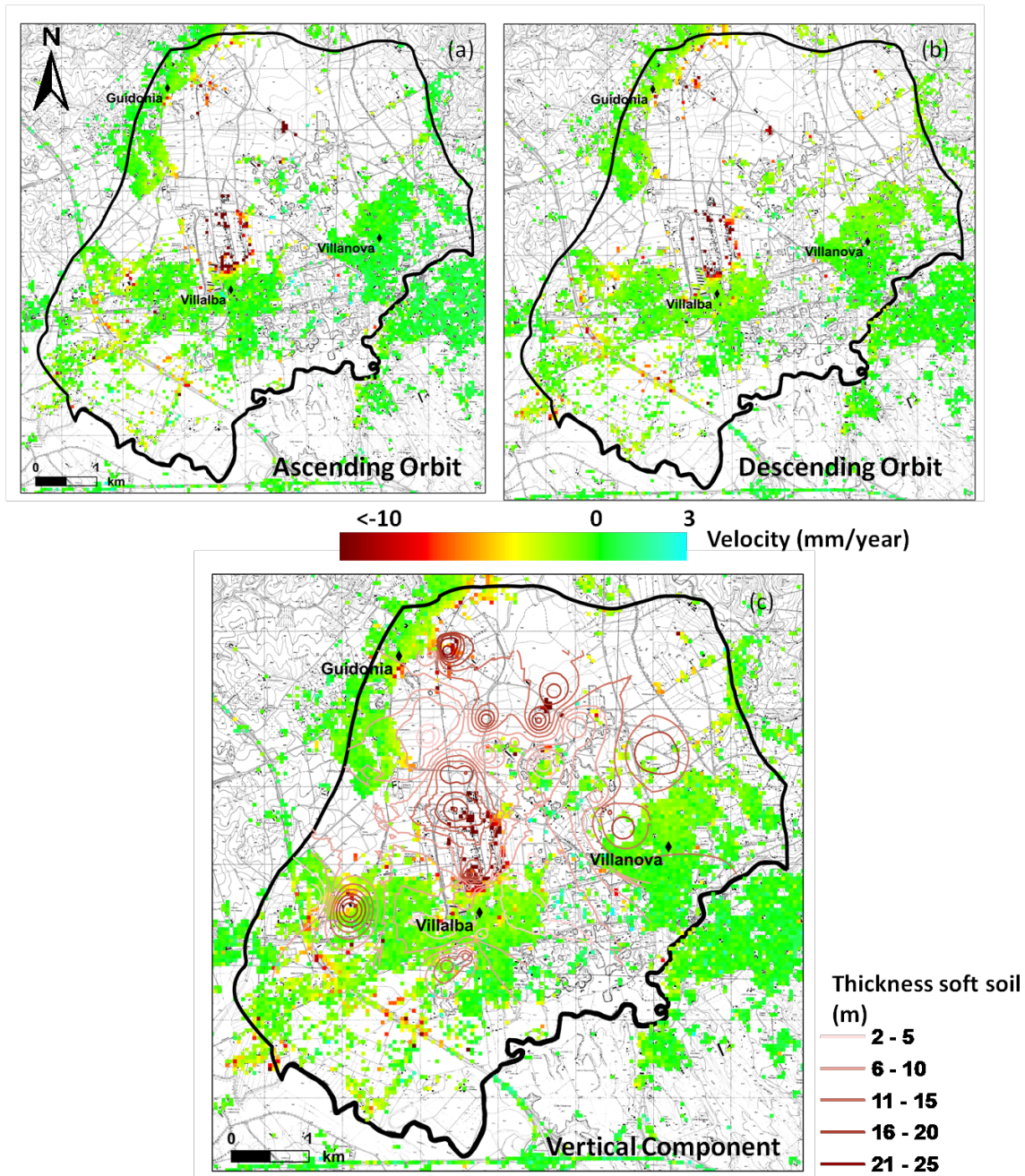


Figure 5.13 Average 2001–2010 velocity maps of the Acque Albule Basin. In (a) and (b) we reported LOS velocities. Vertical component (in millimetre/year) have been extracted using ascending and descending acquisition (c). In LOS displacement maps (a and b), negative velocities (from yellow to red) represent movements away from the satellite while positive velocities (from light blue to dark blue) represent movement towards the satellite. In vertical displacement map (c), negative velocities (from yellow to red) represent downward movements (i.e. subsidence) while positive velocities (from light blue to dark blue) represent upward movements (i.e., uplift). Green points indicate stable areas. In (c) surface geology contours of the compressible deposits is shown. Ground subsidence is clearly visible on vertical deformation map.

(from light blue to dark blue) represent upward movements (i.e., uplift). Green points indicate stable areas.

Superimposed on the c map, we also reported the contour map of the thickness of the compressible deposits.

Our next focus is on three specific sectors of the plain whose deformational behaviour is particularly significant to understand the overall investigated process. These sectors, described more in detail (black boxes in Figure 5.14, Figure 5.15 and Figure 5.16), are the “Central” sector (which includes the town of Villalba), the “Northern” sector (which includes the town of Guidonia) and the “Western” sector (south-west of the town of Villalba).

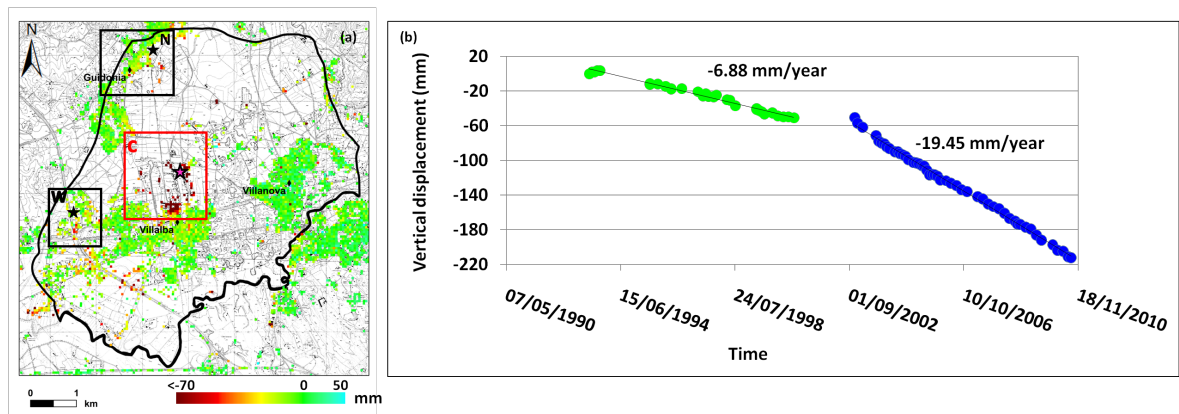


Figure 5.14 In (a) outlined in red is Central sector studied in more details. (b) Vertical displacement time-series and corresponding linear rates of subsidence. ERS (green) and Envisat (blue) time series are shown.

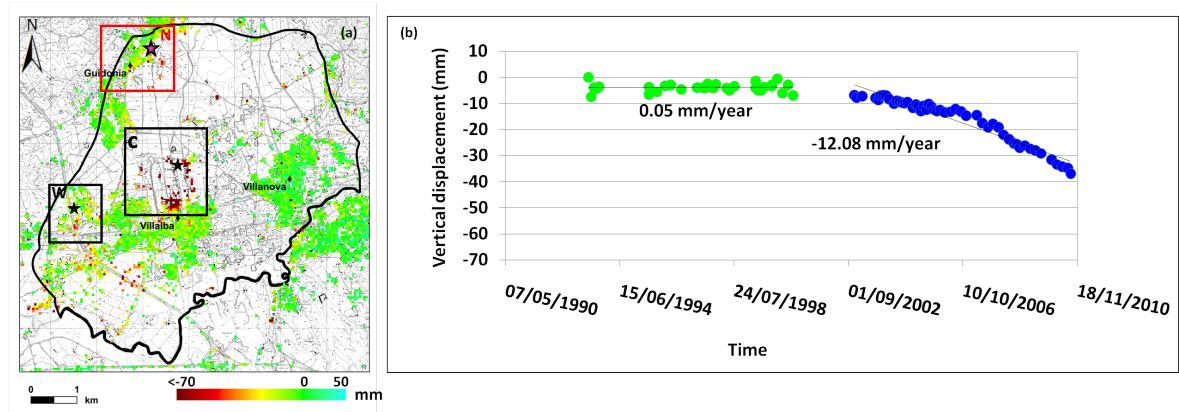


Figure 5.15 In (a) outlined in red is Northern sector studied in more details. (b) Vertical displacement time-series and corresponding linear rates of subsidence. ERS (green) and Envisat (blue) time series are shown.

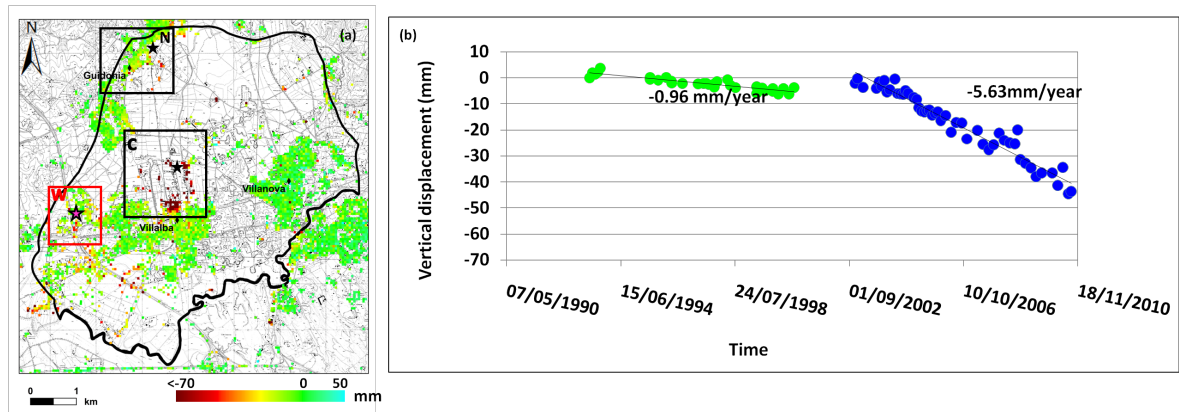


Figure 5.16 In (a) outlined in red is Western sector studied in more details. (b) Vertical displacement time-series and corresponding linear rates of subsidence. ERS (green) and Envisat (blue) time series are shown

The Central sector (Figure 5.14), very close to the open pit area, was affected by average deformation rates ranging from 3 mm/y to 10 mm/y during 1993–2000. From 2003 to 2010, the subsidence rate was greater than in the previously investigated period and presented an average deformation rate ranging from 10 mm/y to 25 mm/y. In this sector, the thickness of the compressible deposits exceeds 20 meters. The displacement time series show a continuity of the process over time, with a slight increase in the rate of subsidence in the Envisat period. The vertical displacement time series and corresponding linear rates of subsidence are presented in Figure 5.14 b.

The Northern sector (Figure 5.15 a), located 3 km north of the open pit area, appeared to be stable during 1993-2001, whereas it was subsiding in 2003-2010, with deformation rates ranging between 10 mm/y and 15 mm/y. The vertical displacement time series and corresponding linear rates of subsidence are presented in Figure 5.15 b.

In contrast with the Northern sector, the Western sector is characterised by stronger urbanisation. A very localised area, distinguished by higher compressible deposit thickness, shows slight subsidence in the ERS data, most likely due to the induced load. However, (Figure 5.16), similarly to the Northern sector, the Western sector widely experienced subsidence in 2003-2010, with deformation rates ranging between 5 mm/y and 10 mm/y. The presence of a bowl-shaped area of subsidence highlights the spatial distribution of the compressible deposits, whose maximum thickness (in the centre of this sector, see Figure 5.12 c) was found in the wetlands and lakes as described in section 2.1. The vertical displacement time series and corresponding linear rates of subsidence are presented in Figure 5.16 b.

Otherwise, some remaining portions of the study area had essentially no deformation until 2010. They are located towards the west and the east of the basin. These two areas are located on Albano-volcanic formations and on old Plio-Pleistocene formations and carbonate rocks, respectively. In addition, in some zones within the basin where travertine deposits outcrop, no deformation is detected.

5.4. Diagnosis of the subsidence process

The results of the A-DInSAR analyses have been interpreted by accounting for the local geological features and the spatial and temporal piezometric evolution over time to attain a comprehensive interpretation of the subsidence process and to derive more insight into the triggering factors.

As discussed above, the piezometric surface has been effectively modelled from 1954 to 2008, thus highlighting the effects induced by pumping over time. Specifically, the underground water cone caused by the quarry activities gradually deepens and affects a wider portion of the plain (Figure 5.17), ranging from -3 m of drawdown in 1969 to -8 m in 1992 in the open pit area. Then, beginning in 1998, when the extraction of water reached approximately $1.5 \text{ m}^3/\text{s}$, the water table underwent a sharp decrease, reaching -18 m in 2001. In 2008, when the extracted water was approximately $4 \text{ m}^3/\text{s}$, the water table reached a depth of 32 meters b.g.l. Furthermore, the dewatering cone has extended over years, thus affecting portions of the plain farther away from the main quarry area.

The Central sector is affected by the decrease in the water table by 4 meters in 1998. In 2008, the simulated drop reaches 10 meters.

The simulated piezometric surface in the Northern sector underwent a decrease of less than 1 m in 1992. In 1998, the decrease was between 1 m and 2 m; in 2001, it reached 4 m. In 2006, the drop was between 4 m and 6 m. At the end of 2008, the decrease was between 6 m and 8 m. (Figure 5.17).

In the Western sector, the decrease was less than 2 m until 2001, and it reached 4 m at the end of 2008.

The overall mechanism linking the piezometric surface variations and the detected subsidence phenomenon in time is thus explained: when water is pumped from the travertine aquifer, whose piezometric level roughly coincided with the ground level under undisturbed conditions, a gradient is created, thus causing a water pressure reduction in the

compressible soils on top of the travertine bedrock. As a result of the water pressure decrease in the compressive soil pores, these soils experienced a consolidation process.

The A-DInSAR data showed a good relationship with the simulated piezometric level changes, thus allowing for the identification of different patterns of ground surface behaviour in the study area.

Specifically, the ground deformations that occurred between 1993-2001 were localised in the areas affected by the cone of depression caused by the pumping activities in the quarry areas. However, although the areas with travertine outcrops showed minimal or null deformation, the areas characterised by the presence of compressible deposits showed vertical deformations proportional to the variations in piezometric level (Central sector). Furthermore, the areas characterised by compressive deposits, where the decrease in the piezometric level did not occur, did not experience detectable deformations (Northern sector and Western sector) (Figure 5.17).

The same linear relationship between the decrease in the piezometric levels and the vertical deformations is confirmed in 2003-2010. In this period, the cone of depression had expanded and deepened in time and in space, affecting the entire basin, and the PS data clearly show the appearance of new areas of subsidence (Figure 5.17). The areas newly affected by subsidence are located where the thickness of the compressible materials is greater (Northern sector and Western sector). In addition, in this case, the interferometric data returned negligible LOS displacements in areas where the travertine locally outcrops. Hence, the full-site A-DInSAR analyses were able to define the overall subsidence mechanism occurred in the Acque Albule plain: local geological conditions control the magnitude of the process, whereas its timing is driven by hydrogeological variations in time.

Moreover, the full-site A-DInSAR results represented a starting point for performing local-scale interferometric analyses. In particular, our objective was to deepen the understanding of subsidence trigger timing. As we observed in section 5.3.2, some sectors localised in the marginal areas of the Acque Albule Basin experienced the beginning of the subsidence process during the Envisat observation period. The main concept was to observe the evolution in time and space of the detected ground deformation with a more accurate time series of the displacements to better identify the triggering time within the Envisat observation period. As stated above (5.3.1.2), the absence of APS estimation and,

furthermore, the displacement estimation performed also using a ‘no-model’ approach (applied in these specific analyses), allowed for an increase in the reliability of the thus-attained time series because the time series are not influenced by any linear model, as was true in the full-site analyses.

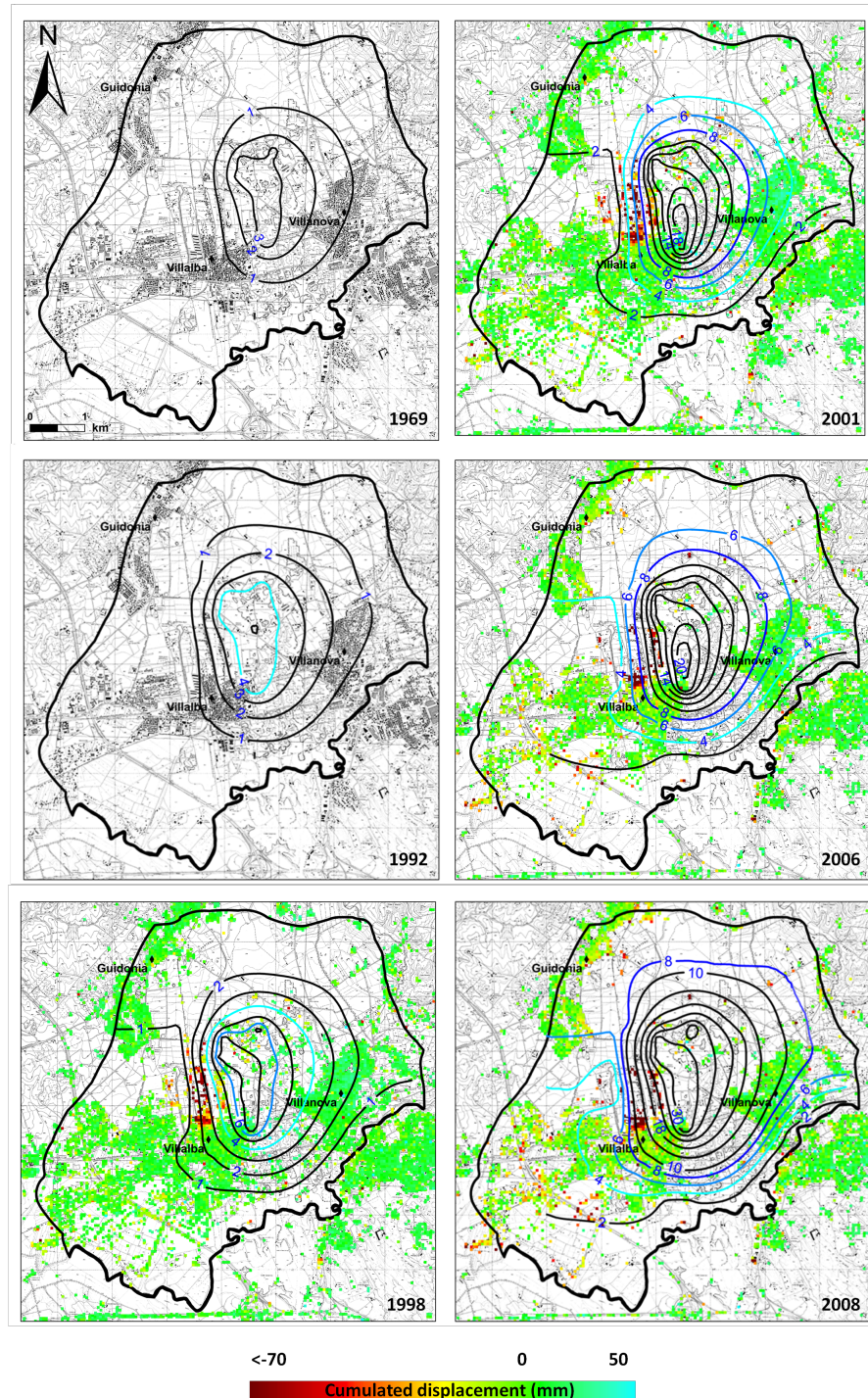


Figure 5.17 Evolution of the cone of depression induced by pumping overlaid on cumulated deformation maps for different time steps.

The results of the local-scale processing of the Envisat data are summarised in Figure 5.18. The time series characterised by non-linear behaviour clearly demonstrate how the process of subsidence expands over the plain. For the areas to the north and west, it was possible to understand when the process started. The time series of the Northern and Western sectors show two linear deformation trends with different velocities. In particular, the subsidence process is activated beginning at certain point in the displacement time series. For the Northern sector, it is possible to characterise three different trends in the deformation rate in the PS time series. In particular, from the observation of the time series in Figure 5.18a, no deformations could be detected up through 2004, whereas in 2004-2007, the cumulated displacements reached approximately 20 mm (i.e., 5 mm/y). From 2007 to 2010, a maximum deformation of 80 mm was reached.

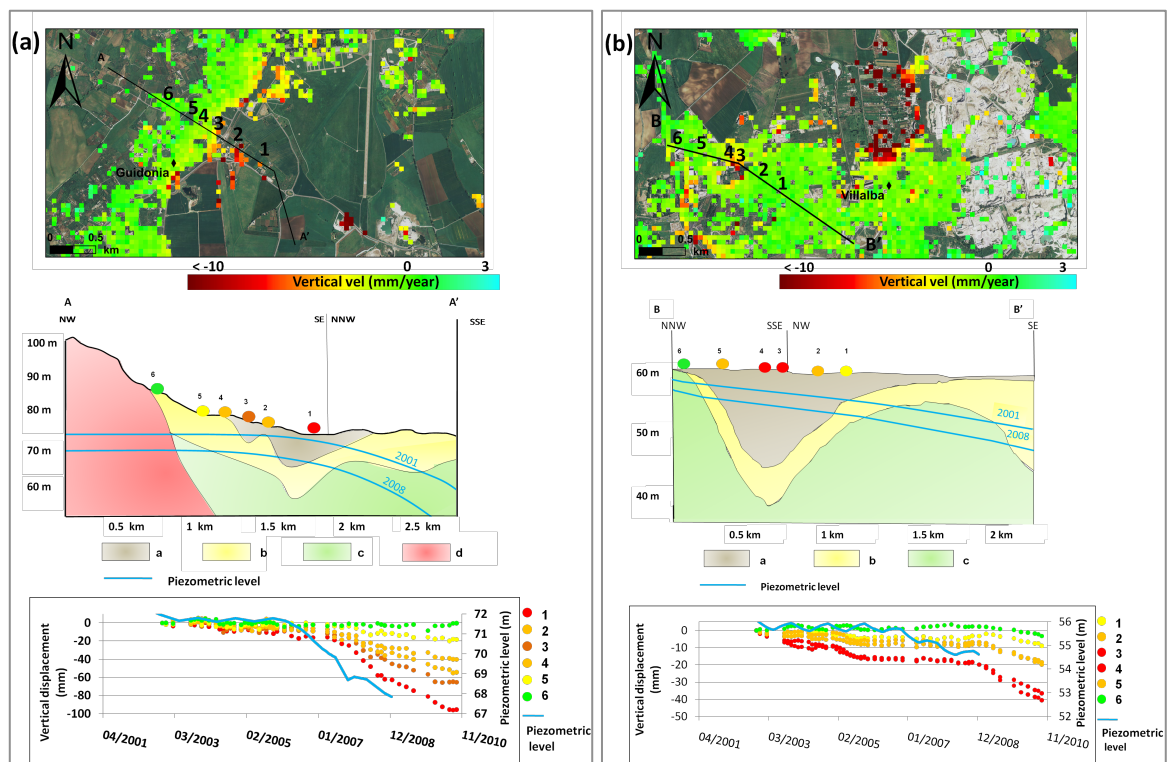


Figure 5.18 Local-scale result of Northern (a) and Western (b) sectors. We reported the geological sketches (with a strong vertical exaggeration) associated to the selected PSs as well as their location. Charts showing the relationships between the time histories of modelled dewatering and vertical displacement of selected PSs along sections. Key to legend: a) Organic clays and peats; b) Loose travertine; c) Travertine; d) Volcanic and sedimentary bedrock. Vertical scales are different to appreciate different piezometric variations in the two sites.

Comparing these results with the variations in the water table, the decrease in the water table in this area was less than 2 m until 2001, and it was between 4 m and 6 m in 2007. Finally, in late 2008, the drawdown was over 6 m. Therefore, the activation time of the subsidence in the Northern sectors is strictly related to the involvement in the cone of depression, whereas the magnitude of the process is governed by the local stratigraphy. This evidence is supported by the behaviour of some PSs farther from the pumping “epicentre” that experienced smaller vertical displacements than other points located closer. The associated stratigraphy reveals a thicker layer of compressible soils at the more distant points than at the closer points. We observed that the changeover between the areas with subsidence (orange to yellow colours in Figure 5.17) and areas without subsidence (green colours) occurred in a narrow zone, less than 1 km wide. The geologic data show that this area corresponds to the transition zone between the compressible deposits and volcanic and sedimentary bedrock.

A similar result was obtained for the Western sector, where we observed an acceleration of the process since 2008 (Figure 5.18b). The relationship between the geological setting and the hydrogeological variations is also here confirmed; in this case, even with a greater thickness of compressible deposits in the centre of the sector, the total vertical displacement is less because the decrease in the water table reached only 2-4 m in this area. To better constrain the relationship between the subsidence and the thickness of the compressible sediments, we assigned to each borehole (among the 97 available) the vertical cumulative displacement value measured for 1992-2008 using PSs included within different buffer areas with radii of i) 20 m; ii) 21 to 50 m; or iii) 51 to 100 m (assumed as representative considering the lateral heterogeneity of the distribution of the deposits).

However, 20% of the boreholes had no available PSs sufficiently close for a significant comparison. Few PSs (5% of total) are included within the area defined by a 20 m buffer; 55.7% of the total PSs are included within the area defined by a 21-50 m buffer; and 18.7% of the total PSs are included within the area defined by a 51-100 m buffer.

Figure 5.19 shows the correlation between the thickness of the compressible deposits, the decrease in the water table and cumulative displacement. Specifically, for a thickness of compressible deposits averaging less than 6 m and a drawdown less than 4 m, the cumulative displacement does not exceed 4 cm, whereas for a thickness greater than 6 m and a drawdown greater than 4 m, the cumulative displacement is greater than 4 cm. This

correlation is sufficiently strong, and yet, this analysis does not include the construction quality of the buildings, the typology of the foundations and the terrain-foundation interactions, although in the A-DInSAR analysis, structures themselves very often represent the targets that the backscatter phase signals related to the deformation measurements.

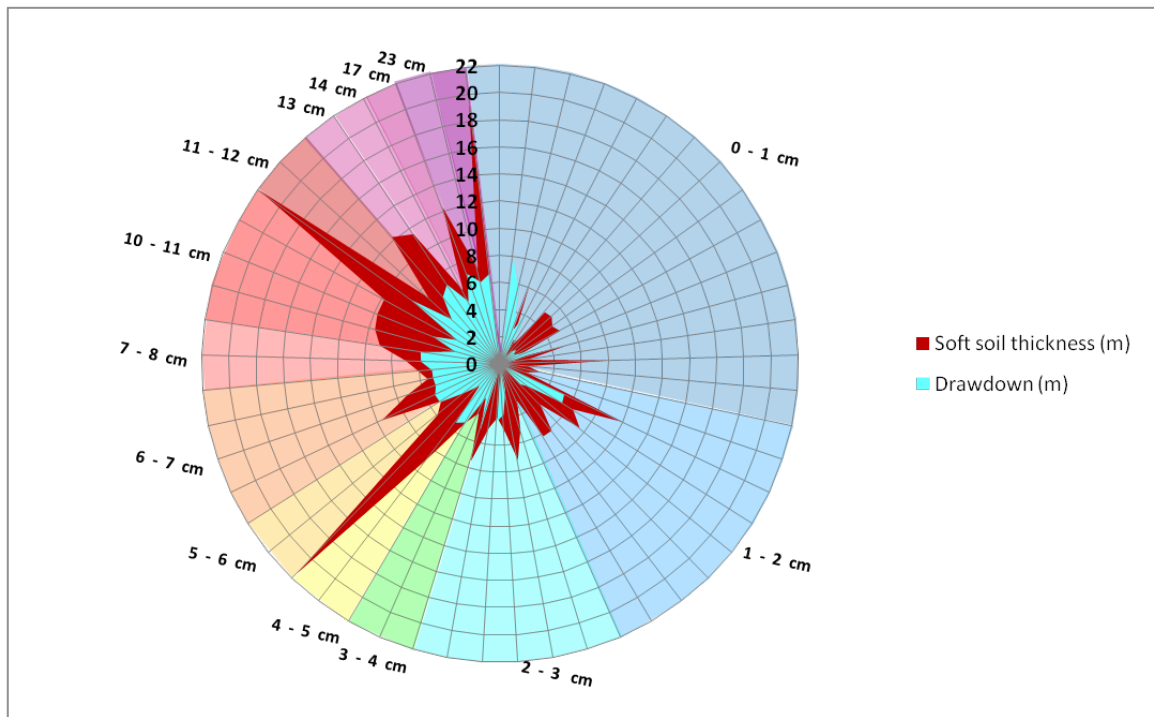


Figure 5.19 The graph shows for each borehole (which corresponds to a radius) data of the thickness of the compressible deposits and drawdown (expressed in meters, vertical scale bar) and vertical cumulated displacement (expressed in centimetres, along circumference).

5.5. Conclusions

Using the combination of geological and geotechnical data with hydrogeological modelling calibrated on piezometric data-set, we were able to explain the spatial and temporal evolution of a subsidence process related to the huge groundwater drawdown experienced in the last decades in a recently anthropogenically stressed area.

The subsidence process has been thoroughly quantified in the time interval 1993-2010 by satellite A-DInSAR analyses performed on four different datasets acquired in double orbital geometries.

The investigations carried out confirm both the overall process on a wide scale and the local behaviours analysed in detail using ad hoc interferometric analyses, combined with local engineering-geological stratigraphic conditions.

The specific role of the main controlling factors has been well constrained by the here performed diagnosis of the already occurred subsidence process: the groundwater level variations drive the timing of subsidence triggering over the area, whereas the local geological conditions – i.e. the thickness of the compressible deposits overlaying the travertine in its turn hosting the exploited aquifer - drive the magnitude of the deformation process.

The back-analysis case history here discussed encourages the research toward the forecasting of the on-going evolution of the subsidence process caused by groundwater exploitation in geologically well-known areas. Systems mainly based on the continuous monitoring of the groundwater levels by means of a network of piezometers distributed in the area could be able to anticipate either the onset or the acceleration phases of the subsidence. We thrust that the coupling of such a type of monitoring network with sporadic satellite and ad-hoc planned A-DInSAR analyses could be a very efficient self-controlling monitoring platform.

Acknowledgments: The present work is within the framework of a research project (PRIN 2009 – “Analysis, monitoring and control of geological instability interacting with human activities”) funded by the Italian Ministry of Education, University and Research (MIUR). A-DInSAR analyses have been carried out thanks to the European Space Agency, in the framework of the Cat-1 project “Geological reconstruction and monitoring in recently urbanized areas affected by subsidence” (Id 13097)

6. POTENTIAL FOR A-DInSAR TO PREDICT THE TIME OF FAILURE OF SLOPES

6.1. Introduction

Landslides represent a major risk for human life and activities, causing severe socioeconomic impacts on people, their homes, industrial establishments, and lifelines, such as highways, railways, and communications systems (Schuster & Highland, 2001). Landslides can be considered as a part of the natural evolution of slopes; nevertheless, human activities and the growing pressure due to infrastructure and building expansion over unstable areas can cause or accelerate already existing slope instability processes (Muller, 1964; Olshansky, 1996; Schuster & Highland, 2001; Bozzano *et al.*, 2010).

Remote sensing contributes to landslide risk reduction at several stages, from susceptibility mapping (usually integrating data into geographic information systems) (Sarkar & Kanungo 2004; Ayalew & Yamagishi, 2005; Lee, 2005; Hong *et al.*, 2007) to the monitoring of landslides performed using a variety of methods, both ground based and air/space-borne (Gigli *et al.*, 2011; Arattano & Marchi, 2008; Bozzano *et al.*, 2011, Qiao *et al.*, 2013; Bozzano *et al.*, 2014). However, generally speaking, in landslide risk reduction, a key role is also played by the prediction of the time of failure, based on quantitative data. Landslides rarely behave as a rigid body that responds instantly to stresses. More frequently, they are characterised by a strain pattern (hence, displacements), increasing over time (Siddle *et al.*, 2007). Therefore, time-dependent failure relationships must be considered to describe the long-term deformation pattern known as “slope-creep” (Terzaghi, 1950; Haefeli, 1953), which represents the slow deformation of slopes involving soil and rock, occurring under gravity and external loading (Emery, 1979). In the creep model, the materials show a particular evolution of the strain pattern characterised by three phases: a primary creep, a secondary creep and finally, a tertiary creep, in which continuous strain acceleration leads the material to failure (Figure 6.1).

Beginning in the 1960s, several authors (Saito & Uezawa 1961, Saito 1965, 1969) tried to investigate landslide failure prediction using observational methods. From laboratory experiments, observed that the displacements are the best parameter to get information about the time before failure. In 1965 he applied this methodology to the prediction of the time of failure of a slope.

Through the results of large-scale experiments observing surficial displacements, Fukuzono (1985) demonstrated the proportionality between the logarithm of velocity and the logarithm of acceleration. From this relationship, several authors (Voight, 1989; Crosta & Agliardi, 2003; Bozzano *et al.*, 2011; Mazzanti *et al.*, 2011) attempted to predict landslide failure using semi-empirical models based on the slope creep theory, in which the time of failure is defined using the inverse velocity of displacement vs. time. In a graph of the reciprocal of the velocity vs. time, you can identify the landslide time of failure from the intersection of the function with the time axis (Figure 6.2).

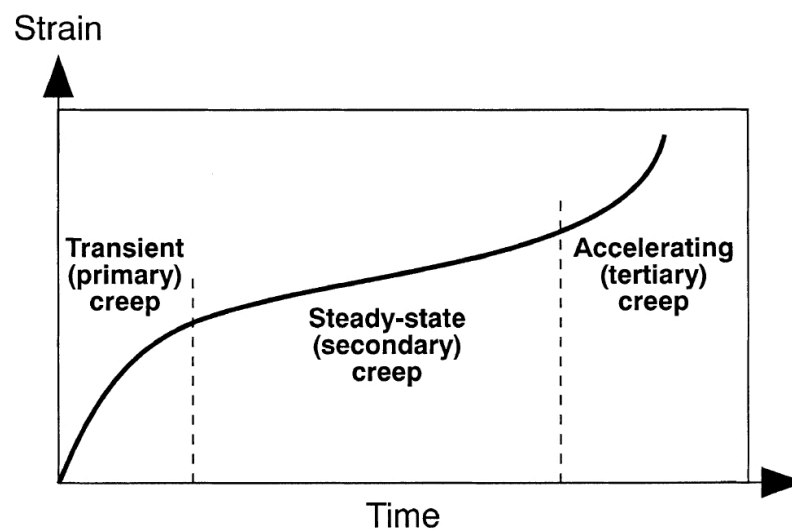


Figure 6.1 Time-dependent strain behaviour according to the creep principle. The behaviour separates into three phases of transient, steady-state and accelerating creep (from Main, 2000).

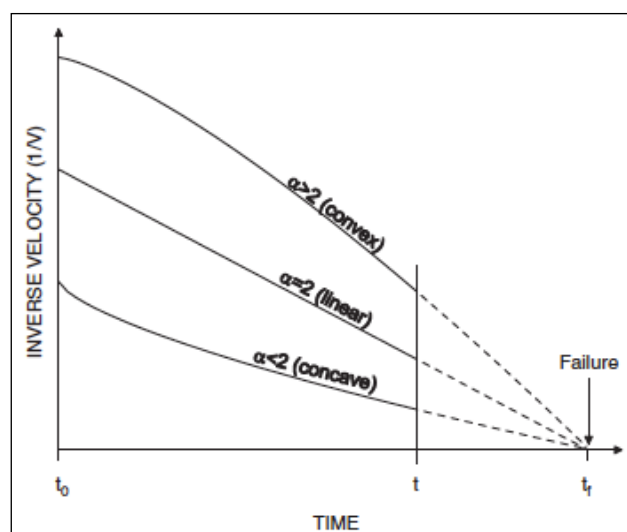


Figure 6.2 Inverse-velocity versus time relationship preceding slope failure – (from Rose & Hungr, 2007, after Fukuzono, 1985).

The models of landslide prediction using displacement time series (Saito & Uezawa, 1961; Saito, 1965; Fukuzono, 1985; Voight, 1989; Crosta & Agliardi, 2003; Bozzano *et al.*, 2011; Mazzanti *et al.*, 2011) are hence based on the assumption that the collapse of the slopes is preceded by creep behaviour characterised, in its final stage, by an acceleration of movement in time.

The continuous collection of displacement data is a key requirement for the application of semi-empirical models. Therefore, displacement monitoring systems play a relevant role in landslide failure prediction (Mazzanti *et al.*, 2012). In the observational approach, the availability of displacement data characterised by a good distribution in space (i.e., the capability of attaining information about several portions of the slope under investigation) and high sampling frequency in time is a crucial point. Consequently, the role of monitoring is essential to collecting accurate and detailed data in both space and time. As highlighted by Mazzanti *et al.* (2014), the back-analysis of large landslides (such as the Vajont landslide in 1963 in Italy) (Kilburn & Petley, 2003) has demonstrated the effectiveness of these semi-empirical methods based on a time series of displacements. However, it is also shown by the literature the difficulty of predicting the time of failure for existing landslides (Crosta & Agliardi, 2003).

The typology and methodology of monitoring systems is a key point for the successful application of these methods. In particular, the temporal resolution of data is very important for properly detecting the acceleration stage for a slope suffering creep evolution over time. Considerable progress has been made in this regard in recent years, in particular in the field of remote sensing. A monitoring system based on the same functional principle as A-DInSAR (namely Terrestrial SAR Interferometry, TInSAR) observed the predictability of landslides on the basis of semi-empirical models. In addition to the widespread distribution of the data in the observed scenario (to overcome another typical limitation of classical monitoring systems, which typically observe a limited number of control points), TInSAR was very useful for the high temporal frequency of data acquisition (up to a few minutes) as well as for the high accuracy and precision (up to 0.1 mm) (Bozzano *et al.*, 2010, 2011, 2012; Gigli *et al.*, 2011; Mazzanti *et al.*, 2011, 2014).

6.2. Detection of non-linear processes by A-DInSAR

As we stated above, to properly address the failure mechanism of the slopes affected by instability processes, the ability to recognise and quantify the acceleration stage preceding the failure is fundamental.

Is A-DInSAR able to detect acceleration/deceleration stages within a given observational period? In other words, is it able to provide information in the form of non-linear time series of displacement (typical of creep evolution)?

Starting from the case study presented in section 5 of this PhD thesis, some general considerations can be made to take advantage of comparisons between different approaches applied in SAR data analysis.

First, even with a linear model used to infer the displacement phase component, it is possible to detect some non-linear signals within the time series. Cigna *et al.* (2011, 2012) presented a PSInSAR post-processing method to handle this type of time series to extract more detailed temporal information from standard PS results. However, this is possible only if these residual signals are not strong enough to generate a severe deviation from the chosen model, thus causing the temporal coherence to be too low, which could cause such results to be removed from further post-processing steps due to the quality thresholds used to retain only reliable results. On the contrary, the discussion in this Chapter focuses on different data processing approaches performed with manual time series analysis without applying models to unwrap the displacement phase signal. In this way, a more effective control is instituted upstream in the data processing flow, thus reducing the risk of losing information in later steps. In contrast, analyses performed using this type of approach are more time-consuming, and they need operators dually skilled in both InSAR data analysis and the investigated deformation phenomena.

For the case study under consideration, the Envisat ascending results from the full-site analyses related to the Northern sector of the Acque Albule Basin (see section 5) provided some interesting information regarding the temporal evolution of the ground instability process (Figure 6.3). In particular, we found that some PSs show LOS displacements marked by velocities ranging from -2 mm/y to -5 mm/y, and they are characterised by quite low temporal coherence ranging from 0.61 to 0.63. Even with a less strict threshold for the temporal coherence value (say 0.65), we would lose these points from further investigation.

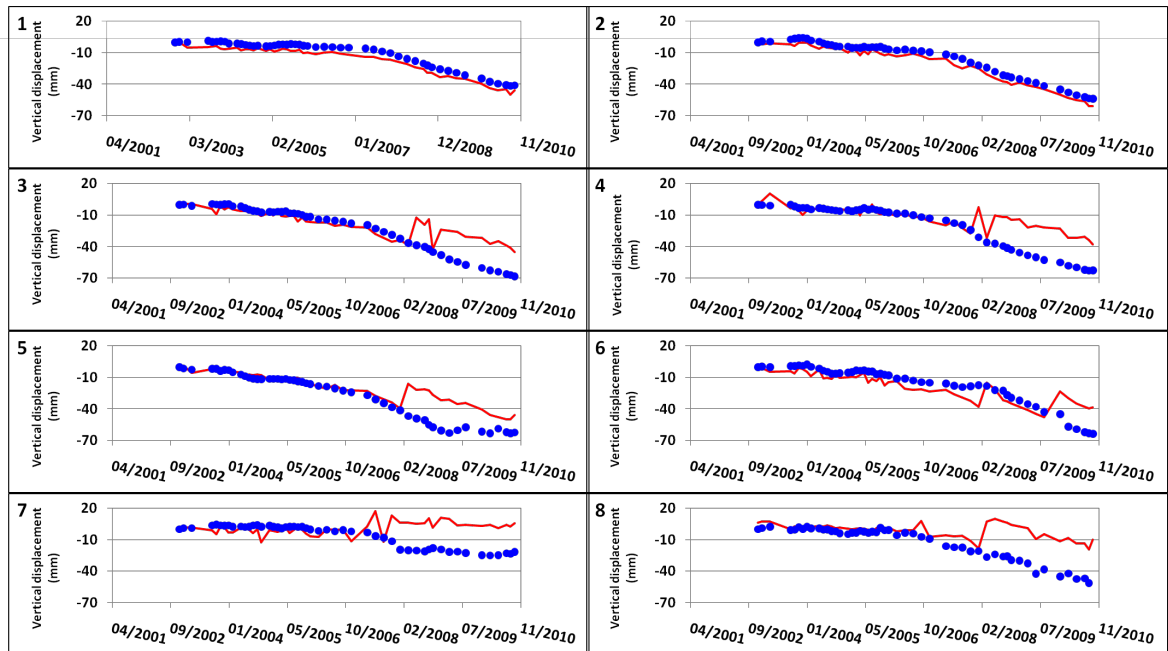
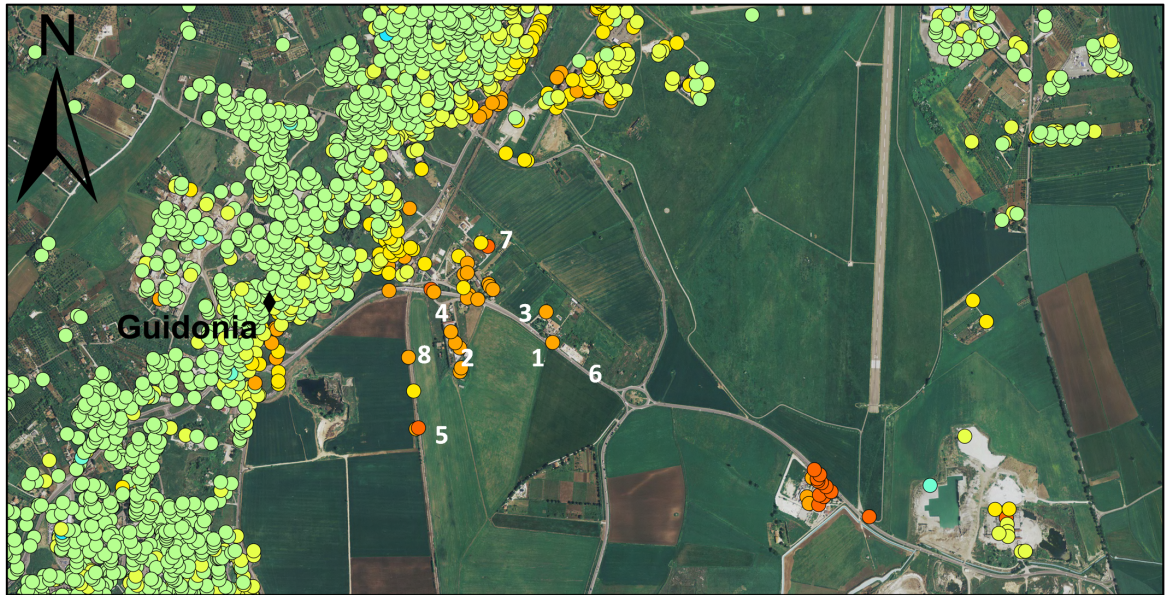


Figure 6.3 Comparison between full site (linear modelled displacement) and local scale (no-model) analyses performed over same PSs in the northern sector.

Examining the time series of displacement of these points in more detail (Figure 6.3-1, Figure 6.3-2), a particular trend is recognisable, ascribable to two linear deformation trends with different velocity behaviour in time (red line). Moreover, the time series of deformation depicted are quite clear and noise-free. The low temporal coherence attained for such points is primarily linked to the divergence of the phase component related to the displacement (more generally: experimental data) from the model used (linear model to derive the displacement component).

Local-scale analyses performed on the same data in the same area with a no-model approach confirmed what we foresaw in the full-site results. As shown in Figure 6.3-1 and Figure 6.3-2, the time series of the same points derived by the above-mentioned model-independent approaches are similar (blue dots), thus confirming the observed deformational behaviour, which is not affected in this case by the APS estimation and displacement model. Moreover, the model-free analysis performed on a small area around such PSs provided even more useful information for the other PSs located nearby. In the latter case, the PS time series with two different approaches are significantly different because the linear model used to unwrap the displacement phase component was not able to detect the non-linearity (from Figure 6.3-3 to Figure 6.3-8). In this perspective, important information related to the temporal evolution of the investigated process would be lost with a standard PS analysis.

It is evident that some limitations strictly related to the A-DInSAR technical features still remain, such as the maximum displacement between any pairs of radar images (one-quarter of the wavelength of the signal, if no a-priori information is available) (Ferretti *et al.*, 2005). Using manual analysis of the displacement time series, it is possible to increase this limit to half of the wavelength, assuming only one direction, to explain the occurred displacements; for landslides, because the process is driven by the action of gravity, it is reasonable to consider that evolution occurs only downward. From this assumption, however, it is necessary to put into practice an interpretation concerning the phenomenon under analysis to reasonably explain the displacement values measured by satellite. For this reason, advanced (manual) A-DInSAR analysis should always be performed considering the nature of the observed process to not introduce serious errors into the results.

Moreover, this aspect is directly related to another parameter of crucial importance, which is the satellite revisit time characterising the SAR data-stack used in the investigation. If the revisit time is too long, the rapid processes could be not properly investigated, thus underestimating the true displacement. For this reason, the satellite revisit time is definitely one of the key parameters to be considered to assess the correct observation of a deformation process using A-DInSAR methods.

6.3. Database of creep evolution for monitored landslides

Because the discussion above (from a theoretical perspective) suggests the evaluation of the application of A- DInSAR to real cases of landslides, let us introduce some data relating to landslide case studies collected in the literature. The majority of this database has been collected by Froude (2011) and has been integrated with 14 case studies by digitising time series of displacement collected from the literature. Overall, we have a total of 42 time series of displacements for monitored landslides, allowing the observation of their evolution during the transition and development of the tertiary creep, until the occurrence of failure (Tab. 6.1). In addition to all of the basic information useful to characterise landslide phenomena (where available), the most important parameter for the topic under discussion here is the duration of the tertiary creep (final column), which is the elapsed time between the beginning of the displacement acceleration and the failure. As shown in Figure 6.4, the length of the Tertiary Creep period (TC) can vary substantially, depending on many factors: materials involved in the instability processes, landslide dimension, or the presence of loadings and other external factors influencing the stress conditions (intense rainfalls, snowmelt, human activities, or seismic events). However, following the philosophy of the observational method, we want to emphasise that when the period of deformation before the failure is long enough to be observed, it could be possible to apply the semi-empirical models that may allow predictive analysis. As stated by Mazzanti *et al.* (2014), the issue we are discussing is temporal in nature; to properly describe the process, you must have as many observations as possible. For the A-DInSAR techniques, this aspect is controlled by the revisit time of the specific SAR satellite. The parameter that allows us to define possible monitoring scenarios is thus provided by the ratio between the Tertiary Creep (TC) duration and the Revisit Time period (RT).

Tab. 6.1 Landslides database collected from literature (from Froude, 2011, modified. ¹Glastonbury and Fell (2002); ²Glastonbury and Fell (2000) (continued on next page)

	ID	Name	Reference	Location	Failure year	General geology (material)	Natural or Man-made slope	Vegetated	Type of monitoring	TERTIARY PHASE Duration [TC] (days)
DIGITIZED TIME SERIES OF DISPLACEMENT	1	Bohemia	Zvelebil and Moser, 2001	Czech Republic	1984	Rock (sandstone)	Natural	Yes	Dilatometer	20
	2	Braced up	Bhandari, 1988	USA	1941	Sandstone	Natural	No	-	138
	3	Coal mine	Hungr and Kent, 1995	Canada	-	Soft Rocks (sandstones, siltstone and shale)	Man-made	No	-	<1
	4	Chamousset	Got et al, 2010	France	2007	Eroded Rock	Man-made	Yes	Extensometers Seismic surveys	20
	5	Dosan line	Saito, 1965	Japan	1962	Rock (Basalt and limestone)	Natural	No	-	11
	6	Hrensko	Zvelebil, 1984	Czech Republic	1984	Sandstone	Man-made	Yes	Dilatometer	13
	7	Monte Beni	Gigli et al, 2011	Italy	2002	Rocks (Basalt and ophiolite)	Natural	Yes	Distometers, TInSAR	60
	8	Ooigawa railroad	Saito, 1965	Japan	1960	-	Natural	-	-	24
	9	Ruahihi	Salt, 1988	New Zealand	-	Rock	Natural	No	-	11
	10	Takabayama	Saito, 1979	Japan	1970	Rock	Natural	-	Extensometer	41
	11	Tessina	Petley et al, 2005	Italy	2003	Rock	Natural	No	Inclinometers, Extensometer	778
	12	Val Pola	Borsetto et al, 1991	Italy	1988	Rock	Natural	Yes	Inclinometers, Extensometer	33
	13	Roesgrenda - Slide A	Okamoto et al, 2004	Norway	2000	Rock	Natural	No	Extensometers	12
	14	Liberty pit mine	Rose and Hungr, 2007	USA	-	Soft Rock	Natural	No	-	25
DATABASE FROM FROUDE (2011)	15	Chuquicamata	Kennedy and Niermeyer, 1970 ¹	Chile	-	Rock	Man-made	No	Surface survey	109
	16	Selbourne Slope Cutting	Petley et al., 2002	England	1989	Soil	Man-made	No	Inclinometer	150
	17	Vajont	Kilburn and Petley, 2003	Italy	1963	Rock	Natural	Yes	Surface monument	63
	18	Bomba	Picarelli et al., 2005	Italy	-	Soil	Man-made	No	-	8,43
	19	Xintan	Keqiang and Sijing, 2006	China	1985	Rock	Man-made	Yes	Survey lines	357,91
	20	New tredegar	Carey et al., 2007	Wales	1930	Rock	Man-made	No	Peg Network	15,43
	21	Barrick Gold's Betze-Post open mine	Rose and Hungr, 2007	USA	2001	Rock	Man-made	No	Inclinometer	43,54

	ID	Name	Reference	Location	Failure year	General Geology (material)	Natural or Man-made slope	Vegetated	Type of monitoring	TERTIARY PHASE Duration [TC] (days)
DATABASE FROM FROUDE (2011)	22	Un-named slope	Rose and Hungr, 2007	USA	-	Rock	Man-made	No	Extensometer	8,23
	23	Ota Mura	Petley and Rosser, 2006	Japan	2004	Rock	Man-made	Yes	Extensometer	7,99
	24	Lijiaxia Landslide	Bai <i>et al.</i> , 2008	China	1998	Rock	Man-made	Yes	Surface monument	14,25
	25	Saleshan landslide	Siqing and Sijing, 2000	China	1986	Rock	Natural	No	-	144,5
	26	Eskihisar coal mine wall	Ulusay and Aksoy, 1994	Turkey	1989	Rock	Man-made	No	Tension crack meters	434
	27	Randa rockslide	Bonnard <i>et al.</i> , 1995	Switzerland	1991	Rock	Natural	Yes	Surface survey	10
	28	Asamushi landslide	Saito, 1969	Japan	1966	Rock	Natural	Yes	Surface survey	1,36
	29	Un-named rockmass	Mufundirwa <i>et al.</i> , 2010	Japan	-	Rock	Man-made	No	Extensometer	0,016
	30	Excavation A	Glanstonbury and Fell 2002	Australia	1950	Rock	Man-made	No	Surface survey	13,63
	31	Teifer Mine	Thompson and Cierlitz, 1993 ¹	Australia	1992	Rock	Man-made	No	Surface survey	144,65
	32	Tuckabianna West	Thompson and Cierlitz 1993 ¹	Australia	-	Rock	Man-made	No	Surface survey	46,21
	33	Smoky River Mine	Martin, 1993 ¹	Canada	-	Rock	Man-made	No	Surface survey	84,68
	34	Delabole Quarry	Boyd <i>et al.</i> , 1973 ¹	England	-	Rock	Man-made	No	Tension crack meters	3171,45
	35	Afton Mine	Reid and Stewart, 1986 ¹	Canada	1986	Rock	Man-made	No	Surface survey	9,82
	36	Hogarth Pit	Brawner and Stacey, 1979 ¹	Canada	1975	Rock	Man-made	No	Extensometer	243,28
	37	Luscar Mine-50A2 Pit	Wylie and Munn, 1978 ¹	Canada	-	Rock	Man-made	No	Extensometer	338,71
	38	Roberts Pit	Coates <i>et al.</i> , 1979 ¹	Canada	-	Rock	Man-made	No	Surface survey	126,17
	39	Nevis Bluff	Brown <i>et al.</i> , 1980 ²	New Zeland	1975	Rock	Natural	No	Surface survey	26,76
	40	Ryan and Call slide 2	Ryan and Call, 1992 ¹	Mexico	-	Rock	Man-made	No	Surface survey	65,14
	41	Kennecott#1	Zavodni & Broadbent, 1980 ¹	USA	-	Rock	Man-made	No	Tension crack meters	24,97
42	Labe Canyon	Zvelebil and Moser, 2001	Germany	1984	Rock	Natural	Yes	Rod dilatometer	102,03	

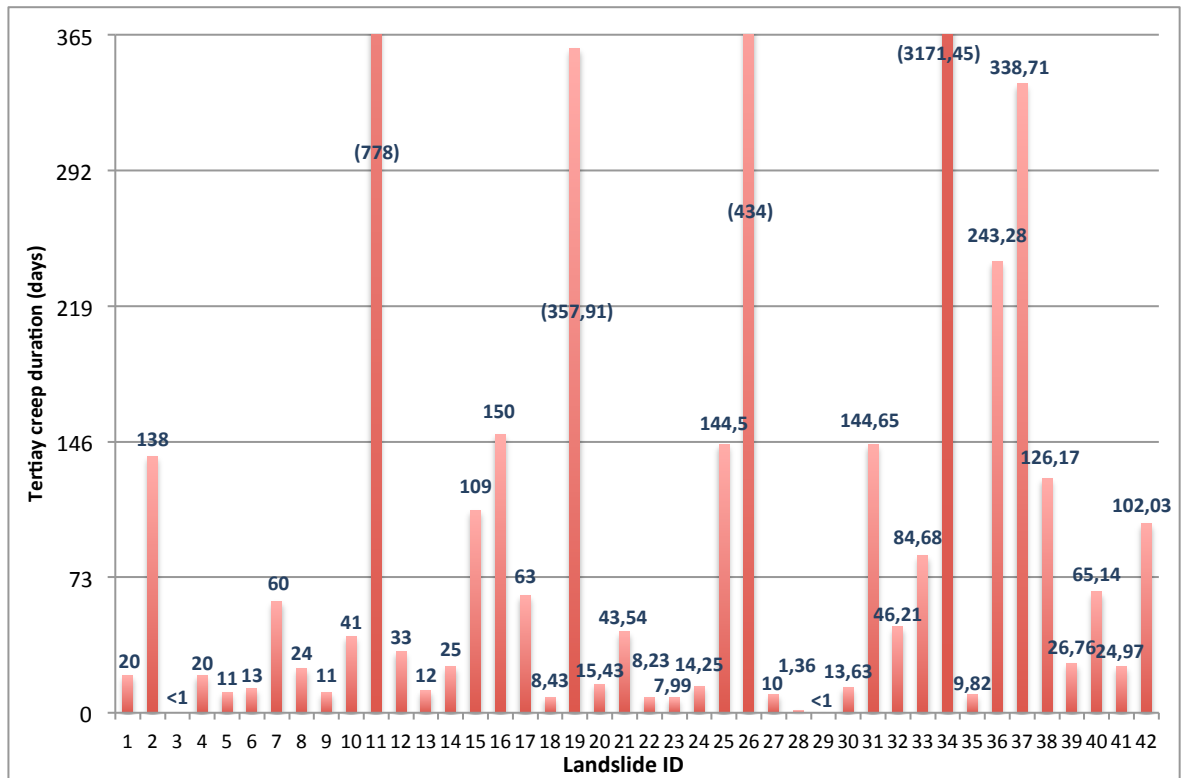


Figure 6.4 Tertiary creep duration before failure for database of monitored landslides from literature.

6.3.1. Investigation of landslide tertiary creep using A-DInSAR: a theoretical approach

The tertiary creep phase is by definition represented by the acceleration of the displacement trend. However, the secondary creep stage is very often characterised by low displacement velocity and thus not detectable by satellites. Under this condition, the TC could be observed by satellite as the beginning of a phase characterised by displacement. Beginning with this consideration, let us consider the most favourable condition for all cases: namely, when the tertiary creep begins immediately before the acquisition of a SAR image. The following are the possible cases:

a) $TC/RT \leq 1$ (1 image during TC)

If TC is shorter than or equal to RT, we will have available only the image acquired immediately after the beginning of TC (as in the hypothesis). The TC will be described by only one sample before the failure. Even in a strictly theoretical

discussion such as this one, we must consider that having only one image with information about displacement is not robust enough to define new deformation behaviour, least of all, to define when the TC started. In this case, we will not be able to make any prediction about the time of failure or to define if the instability process is starting/increasing.

b) $1 < TC/RT \leq 2$ (2 images during TC)

This scenario represents the minimum conditions that allow 2 displacement data points within the tertiary creep. From the above considerations, in these circumstances, we could assess that a new displacement trend had begun, but the data still are not sufficient to define an increment function, which is a necessary condition for applying the semi-empirical model to predict the slope time of failure.

c) $TC/RT > 2$ (3 or more images during TC)

This scenario represents the minimum conditions to obtain 3 or more data points regarding the tertiary stage. From this condition, we are able to build a function that can provide information on increasing displacement velocity, and thus, we are able to apply semi-empirical models.

Considering the revisit time of past, present and future SAR satellites and the tertiary creep duration of the landslides shown in the database (Tab. 6.1), we present here several theoretical monitoring scenarios based on the considerations described above (Tab. 6.2). Three different colours depict every TC/RT class: red for the scenario described in (a) (only one image during TC), yellow for (b) (2 images during TC) and green for (c) (3 or more images during TC). Although we cannot take any action in the first scenario, in the second, it is possible to recognise the beginning of the displacement/acceleration (such information could be used to hypothesise a phase of attention/warning). Finally, in the third case, we can begin to apply the semi-empirical models to predict the landslide time of failure. Obviously, the greater the number of data points preceding the failure event, the greater will be the chances of success of the prediction analyses (Mazzanti *et al.*, 2014).

Based on the analysis of the landslide database (Tab. 6.2), if these processes had occurred since 1992, only 3 of the 42 landslides would not be monitored due to the too rapid evolution of the tertiary creep.

		PAST SATELLITES			PRESENT SATELLITES					FUTURE SATELLITES						
		ALOS PALSAR	J-ERS	ERS/Envisat	RADARSAT-1/2	COSMO-SkyMed (4 sat.)				Terra SAR-X	Sentinel-1	RADARSAT Constellation Mission	ALOS PALSAR-2	SAOCOM (2 Sat)		
		REVISIT TIME (DAYS)														
ID	Name	46	44	35	24	4	8	16	11	6	12	3	12	14	8	16
1	Bohemia	0,43	0,45	0,57	0,83	5,00	2,50	1,25	1,82	3,33	1,67	6,67	1,67	1,43	2,50	1,25
2	Braced up	3,00	3,14	3,94	5,75	34,50	17,25	8,63	12,55	23,00	11,50	46,00	11,50	9,86	17,25	8,63
3	Coal mine	0,00	0,01	0,01	0,01	0,06	0,03	0,01	0,02	0,04	0,02	0,07	0,02	0,02	0,03	0,01
4	Chamousset	0,43	0,45	0,57	0,83	5,00	2,50	1,25	1,82	3,33	1,67	6,67	1,67	1,43	2,50	1,25
5	Dosan line	0,24	0,25	0,31	0,46	2,75	1,38	0,69	1,00	1,83	0,92	3,67	0,92	0,79	1,38	0,69
6	Hrensko	0,28	0,30	0,37	0,54	3,25	1,63	0,81	1,18	2,17	1,08	4,33	1,08	0,93	1,63	0,81
7	Monte Beni	1,30	1,36	1,71	2,50	15,00	7,50	3,75	5,45	10,00	5,00	20,00	5,00	4,29	7,50	3,75
8	Ooigawa railroad	0,52	0,55	0,69	1,00	6,00	3,00	1,50	2,18	4,00	2,00	8,00	2,00	1,71	3,00	1,50
9	Ruahihi	0,24	0,25	0,31	0,46	2,75	1,38	0,69	1,00	1,83	0,92	3,67	0,92	0,79	1,38	0,69
10	Takabayama	0,89	0,93	1,17	1,71	10,25	5,13	2,56	3,73	6,83	3,42	13,67	3,42	2,93	5,13	2,56
11	Tessina	16,91	17,68	22,23	32,42	194,5	97,25	48,63	70,73	129,7	64,83	259,3	64,83	55,57	97,25	48,63
12	Val Pola	0,72	0,75	0,94	1,38	8,25	4,13	2,06	3,00	5,50	2,75	11,00	2,75	2,36	4,13	2,06
13	Roesgrenda	0,26	0,27	0,34	0,50	3,00	1,50	0,75	1,09	2,00	1,00	4,00	1,00	0,86	1,50	0,75
14	Liberty pit mine	0,54	0,57	0,71	1,04	6,25	3,13	1,56	2,27	4,17	2,08	8,33	2,08	1,79	3,13	1,56
15	Chuquicamata	2,37	2,48	3,11	4,54	27,25	13,63	6,81	9,91	18,17	9,08	36,33	9,08	7,79	13,63	6,81
16	Selbourne	3,26	3,41	4,29	6,25	37,50	18,75	9,38	13,64	25,00	12,50	50,00	12,50	10,71	18,75	9,38
17	Vajont	1,37	1,43	1,80	2,63	15,75	7,88	3,94	5,73	10,50	5,25	21,00	5,25	4,50	7,88	3,94
18	Bomba	0,18	0,19	0,24	0,35	2,11	1,05	0,53	0,77	1,41	0,70	2,81	0,70	0,60	1,05	0,53
19	Xintan	7,78	8,13	10,23	14,91	89,48	44,74	22,37	32,54	59,65	29,83	119,3	29,83	25,57	44,74	22,37
20	New tredegar	0,34	0,35	0,44	0,64	3,86	1,93	0,96	1,40	2,57	1,29	5,14	1,29	1,10	1,93	0,96
21	Barrick Gold's mine	0,95	0,99	1,24	1,81	10,89	5,44	2,72	3,96	7,26	3,63	14,51	3,63	3,11	5,44	2,72
22	Un-named slope	0,18	0,19	0,24	0,34	2,06	1,03	0,51	0,75	1,37	0,69	2,74	0,69	0,59	1,03	0,51
23	Ota Mura	0,17	0,18	0,23	0,33	2,00	1,00	0,50	0,73	1,33	0,67	2,66	0,67	0,57	1,00	0,50
24	Lijaxia Landslide	0,31	0,32	0,41	0,59	3,56	1,78	0,89	1,30	2,38	1,19	4,75	1,19	1,02	1,78	0,89
25	Saleshan landslide	3,14	3,28	4,13	6,02	36,13	18,06	9,03	13,14	24,08	12,04	48,17	12,04	10,32	18,06	9,03
26	Eskihisar coal mine	9,43	9,86	12,40	18,08	108,5	54,25	27,13	39,45	72,33	36,17	144,7	36,17	31,00	54,25	27,13
27	Randa rockslide	0,22	0,23	0,29	0,42	2,50	1,25	0,63	0,91	1,67	0,83	3,33	0,83	0,71	1,25	0,63
28	Asamushi	0,03	0,03	0,04	0,06	0,34	0,17	0,09	0,12	0,23	0,11	0,45	0,11	0,10	0,17	0,09
29	UN rockmass	0,00	0,00	0,00	0,00	0,00	0,00	0,00	0,00	0,00	0,00	0,01	0,00	0,00	0,00	0,00
30	Excavation A	0,30	0,31	0,39	0,57	3,41	1,70	0,85	1,24	2,27	1,14	4,54	1,14	0,97	1,70	0,85
31	Teifer Mine	3,14	3,29	4,13	6,03	36,16	18,08	9,04	13,15	24,11	12,05	48,22	12,05	10,33	18,08	9,04
32	Tuckabianna West	1,00	1,05	1,32	1,93	11,55	5,78	2,89	4,20	7,70	3,85	15,40	3,85	3,30	5,78	2,89
33	Smoky River Mine	1,84	1,92	2,42	3,53	21,17	10,59	5,29	7,70	14,11	7,06	28,23	7,06	6,05	10,59	5,29
34	Delabole Quarry	68,94	72,08	90,61	132	793	396	198	288	529	264	1057	264	227	396	198
35	Afton Mine	0,21	0,22	0,28	0,41	2,46	1,23	0,61	0,89	1,64	0,82	3,27	0,82	0,70	1,23	0,61
36	Hogarth Pit	5,29	5,53	6,95	10,14	60,82	30,41	15,21	22,12	40,55	20,27	81,09	20,27	17,38	30,41	15,21
37	Luscar Mine Pit	7,36	7,70	9,68	14,11	84,68	42,34	21,17	30,79	56,45	28,23	112,9	28,23	24,19	42,34	21,17
38	Roberts Pit	2,74	2,87	3,60	5,26	31,54	15,77	7,89	11,47	21,03	10,51	42,06	10,51	9,01	15,77	7,89
39	Nevis Bluff	0,58	0,61	0,76	1,12	6,69	3,35	1,67	2,43	4,46	2,23	8,92	2,23	1,91	3,35	1,67
40	Ryan & Call slide 2	1,42	1,48	1,86	2,71	16,29	8,14	4,07	5,92	10,86	5,43	21,71	5,43	4,65	8,14	4,07
41	Kennecott#1	0,54	0,57	0,71	1,04	6,24	3,12	1,56	2,27	4,16	2,08	8,32	2,08	1,78	3,12	1,56
42	Labe Canyon	2,22	2,32	2,92	4,25	25,51	12,75	6,38	9,28	17,01	8,50	34,01	8,50	7,29	12,75	6,38

TERTIARY CREEP/REVIST TIME

Tab. 6.2 TC/RT ratio values of landslides database considering past, present and future SAR satellites. We present in red the cases where there is only one image during the TC, in yellow cases with two images and in green cases with 3 or more images. For more information, refer to paragraph 6.3.1.

Furthermore, the significant improvement in terms of revisit time, provided by present and future satellites, greatly increases the ability to monitor such processes. In this regard, it should be observed that 17 landslides that could not be monitored by past satellites (namely, ERS 1/2, Envisat, J-ERS and ALOS PALSAR) would be monitored by present and future satellites. Moreover, for 8 landslides, the past satellites could theoretically observe their TC (even with only two images), but they become potentially predictable if monitored by recent satellites (e.g., the Takabayama and Vajont landslides).

6.3.2. Investigation of landslide tertiary creep using A-DInSAR: a practical approach.

The discussion in paragraph 6.3.1 addresses a key question: Does the A-DInSAR technique possess the basic features for landslide forecasting? The ability to observe the TC as a function of the revisit time of the satellite is a necessary but not sufficient condition for this purpose. In our discussion, we have deliberately neglected another aspect of crucial importance, namely the displacement rate that occurs during the tertiary creep stage. The TC is not characterised only by duration but also by increasing deformation, which is a function of multiple factors that are very difficult to predict. For this reason, we must also consider the quantity of displacement to be measured during the TC, especially considering that the displacement increases as the slope approaches failure. In this regard, it is also important to remember the limitations of phase ambiguity mentioned in section 6.1 and the possible ways to overcome them.

In addition to such points, also other practical considerations need to be mentioned:

- i. Because SAR satellites can have difficulty during their operational missions, some planned images may not to be acquired, and thus, the real revisit time can be longer than the nominal one. Moreover, even when the average revisit time is similar to the nominal one for a given stack, there is still a possibility of the absence of data in circumscribed periods for specific, time-limited satellite troubles.
- ii. Even with relatively slow displacement during the TC (at least during the initial stage), some problems related to temporal unwrapping errors may occur, thus affecting the measured deformation processes. In these cases, manual analyses of displacement time series may prevent the underestimation of the observed displacements (see section 6.2).

- iii. Good radar targets are also necessary for performing an A-DInSAR investigation over a given landslide. This could seem trivial, but the presence of vegetation or the total absence of structures can also prevent the attainment of good results for case studies that are "perfect" from a kinematic point of view.
- iv. Finally, the issue of the satellite LOS related to the real displacement direction is another key point of consideration. All displacement values considered in the creep curves are "*real displacement*", whereas A-DInSAR provides information along the LOS. This has several consequences for landslide investigation because only a portion of the real movement can be detected. Landslides affecting North-South oriented slopes, for example, are not observed properly (the horizontal component is not detected at all). For East- or West-facing slopes, the possibility also exists to observe only fractions of the true movements for reasons related to the inclination of the slope. This is usually considered an inconvenient condition, but it can also be an advantage, as it reduces the risk of reaching the observable velocity limit due to too rapid movements. However, both in negative and positive cases, this aspect should be considered.

All of these aspects have been properly addressed in the case studies herein presented. In particular, for the case study discussed in Chapter 4, the parameters capable of influencing the A-DInSAR results (both in terms of the SAR technical features and the characteristics of the landslides) have been quantitatively evaluated for the best analysis design, in terms of data selection and processing methods.

To conclude, each of the above listed aspects needs a case-by-case evaluation due to the complexity of the factors that influence the feasibility of landslide analyses using A-DInSAR, in terms of both the investigation of historical displacements and future monitoring.

In particular, for the future-oriented monitoring of a landslide, all of the limitations that should be considered case-by-case can be duly managed by a proper design of the image acquisition plan (the selection of the incidence angle, the choice of the orbital geometry, and the ad-hoc revisit time) and implementation on the ground (for example, with the installation of corner reflectors in areas without adequate scatterers).

7. CONCLUSIONS

The work presented in this PhD thesis has shown that the potentials in the framework of ground deformation investigation are today very sophisticated thanks to modern technologies.

Compared with many decades ago, when R. Peck theorised the importance of the observational method (DiBiagio & Flaate, 2000), today, the confidence in this approach is further supported by a variety of methodologies. These tools allow the measurement of displacements with very high accuracies, and this allows (also in the future perspective) the quantitative measurement of processes as a key parameter for understanding, monitoring and forecasting. This opinion needs to be clearly stated because it is not always agreed upon: "monitoring" is often still considered as a sort of safeguard to be applied only for control purposes.

With this consideration, satellite SAR interferometry using data collected almost regularly since 1992 is an excellent opportunity to perform historical analyses. All of this is possible because the paradigm of monitoring as "activities that begin after the installation of site-specific instrumentation" has been completely changed beyond the limits previously imagined.

In this thesis, we assessed that satellite SAR interferometry is able to provide quantitative information, which could be more or less refined; moreover, although the degree of reliability is a function of many factors (instrumental, technical, methodological, environmental and related to the process), the level of knowledge that it contributes to the comprehension of the observed processes is however of great value because it is unique and not replaceable with other techniques and methodologies.

The results obtained in the case studies discussed to support this thesis show that the dependence on surrounding factors is extremely high, especially for site-specific conditions. In this regard, the variety of case studies presented (a coastal cliff completely devoid of vegetation in Oman, a densely vegetated, hilly area with sparse structures in the Abruzzi Region (Italy), and finally, a flat area affected by urbanisation and quarry activities) has allowed for the understanding of how the technique provides very useful information and that it is necessary to perform a careful analysis design calibrated to the type of area, the specific issue, the final purpose and the available data. All interferometry-

based techniques, however, are today considered opportunistic (Hanssen, 2005). This is certainly true in the sense that it is necessary to take advantage of what is available in terms of acquired images. On the one hand, this perspective has led to the need to develop increasingly sophisticated algorithms for data analysis, but on the other hand, it has most likely slowed the process of adaptation of such techniques to specific cases studies. This approach could improve the level of results by evaluating the specific needs to be considered case by case. In this thesis, it is shown how the effectiveness of the technique (despite its intrinsic limits) can be increased through conscious use and case-by-case adaptations. In this regard, the case studies addressed represent good examples because they are very different from one another:

- In the case study of the coastal slope in Oman, it was not possible to apply the A-DInSAR techniques in a standard way, and only by using an ad hoc procedure based on the DInSAR methods on the L-band archive data could valid results be obtained (Chapter 3);
- The case study in the Abruzzi Region (Italy) has shown that the correct interpretation of the processes was possible only by the proper integration of the double orbital geometric InSAR results, thus avoiding misunderstandings of the real kinematics of some slope instability processes. This objective was achieved only using specific evaluations of all of the parameters involved in the issue (both related to the SAR technical characteristics and also to the local topography and processes under investigation) (Chapter 4);
- The subsidence induced by the quarrying activities in the Tivoli-Guidonia area (Acque Albule Basin, nearby Rome) has been fully understood only using the integration of the A-DInSAR results with the geological/hydrogeological data. Furthermore, only using manual and model-independent A-DInSAR methods was it possible to reconstruct the time series of displacement to show the triggering of these processes in previously undisturbed areas (Chapter 5);

Therefore, we can say that satellite SAR interferometry in the fields of Earth Sciences and Engineering Geology, in particular, can be used with a dual purpose: a general "survey" method, which is more common today, and a more case-specific approach. The latter is certainly more time-consuming and less objective; furthermore, it requires expertise in both data processing and the issues under investigation to optimise the specific

applications to single processes. Based on these observations, many efforts have been made in recent years to increase the applicability of the technique over large areas by reducing the technological limitations, such as the difficulty of obtaining reliable results in areas without good reflectors (see SqueeSAR technique, Ferretti *et al.*, 2011; QPS technique, Perissin & Wang, 2012).

In addition to the purely technical issues of signal-processing, considered the core of the discipline, progress has been made by the space agencies that are heavily investing in providing ever more numerous and qualitatively valuable satellite SAR data. Even private industry is increasingly involved. Finally, we can say that this remote sensing sector is definitely expanding, in terms of both opportunity and the availability of data. In accordance with the above, therefore, the promising future of satellite interferometry is an opportunity to be fully exploited, and appropriate actions should be taken to optimise future acquisitions; for example, by increasing the installation of artificial reflectors in areas that are difficult to be monitored, also in future perspective and not necessarily for planned monitoring activities (e.g., for areas where urban expansion or future large infrastructure work is expected, or even for areas where extraction activities may begin in the future). In addition, it is clear that the satellite SAR systems have been transformed over time by general Earth Observation systems into real tools for the monitoring of ground/structure deformation through the development of the A-DInSAR methods. This purpose for the SAR data, therefore, will always be a priority for the authorities responsible for the management of satellites, as in the Italian Space Agency with the COSMO-SkyMed constellation.

In this PhD thesis, the applications tested in several case studies (landslides and a Quaternary plain affected by subsidence) have clearly shown that the investigation of the processes of subsidence is certainly simpler because of the smoother spatial distribution of deformation, the topographic characteristics, and the slower evolution compared with most slope instability processes. The results obtained for the Tivoli-Guidonia case study (see 6.2), for example, demonstrate how the high detail reached in the definition of the process (also through the validation by data of a different nature) would allow the application of predictive models.

The A-DInSAR methodology, however, should still be considered borderline from a failure prediction perspective for landslide processes. Considering this objective, we

observed that the revisit time certainly represents a fundamental problem. The improvements in the technical characteristics of the sensors have been remarkable in recent years (e.g., the increase in the spatial resolution), but to date, equally interesting improvements of the revisit time for future satellites are not expected, although the trend shows general improvement. Chapter 6 shows how, from a theoretical point of view, the ability to monitor landslide processes can be very high using current and future satellites; however, in consideration of the magnitude of deformations involved and the environmental difficulties affecting landslides areas, the outlook still remains only a possibility. The increase in the temporal resolution offered by future satellites will certainly allow a refinement in the ability to describe the evolution of slow deformation processes, but it is not possible to imagine a drastic increase in the predictive capabilities for more rapid processes basing on the expected revisit time of future satellites.

Moreover, another aspect to consider is related to the time interval between the acquisition of the images and the interpretation of a useful result for a real "monitoring" activity. This time gap must cover the transfer of data from the satellite to the ground, the validation of the raw data, the transmission from the space agency to the A-DInSAR operators, the processing time of the data, the validation of the data and the interpretation of the results. Under the best conditions (totally theoretical), this could require several hours. For a monitoring activity with a "control" purpose, this is acceptable. However, another aspect to be considered is related to the need to acquire an entire data-stack to begin an A-DInSAR analysis. If no images for a given area are available, the time necessary for the acquisition of a proper images-stack must be considered. From this perspective, an acquisition policy devoted to systematic coverage to allow interferometric processing is extremely valuable.

Tab. 6.2 shows that only some of the landslides in the database would have been monitored (from a strictly theoretical point of view). Considering that the database is related to past large landslides, this limitation is even more true for small-scale processes. Considering small landslides that develop and reach failure in a very short time (a few days to a few hours) (Bozzano *et al.*, 2014; Mazzanti *et al.*, 2014), it is clear that this technique would not be used, and it almost certainly never will be. Finally, all of this discussion neglects the limitations related to the complexity of observing these processes by satellites in areas with difficult conditions (e.g., absence of measurement points for vegetation and problems related to the presence of radar geometric distortions).

To conclude, the contribution of using satellite InSAR techniques to investigate ground deformation issues, such as subsidence and slow landslides, can be crucial. The predictive prospects for the issues of slope instability are limited, but some improvements are possible using future data, with higher spatial and temporal resolutions. In this regard, however, integration with other techniques (based on the same principle as the terrestrial SAR interferometry) can be an effective way to fill the temporal gap that would be otherwise insurmountable.

References

- Akbarimehr, M., Motagh, M., & Haghshenas-Haghighi, M. (2013). Slope stability assessment of the sarcheshmeh landslide, Northeast Iran, investigated using InSAR and GPS observations. *Remote Sensing*, 5(8), 3681-3700.
- Alexander, D. E. (1993). *Natural disasters*. Springer.
- Amelung, F., Galloway, D. L., Bell, J. W., Zebker, H. A., & Lacznik, R. J. (1999). Sensing the ups and downs of Las Vegas: InSAR reveals structural control of land subsidence and aquifer-system deformation. *Geology*, 27(6), 483-486.
- Arattano, M. & Marchi, (2008). L. Systems and sensors for debris-flow monitoring and warning. *Sensors*, 8, 2436–2452. 19.
- Ayalew, L., & Yamagishi, H. (2005). The application of GIS-based logistic regression for landslide susceptibility mapping in the Kakuda-Yahiko Mountains, Central Japan. *Geomorphology*, 65(1), 15-31.
- Bai, J.G., Lu, S.D. & Han, J.S. (2008). Importance of study of creep sliding mechanism to prevention and treatment of reservoir landslide. In: Z. Chen, J. Zhang, Z. Li, F. Wu and K. Ho (Editors), *Landslides and Engineered Slopes: From the Past to the Future*. CRC Press: Taylor & Francis Group, Xi'an, China, pp. 1071 - 1076.
- Bhandari, R.K. (1988). Special lecture - some practical lessons in the investigation and field monitoring of landslides *Landslides*, Vols 1 - 3, 1435 - 1457
- Barrett, E. C. (2013). *Introduction to environmental remote sensing*. Routledge.
- Béchenec, F., Le Métour, J., Platel, J.P. & Roger, J. (1993). Geological map of the Sultanate of Oman, scale 1:1,000,000, Oman Ministry of Petroleum and Minerals, Directorate General of Minerals.
- Bell, R., & Glade, T. (2004). Quantitative risk analysis for landslides—Examples from Bildudalur, NW-Iceland. *Natural Hazards and Earth System Science*, 4(1), 117-131.
- Berardino, P., Fornaro, G., Lanari, R., & Sansosti, E. (2002). A new algorithm for surface deformation monitoring based on small baseline differential SAR interferograms. *IEEE Trans. Geosci. Remote Sensing*. 40, 2375 – 2383.
- Bigi, S., Calamita F., Cello G., Centamore E., Deiana G., Paltrinieri W., & Ridolfi M. (1995). Evoluzione messinianopliocenica del sistema catena avanfossa dell'area marchigiano-abruzzese esterna. *Studi Geologici Camerti vol. spec. 1995/1*, pp171-183. Camerino (in Italian).
- Bigi, S., Centamore E. & Nisio S. (1997) Elementi di tettonica quaternaria nell'area pedeappenninica marchigiano-abruzzese. *Il Quaternario*, 10(2), 359-362.
- Billi, A., Valle, A., Brillì, M., Faccenna, C., & Funicello, R. (2007). Fracture-controlled fluid circulation and dissolutional weathering in sinkhole-prone carbonate rocks from central Italy. *Journal of structural geology*, 29(3), 385-395.
- Blong, R. J. (1996). Volcanic hazards risk assessment. In *Monitoring and mitigation of volcano hazards* (pp. 675-698). Springer Berlin Heidelberg.
- Bock, Y., Wdowinski, S., Ferretti, A., Novali, F., & Fumagalli, A. (2012). Recent subsidence of the Venice Lagoon from continuous GPS and interferometric synthetic aperture radar. *Geochemistry, Geophysics, Geosystems*, 13(3).
- Boni, C., Bono, P. & Capelli, G. (1986). Schema idrogeologico dell'Italia Centrale. *Mem. Soc. Geol. It.*, 35, pp. 991-1012.
- Bonnard, C., Noverraz, F., Lateltin, O., & Raetzo, H. (1995). Large Landslides and Possibilities of Sudden Reactivation. *Felsbau*, 13(6): 400 - 407.

- Bono, P. (2005). Indagini idrogeologiche per determinare le cause dei dissesti agli edifici di via Cesare Augusto e aree limitrofe, in località Bagni di Tivoli. Dip. Scienze della Terra (Università La Sapienza, Roma) – Regione Lazio.
- Borsetto, M., Frassoni, A., La Barbera, G., Fanelli, M., Giuseppetti, G. & Mazzà, G. (1991). An application of Voight empirical model for the prediction of soil and rock instabilities. *Landslides*, Bell (ed). 1991. Balkema, Rotterdam. ISBN 90 5410 032 X.
- Bovenga, F., Refice, A., Nutricato, R., Guerriero, L., & Chiaradia, M. T. (2004). SPINUA: a flexible processing chain for ERS/ENVISAT long term interferometry. In *Proceedings of ESA-ENVISAT Symposium, Salzburg, Austria* (pp. 6-10).
- Boyd, J.M., Hinds, D.V., Moy, D. & Rogers, C. (1973). Two simple devices for monitoring movements in rock slopes. *Quarterly Journal of Engineering Geology and Hydrogeology*, 6(3 - 4): 295 - 302.
- Bozzano, F., Mazzanti, P., Prestininzi, A., & Mugnozza, G. (2010). Research and development of advanced technologies for landslide hazard analysis in Italy. *Landslides*, 7(3), 381–385. doi:10.1007/s10346-010-0208-x
- Bozzano, F., Cipriani, I., Mazzanti, P. & Prestininzi, A. (2011). Displacement patterns of a landslide affected by human activities: Insights from ground-based InSAR monitoring. *Nat. Hazards* 2011, 59, 1377–1396. 27.
- Bozzano, F., Cipriani, I., & Mazzanti, P. (2012). Assessing the efficacy of semi-empirical failure prediction methods for slope affected by human activities. *Landslides and Engineered Slopes: Protecting Society through Improved Understanding*, edited by: Eberhardt, E., Froese, C., Turner, K., and Leroueil, S., Taylor & Francis Group, London, 1465-1471.
- Bozzano, F., & Rocca, A. (2012). Remote monitoring of deformation using Satellite SAR Interferometry. *Geotechnical News*, 30(2), 26.
- Bozzano, F., Cipriani, I., Mazzanti, P., & Prestininzi, A. (2014). A field experiment for calibrating landslide time-of-failure prediction functions. *International Journal of Rock Mechanics and Mining Sciences*, 67, 69–77. doi:10.1016/j.ijrmms.2013.12.006
- Brawner, C.O. and Stacey, P.F. (1979). Hogarth pit slope failure, Ontario, Canada. In: B. Voight (Editor), *Rockslides and Avalanches*. Elsevier, Amsterdam, pp. 691 - 707.
- Brown, I., Hittinger, M. & Goodman, R. (1980). Finite element study of the Nevis Bluff (New Zealand) rock slope failure. *Rock Mechanics*, 12: pp. 231 - 245.
- Bru, G., Herrera, G., Tomás, R., Duro, J., De la Vega, R., & Mulas, J. (2013). Control of deformation of buildings affected by subsidence using persistent scatterer interferometry. *Structure and infrastructure engineering*, 9(2), 188-200.
- Brunetti, E. (2010). Modeling the Impact of the Dewatering in the Travertine Aquifer of the Acque Albule Basin (Tivoli, Italy). Master of Science in Earth Sciences, Waterloo, Ontario, Canada.
- Brunetti, E., Jones, J. P., Petitta, M., & Rudolph, D. L. (2013). Assessing the impact of large-scale dewatering on fault-controlled aquifer systems: a case study in the Acque Albule basin (Tivoli, central Italy). *Hydrogeology Journal*, 21(2), 401-423.
- Buccolini, M., Crescenti, U. & Sciarra, N. (1994) – Interazione fra dinamica dei versanti ed ambienti costruiti: alcuni esempi in Abruzzo. *Il Quaternario*, 7(1), 179-196.
- Budhu, M., & Adiyaman, I. B. (2010). Mechanics of land subsidence due to groundwater pumping. *International Journal for Numerical and Analytical Methods in Geomechanics*, 34(14), 1459-1478.
- Burbey, T. (2002). The influence of faults in basin-fill deposits on land subsidence, Las Vegas Valley, Nevada, USA. *Hydrogeology Journal*, 10(5), 525–538, <http://dx.doi.org/10.1007/s10040-002-0215-7>.
- Bürgmann, R., Rosen, P. A., & Fielding, E. J. (2000). Synthetic aperture radar interferometry to measure Earth's surface topography and its deformation. *Annual Review of Earth and Planetary Sciences*, 28(1), 169-209.

- Cabral-Cano, E., Dixon, T. H., Miralles-Wilhelm, F., Díaz-Molina, O., Sánchez-Zamora, O., & Carande, R. E. (2008). Space geodetic imaging of rapid ground subsidence in Mexico City. *Geological Society of America Bulletin*, 120(11-12), 1556-1566.
- Calamita, F., Scisciani, V., Montefalcone, R., Paltrinieri, W. & Pizzi, A. (2002) – L’ereditarietà del paleomargine dell’Adria nella geometria del sistema orogenico centro-appenninico: l’area abruzzese esterna. *Memorie della Società Geologica Italiana*, 57, 355-368.
- Cantalamessa, G., Centamore, E., Chiocchini, U., Colalongo, M.L., Micarelli, A., Nanni, T., Pasini G., Potetti, M. & Ricci Lucchi, F. (1986) – Il Plio-Pleistocene delle Marche. *Studi Geologici Camerti*, vol. speciale “La Geologia delle Marche”, 73° Congresso della Società Geologica Italiana, 61-81.
- Canuti, P. and Focardi, P. (1986). Slope stability and landslides investigation in Tuscany. *Mem. Sot. Geol. Ital.*, 3 I: 307-315.
- Capelli, G., Cosentino, D., Messina, P., Raffi, R., & Ventura, G. (1987). Modalità di ricarica e assetto strutturale dell’acquifero delle sorgenti Capore–S. Angelo (Monti Lucretili–Sabina Meridionale) (Recharge and structural setting of the Capore-S. Angelo springs’ reservoir–Lucretili Mt. s-South Sabina). *Geologica Romana*, 26, 419-447.
- Capelli, G., Mazza, R. & Gazzetti, C. (2005a). Strumenti e strategie per la tutela e l’uso compatibile della risorsa idrica nel Lazio. *Gli acquiferi vulcanici. Quaderni di Tecniche di Protezione Ambientale*, 78.
- Capelli, G., Mazza, R. & Taviani, S. (2005b). Studi idrogeologici per la definizione degli strumenti operativi del piano stralcio per l’uso compatibile delle risorse idriche sotterranee nell’ambito dei sistemi acquiferi prospicienti i territori vulcanici laziali. *Relazione inedita*, 132 Università degli Studi di Roma III, dipartimento di Scienze Geologiche, laboratorio di Idrogeologia.
- Capelli G. & Mazza R. (2006). Indagini geologiche, strutturali, stratigrafiche e idrogeologiche nell’area di Tivoli Terme (RM) e Villalba di Guidonia (RM). *Convenzione di ricerca, Relazione finale. Università degli studi di Roma TRE. Gruppo di lavoro di idrogeologia. Inedito.*
- Carey, J.M., Moore, R., Petley, D.N. & Siddle, H.J. (2007). Pre-failure behaviour of slope materials and their significance in the progressive failure of landslides. In: R. McInnes, J. Jakeways, H. Fairbank and E. Mathie (Editors), *Landslides and Climate Change: Challenges and Solutions. Proceedings and Monographs in Engineering, Water and Earth Sciences*. Taylor & Francis Ltd, London, pp. 207 - 215.
- Carnec, C., Massonnet, D., & King, C. (1996). Two examples of the use of SAR interferometry on displacement fields of small spatial extent. *Geophysical Research Letters*, 23(24), 3579–3582.
- Carucci, V. (2010). *Prospezioni geochemiche e approccio multi-isotopico applicati allo studio di interazione tra acquifero superficiale e profondo nella Piana di Tivoli Roma. Tesi di Dottorato, Università La Sapienza, Roma*
- Carucci, V., Petitta, M., & Aravena, R. (2012). Interaction between shallow and deep aquifers in the Tivoli Plain (Central Italy) enhanced by groundwater extraction: a multi-isotope approach and geochemical modeling. *Applied Geochemistry*, 27(1), 266-280.
- Cascini, L., Fornaro, G., & Peduto, D. (2010). Advanced low- and full-resolution DInSAR map generation for slow-moving landslide analysis at different scales. *Engineering Geology*, 112(1-4), 29–42. doi:10.1016/j.enggeo.2010.01.003
- Centamore, E., Nisio, S., Prestininzi, A. & Scarascia Mugnozza, G. (1997). Evoluzione morfodinamica e fenomeni franosi nel settore periadriatico dell’Abruzzo settentrionale. *Studi Geologici Camerti*, 14, 9-27.
- Chaussard, E., Amelung, F., Abidin, H., & Hong, S. H. (2013). Sinking cities in Indonesia: ALOS PALSAR detects rapid subsidence due to groundwater and gas extraction. *Remote Sensing of Environment*, 128, 150-161.
- Chaussard, E., Wdowinski, S., Cabral-Cano, E., & Amelung, F. (2014). Land subsidence in central Mexico detected by ALOS InSAR time-series. *Remote Sensing of Environment*, 140, 94-106.
- Chen, F., Lin, H., Li, Z., Chen, Q., & Zhou, J. (2012). Interaction between permafrost and infrastructure along the Qinghai–Tibet Railway detected via jointly analysis of C-and L-band small baseline SAR interferometry. *Remote Sensing of Environment*, 123, 532-540.

- Chen, F., Lin, H., & Hu, X. (2014). Slope Superficial Displacement Monitoring by Small Baseline SAR Interferometry Using Data from L-band ALOS PALSAR and X-band TerraSAR: A Case Study of Hong Kong, China. *Remote Sensing*, 6(2), 1564–1586. doi:10.3390/rs6021564
- Cigna, F., Del Ventisette, C., Liguori, V., & Casagli, N. (2011). Advanced radar-interpretation of InSAR time series for mapping and characterization of geological processes. *Natural Hazards and Earth System Sciences*, 865–881. doi:10.5194/nhess-11-865-2011
- Cigna, F., Bianchini, S., & Casagli, N. (2012). How to assess landslide activity and intensity with Persistent Scatterer Interferometry (PSI): the PSI-based matrix approach. *Landslides*, (February). doi:10.1007/s10346-012-0335-7
- Coates, D.F., Yu, Y. & Gyenge, M. (1979). A case history of pit slope design, *Proceedings Fourth International Congress on Rock Mechanics*, Montreaux, Switzerland, pp. 591 - 595.
- Colesanti, C., Ferretti, A., Novali, F., Prati, C. & Rocca, F. (2003a). SAR monitoring of progressive and seasonal ground deformation using the Permanent Scatterers technique. *IEEE Transactions on Geoscience and Remote Sensing* 41, 1685–1700.
- Colesanti, C., Ferretti, A., Prati, C. & Rocca, F. (2003b). Monitoring landslides and tectonic motion with the Permanent Scatterers technique. *Engineering Geology* 68/1–2, 3–14.
- Colesanti, C., & Wasowski, J. (2006). Investigating landslides with space-borne Synthetic Aperture Radar (SAR) interferometry. *Engineering Geology*, 88(3-4), 173–199. doi:10.1016/j.enggeo.2006.09.013
- Colombo, D, Farina, P, Moretti, S, Nico, G, & Prati, C. (2003) Land subsidence in the Firenze-Prato-Pistoia basin measured by means of spaceborne SAR interferometry, *Geoscience and Remote Sensing Symposium, 2003. IGARSS '03. Proceedings. 2003 IEEE International*.
- Colombo, A., Mallen, L., Pispico, R., Giannico, C., Bianchi, M. & Savio, G. (2006). Mappatura regionale delle aree monitorabili mediante l'uso della tecnica PS, In *Proceedings of 10° National Conference ASITA*, Bolzano, ISBN/ISSN:88-900943-0-3-2006, 14–17 November 2006 (in Italian).
- Corominas, J., van Westen, C., Frattini, P., Cascini, L., Malet, J. P., Fotopoulou, S., Catani, F., Van Den Eeckhaut, M., Mavrouli, O., Agliardi, F., Pitilakis, K., Winter, M. G., Pastor, M., Ferlisi, S., Tofani, V., Herva's, J., & Smith, J. T. (2013). Recommendations for the quantitative analysis of landslide risk. *Bulletin of engineering geology and the environment*, 1-55.
- Costantini, M., Falco, S., Malvarosa, F., & Minati, F. (2008). A new method for identification and analysis of persistent scatterers in series of SAR images. In *Geoscience and Remote Sensing Symposium, 2008. IGARSS 2008. IEEE International* (Vol. 2, pp. II-449). IEEE.
- Crosta, G.B. & Agliardi, F. (2003). Failure forecast for large rock slides by surface displacement measurements. *Canadian Geotechnical Journal*, 40, 176-191.
- Cruden, D. M., & Varnes, D. J. (1996). Landslide types and processes. *Landslides: investigation and mitigation*, 247, 36-75.
- Currado, C., Fredi, P. (2000) – Morphometric parameters of drainage basins and morphotectonic setting of eastern Abruzzo. *Memorie della Società Geologica Italiana*, 55, 411-419
- D'Alessandro L. & Pantaleone A. (1987) – Caratteristiche geomorfologiche e dissesti nell'Abruzzo sud-orientale. *Memorie della Società Geologica Italiana*, 37, 805-821.
- D'Alessandro, L., Miccadei, E. & Piacentini, T. (2003) – Morphostructural elements of central-eastern Abruzzi: contributions to the study of the role of tectonics on the morphogenesis of the Apennine chain. *Quaternary International*, 101-102, 115-124.
- Damoah-Afari, P., Ding, X., Lu, Z., Li, Z.W. (2008). Detection ground settlement of Shanghai using interferometric synthetic radar (InSAR) techniques. *The International Archives of the Photogrammetry, Remote Sensing and Spatial Information Sciences* 37 (Part B7), 117–124.
- Demangeot, J. (1965) – Géomorphologie des Abruzzes Adriatiques. *Centre Recherche et Documentation Cartographique, Memoires et Documents*, CNRS, pp. 403, Paris.

- Di Bucci D. & Tozzi M. (1992) – La linea “Ortona-Roccamonfina”: Revisione dei dati esistenti e nuovi contributi per il settore settentrionale (Media valle del Sangro). Studi Geologici Camerti, volume speciale 1991/2, 397-406.
- DiBiagio E. & Flaate K. (2000). Publication Nr. 207: Ralph B. Peck “Engineer, Educator, A Man of Judgement”. Norwegian Geotechnical Institute (NGI), Oslo.
- Dixon, T. H., Amelung, F., Ferretti, A., Novali, F., Rocca, F., Dokka, R., *et al.* (2006). Space geodesy: Subsidence and flooding in New Orleans. *Nature*, 441(7093), 587–588, <http://dx.doi.org/10.1038/441587a>.
- Dragoni, W. (1998). Some considerations on climatic changes, water resources and water needs in the Italian region south of 43 N. In *Water, environment and society in times of climatic change* (pp. 241-271). Springer Netherlands.
- Duncan, J. M. (1996). State of the art: limit equilibrium and finite-element analysis of slopes. *Journal of Geotechnical engineering*, 122(7), 577-596.
- Elachi, C. (1988). *Spaceborne radar remote sensing: applications and techniques*. New York, IEEE Press, 1988, 285 p., 1.
- Emery, J.J. (1979). Simulation of slope creep. In *rock slides & avalanches*. Edited by B. Voight. *Developments in Geotechnical Engineering*, 14b, Elsevier, Amsterdam, 669, 691.
- Faccenna, C. (1994). Structural and hydrogeological features of Pleistocene shear zones in the area of Rome (central Italy). *Annali di Geofisica*, 37 (1), 121-133.
- Faccenna, C., Funicello, R., & Mattei, M. (1994). Late Pleistocene N–S shear zones along the Latium Tyrrhenian margin: structural characters and volcanological implications. *Boll. Geof. Teor. Appl*, 36(141-144), 507-522.
- Faccenna, C., Soligo, M., Billi, A., De Filippis, L., Funicello, R., Rossetti, C., & Tuccimei, P. (2008). Late Pleistocene depositional cycles of the Lapis Tiburtinus travertine (Tivoli, Central Italy): Possible influence of climate and fault activity. *Global and Planetary Change*, 63(4), 299-308.
- Fanucci, F., Moretti, E., Nesci, O., Savelli, D. & Veneri, F. (1996) – Tipologia dei terrazzi vallivi ed evoluzione del rilievo nel versante Adriatico dell’Appennino centro-settentrionale. *Il Quaternario*, 9 (1), 255-258.
- Farabollini, P. & Nisio, S. (1997) – Evoluzione geomorfologica quaternaria del bacino del F. Vomano (Abruzzo). *Il Quaternario*, 10, 101-104.
- Farina, P., Colombo, D., Fumagalli, A., Marks, F., & Moretti, S. (2006). Permanent Scatterers for landslide investigations: outcomes from the ESA-SLAM project. *Engineering Geology*, 88(3-4), 200–217. doi:10.1016/j.enggeo.2006.09.007
- Farina, P., Casagli, N., & Ferretti, A. (2007). Radar-interpretation of InSAR measurements for landslide investigations in civil protection practices. In *First North American Landslide Conference* (pp. 272-283).
- Ferretti, A., Prati, C., & Rocca, F. (2000). Nonlinear subsidence rate estimation using permanent scatterers in differential SAR interferometry. *IEEE Transactions on Geoscience and Remote Sensing*, 38(5), 2202–2212. doi:10.1109/36.868878
- Ferretti, A., Prati, C. & Rocca, F. (2001). Permanent scatterers in SAR interferometry. *IEEE Trans. Geosc. and Remote Sens.* 39(1), 8-20.
- Ferretti, A., Prati, C., Rocca, F., Nicola, C., Farina, P., & Young, B. (2005). Permanent Scatterers technology: a powerful state of the art tool for historic and future monitoring of landslides and other terrain instability phenomena. In *International Conference on Landslide Risk Management*. AA Balkema, Vancouver, Canada.
- Ferretti, A., Monti-Guarnieri, A., Prati, C., Rocca, F., & Massonnet, D. (2007). *InSAR Principles-Guidelines for SAR Interferometry Processing and Interpretation*. (K. Fletcher, Ed.) (ESA Public.). Noordwijk, The Netherlands: ESA Publications. Retrieved from <http://adsabs.harvard.edu/abs/2007ESATM>

- Ferretti, A., Fumagalli, A., Novali, F., Prati, C., Rocca, F., & Rucci, A. (2011). A new algorithm for processing interferometric data-stacks: SqueeSAR. *Geoscience and Remote Sensing, IEEE Transactions on*, 49(9), 3460-3470.
- Fournier, M., Bellahsen, N., Fabbri, O., & Gunnell, Y. (2004). Oblique rifting and segmentation of the NE Gulf of Aden passive margin. *Geochemistry, Geophysics, Geosystems*, 5(11).
- Franceschetti, G., Lanari, R. & Marzouk, E.S. (1995), Efficient and high precision space-variant processing of SAR data. *IEEE Trans. Aerosp. Electron. Syst.*, 31, 227.
- Franceschetti, G., & Lanari, R. (1999), *Synthetic Aperture Radar Processing*, CRC Press, Boca Raton, Florida.
- Franchi S. (2012). Effetti del depauperamento dell'acquifero principale della piana di Tivoli-Guidonia sulla compattazione dei sedimenti recenti. Tesi di laurea, Università La Sapienza, Roma.
- Froude, Melanie, Jane (2011). Capturing and characterising pre-failure strain on failing slopes, Durham theses, Durham University. Available at Durham E-Theses Online: <http://etheses.dur.ac.uk/3272/>
- Fruneau, B., Achache, J., & Delacourt, C. (1996). Observation and modelling of the Saint-Étienne-de-Tinée landslide using SAR interferometry. *Tectonophysics*, 265, 181–190.
- Fruneau, B., & Sarti, F. (2000). Detection of ground subsidence in the city of Paris using radar interferometry: Isolation of deformation from atmospheric artifacts using correlation, *Geophysical Research Letters*, Vol. 27:3981–3984.
- Fukuzono, T. (1985). A new method for predicting the failure time of a slope. *Proc. IV International Conference and Field Workshop on Landslides*, Tokyo.
- Funicello, R., Faccenna, C., De Filippis, L. & Rossetti, C. (2005). Indagini per determinare le cause dei dissesti agli edifici di Via Cesare Augusto, e aree limitrofe, in località Bagni di Tivoli: Assetto strutturale e Microzonazione sismica. Rep. Cron. N.3561 del 17.01.05
- Gabriel, A. K. & Goldstein, R. M. (1988), Crossed orbit interferometry: theory and experimental results from SIR-B, *Int.J. Remote Sensing*, 9(5):857–872.
- Gabriel, A., Goldstein, R., & Zebker, H. A. (1989). Mapping small elevation changes over large areas — Differential radar interferometry. *Journal of Geophysical Research-Solid Earth and Planets*, 94, 9183–9191.
- García-Davalillo, J. C., Herrera, G., Notti, D., Strozzi, T., & Álvarez-Fernández, I. (2014). DInSAR analysis of ALOS PALSAR images for the assessment of very slow landslides: the Tena Valley case study. *Landslides*. 11:225-246. doi:10.1007/s10346-012-0379-8.
- Ghezzi, G., Peralta, J.C., Bianchi, A., Sartini, S., Anfuso, A., Creatini, F., Cassitelli, M., Ghezzi, R., Pellegrini, M., Porsia, D., & Rizza, L. (2012). Geophysical site investigation for Hasik landslides stretch from km 7+000 to km 8+500 (Unpublished technical report).
- Gigli, G., Fanti, R., Canuti, P. & Casagli, N. (2011). Integration of advanced monitoring and numerical modeling techniques for the complete risk scenario analysis of rockslides: The case of Mt. Beni (Florence, Italy). *Elsevier. Engineering Geology* 120 (2011) 48-59.
- Glastonbury, B. & Fell, R. (2000). Report on the analysis of rapid natural rock slope.
- Glastonbury, B. & Fell, R. (2002). Report on the analysis of the deformation behaviour.
- Goldstein, R., Zebker, H. A. & Werner, C. L. (1988), Satellite radar interferometry: Two-dimensional phase unwrapping, *Radio Science*, 23(4):713–720.
- Goldstein, R., Engelhardt, H., Kamb, B., & Frolich, R. (1993). Satellite radar interferometry for monitoring ice-sheet motion: application to an Antarctic ice stream. *Science*, 262, 1525–1530.
- Gonzalez-Diez, A., Remondo, J., Diaz, de Teràn, R. & Cendrero, A. (1999). A methodological approach for the analysis of the temporal occurrence and triggering factors of landslides.
- Got, J.L., Mourot, P. & Grangeon, J. (2010). Pre-failure behaviour of an unstable limestone cliff from displacement and seismic data. *Nat. Hazards Earth Syst. Sci.*, 10, 819-829.

- Graham, L. C. (1974) Synthetic Interferometer Radar for Topographic Mapping, *Proc. of the IEEE*, 62(2), 763-768.
- Guéguen, Y., Deffontaines, B., Fruneau, B., Al Heib, M., De Michele, M., Raucoules, D., ... & Planchenault, J. (2009). Monitoring residual mining subsidence of Nord/Pas-de-Calais coal basin from differential and Persistent Scatterer Interferometry (Northern France). *Journal of Applied Geophysics*, 69(1), 24-34.
- Gustavii, B. (2012). *How to Prepare a Scientific Doctoral Dissertation Based on Research Articles*. Cambridge University Press.
- Guzzetti, F., Carrara, A., Cardinali, M., & Reichenbach, P. (1999). Landslide hazard evaluation: a review of current techniques and their application in a multi-scale study, Central Italy. *Geomorphology*, 31(1), 181-216.
- Guzzetti, F., Mondini, A. C., Cardinali, M., Fiorucci, F., Santangelo, M., & Chang, K. T. (2012). Landslide inventory maps: New tools for an old problem. *Earth-Science Reviews*, 112(1), 42-66.
- Haefeli, R. (1953). Creep problems in soils, snow and ice. *Proc. 3rd Int. Conf. on Soil Mechanics and Foundation Engineering* 3: 238–251.
- Hanssen, R. (2001). *Radar interferometry, data interpretation and error analysis*. Kluwer Academic Publishers.
- Hanssen, R. F. (2005). Satellite radar interferometry for deformation monitoring: a priori assessment of feasibility and accuracy. *International Journal of Applied Earth Observation and Geoinformation*, 6(3), 253-260.
- Harbaugh, A. W. (2005). MODFLOW-2005, the US Geological Survey modular ground-water model: The ground-water flow process (pp. 6-A16). US Department of the Interior, US Geological Survey.
- Heleno, S. I., Oliveira, L. G., Henriques, M. J., Falcão, A. P., Lima, J. N., Cooksley, G., ... & Fonseca, J. F. (2011). Persistent Scatterers Interferometry detects and measures ground subsidence in Lisbon. *Remote Sensing of Environment*, 115(8), 2152-2167.
- Hilley, G. E., Bürgmann, R., Ferretti, A., Novali, F., & Rocca, F. (2004). Dynamics of slow-moving landslides from permanent scatterer analysis. *Science*, 304(5679), 1952-1955.
- Hoffmann, J., Zebker, H. A., Galloway, D. L., & Amelung, F. (2001). Seasonal subsidence and rebound in Las Vegas Valley, Nevada, observed by synthetic aperture radar interferometry. *Water Resources Research*, 37(6), 1551-1566.
- Hong, Y., Adler, R., & Huffman, G. (2007). Use of satellite remote sensing data in the mapping of global landslide susceptibility. *Natural Hazards*, 43(2), 245-256.
- Hooper, A., Zebker, H., Segall, P., & Kampes, B. (2004). A new method for measuring deformation on volcanoes and other natural terrains using InSAR persistent scatterers. *Geophysical Research Letters*, 31(23), L23611. doi:10.1029/2004GL021737
- Hu, J., Li, Z.W., Ding, X.L., Zhu, J.J., Zhang, L. & Sun, Q., (2014). Resolving three-dimensional surface displacements from InSAR measurements: A review, *Earth Science Reviews*, doi: 10.1016/j.earscirev.2014.02.005.
- Hungr, O. & Kent, A. (1995). Coal Mine Waste Dump Failures in British Columbia, Canada. *Landslide News*. N°9 (December 1995).
- Hung, W. C., Hwang, C., Chen, Y. A., Chang, C. P., Yen, J. Y., Hooper, A., & Yang, C. Y. (2011). Surface deformation from persistent scatterers SAR interferometry and fusion with leveling data: A case study over the Choushui River Alluvial Fan, Taiwan. *Remote Sensing of Environment*, 115(4), 957-967.
- Hungr, O. (1995). A model for the runout analysis of rapid flow slides, debris flows, and avalanches. *Canadian Geotechnical Journal*, 32(4), 610-623.
- IUGS (1995). A suggested method for describing the rate of movement of a landslide. *Bulletin of Engineering Geology and the Environment*, 52, 75-78.

- Jebur, M. N., Pradhan, B., & Tehrany, M. S. (2013). Using ALOS PALSAR derived high-resolution DInSAR to detect slow-moving landslides in tropical forest: Cameron Highlands, Malaysia. *Geomatics, Natural Hazards and Risk*, 0(0), 1–19. doi:10.1080/19475705.2013.860407.
- Jenkins, S. F., Spence, R. J. S., Fonseca, J. F. B. D., Solidum, R. U., & Wilson, T. M. (2014). Volcanic risk assessment: Quantifying physical vulnerability in the built environment. *Journal of Volcanology and Geothermal Research*, 276, 105-120.
- Jung, H.C., Kim, S.W., Jung, H.S., Min, K.D. & Won, J.S. (2007). Satellite observation of coal mining subsidence by persistent scatterer analysis. *Engineering Geology*, 92, 1–13.
- Kampes, B. M. (2006). *Radar Interferometry Persistent Scatterers Technique*. (Springer, Ed.). Dordrecht, The Netherlands.
- Keqiang, H. & Sijing, W. (2006). Double parameter threshold and its formation mechanism of the colluvial landslide: Xintan landslide, China. *Environmental Geology*, 49(5): 696 - 707
- Kennedy, B.A. & Niermeyer, K.E. (1970). Slope monitoring systems used in the prediction of a major slope failure at the Chuquicamata Mine, Chile, Proceedings of the symposium on Planning Open Pit Mines. Balkema, Amsterdam, Johannesburg, South Africa, pp. 215 - 225.
- Kilburn, C. R., & Petley, D. N. (2003). Forecasting giant, catastrophic slope collapse: lessons from Vajont, Northern Italy. *Geomorphology*, 54(1), 21-32.
- Kim, K. D., Lee, S., Oh, H. J., Choi, J. K., & Won, J. S. (2006). Assessment of ground subsidence hazard near an abandoned underground coal mine using GIS. *Environmental Geology*, 50(8), 1183-1191.
- Kwok, R., & Fahnestock, M. a. (1996). Ice sheet motion and topography from radar interferometry. *IEEE Transactions on Geoscience and Remote Sensing*, 34 (1), 189–200. doi:10.1109/36.481903.
- La Vigna, F. (2009). Groundwater flow model of the hydrothermal groundwater unit of the Acque Albule, Rome. Phd Thesis, XXI Italian PhD Cycle. RomaTRE University.
- La Vigna, F., Mazza, R, Capelli, G. (2012). Detecting the flow relationships between deep and shallow aquifers in an exploited groundwater system, using long-term monitoring data and quantitative hydrogeology: the Acque Albule basin case (Rome, Italy). *Hydrological Processes*.
- Lanari, R., Lundgren, P., Manzo, M., & Casu, F. (2004). Satellite radar interferometry time series analysis of surface deformation for Los Angeles, California. *Geophysical Research Letters*, 31(23).
- Lauknes, T. R. (2004). Long-term surface deformation mapping using small-baseline differential SAR interferograms. Unpublished Master Thesis, Department of Physics and Technology, University of Tromsø.
- Lauknes, T., & Shanker, A. P. (2010). Detailed rockslide mapping in northern Norway with small baseline and persistent scatterer interferometric SAR time series methods. *Remote Sensing of Environment*, 114(9), 2097–2109. doi:10.1016/j.rse.2010.04.015
- Lee, S. (2005). Application of logistic regression model and its validation for landslide susceptibility mapping using GIS and remote sensing data. *International Journal of Remote Sensing*, 26(7), 1477-1491.
- Lepvrier, C., Fournier, M., Bérard, T., & Roger, J. (2002). Cenozoic extension in coastal Dhofar (southern Oman): implications on the oblique rifting of the Gulf of Aden. *Tectonophysics*, 357(1), 279-293.
- Li, F. & Goldstein, R. (1987). Studies of Multi-baseline Spaceborne Interferometric Synthetic Aperture Radar, in: *International Geoscience and Remote Sensing Symposium*, Ann Arbor, 18–21 May 1987, pp. 1545–1550.
- Li, F. K. & Goldstein, R. M. (1990). Studies of Multibaseline Spaceborne Interferometric Synthetic Aperture Radars, *IEEE Transactions on Geoscience and Remote Sensing*, 28(1): 88–97.
- Lombardi, L. (2005). Indagini geochimiche per determinare le cause dei dissesti agli edifici di Via Cesare Augusto ed aree limitrofe, in località Bagni di Tivoli. Analisi di campioni di acqua e gas. Contratto di ricerca Regione Lazio n. 5350 del 11/01/2005.
- Luzi, G. (2010). Ground based SAR interferometry: a novel tool for Geoscience. *Geoscience and Remote Sensing New Achievements*, 508pp.

- Main, I. G. (2000). A damage mechanics model for power - law creep and earthquake aftershock and foreshock sequences. *Geophysical Journal International*, 142(1), 151-161.
- Martin, D.C. (1993). Time dependent deformation of rock slopes, University of London. Massey,
- Massonnet, D., Rossi, M., Carmona, C., Adragna, F., Peltzer, G., Feigl, K., & Rabaute, T. (1993). The displacement field of the Landers earthquake mapped by radar interferometry. *Nature*, 364 (6433), 138-142.
- Massonnet, D., Feigl, K., Rossi, M., & Adragna, F. (1994). Radar interferometric mapping of deformation in the year after the Landers earthquake. *Nature*, 369 (6477), 227-230.
- Massonnet, D., Briole, P., & Arnaud, A. (1995). Deflation of Mount Etna monitored by spaceborne radar interferometry. *Nature*, 375 (6532), 567-570.
- Maxia C. (1950). Il Bacino delle Acque Albule (Lazio). *Contributi di Scienze Geologiche, Supp. Ric. SC.* 20-27, Univ. Roma.
- Mazzanti, P., & Brunetti, A. (2010). Assessing rockfall susceptibility by terrestrial SAR interferometry. In *Proceedings of the mountain risks international conference*, Florence, Italy (pp. 24-26).
- Mazzanti, P. (2011). Displacement monitoring by terrestrial SAR interferometry for geo- technical purposes. *Geotech Instrum News* 29(2):25–28.
- Mazzanti, P., Bozzano, F., Esposito, F. Cipriani, I. (2011). Temporal prediction of landslides failure by continuous TInSAR monitoring. *Proc. of 8th International Symposium on Field Measurements in GeoMechanics Berlin, Germany*, September 12-16, 2011.
- Mazzanti, P. (2012). Remote monitoring of deformation. An overview of the seven methods described in previous GINs. *Geotechnical Instrumentation News*, (December), pp. 24-29.
- Mazzanti P., Rocca A., Bozzano F., Cossu R. & Floris M. (2012). Landslides forecasting analysis by time series displacement derived from satellite InSAR data: preliminary results. In: *ESA-ESRIN, Frascati (RM), Italy, September 2011*, Noordwijk:L. Ouwehand, ISBN: 9789290922612.
- Mazzanti, P., Bozzano, F., Cipriani, I., & Prestininzi, A. (2014). New insights into the temporal prediction of landslides by a terrestrial SAR interferometry monitoring case study. *Landslides*, (January). doi:10.1007/s10346-014-0469-x
- Meckel, T. A., Brink, ten, U. S., & Williams, S. J. (2006). Current subsidence rates due to compaction of Holocene sediments in southern Louisiana. *Geophysical Research Letters*, 33(11),
- Meisina, C., Zucca, F., Fossati, D., Ceriani, M., & Allievi, J. (2006). Ground deformation monitoring by using the Permanent Scatterers Technique: The example of the Oltrepo Pavese (Lombardia, Italy). *Engineering Geology*, 88(3-4), 240–259. doi:10.1016/j.enggeo.2006.09.010
- Meng, S. L. & Yang, C. (2011). Prediction of Landslide Deep Displacement Using Improved Genetic Algorithm Based on Time Series Analysis. *2011 International Conference on System Science, Engineering Design and Manufacturing Informatization*. 978-1-4577-0246-4/11/\$26.00.
- Mercolli, I., Briner, A.P., Frei, R., Schönberg, R., Nægler, T.F., Kramers, J., & Peters, T. (2006). Lithostratigraphy and geochronology of the Neoproterozoic crystalline basement of Salalah, Dhofar, Sultanate of Oman: *Precambrian Research*, v. 145, p. 182–206.
- Miccadei, E. (1993) – *Geologia dell’area Alto Sagittario-Alto Sangro*. *Geologica Romana*, 29, 463-481.
- Modoni, G., Darini, G., Spacagna, R. L., Saroli, M., Russo, G., & Croce, P. (2013). Spatial analysis of land subsidence induced by groundwater withdrawal. *Engineering Geology*, 167, 59-71.
- Moreira, A., Prats-Iraola, P., Younis, M., Krieger, G., Hajnsek, I., & Papathanassiou, K. (2013). A tutorial on synthetic aperture radar. *IEEE Geoscience and Remote Sensing Magazine*, (March), 6–43.
- Mufundirwa, A., Fujii, Y. & Kodama, J. (2010). A new practical method for prediction of geomechanical failure - time. *International Journal of Rock Mechanics and Mining Sciences*, 47(7): 1079 - 1090.
- Muller, L. (1964) - The rock-slide in the Vajont Valley. *Int. J. Rock Mechanics and Mining Sciences*, 2, 148-212.

- Mostardini, F. & Merlini, S. (1986). Appennino centro-meridionale. Sezioni geologiche e proposta di un modello strutturale. *Memorie della Società Geologica Italiana*, 35, 177-202.
- Notti, D., Davalillo, J. C., Herrera, G. & Mora, O. (2010). Assessment of the performance of X-band satellite radar data for landslide mapping and monitoring: Upper Tena Valley case study. *Natural Hazards and Earth System Science*, 10(9), 1865–1875. doi:10.5194/nhess-10-1865-2010
- Okamoto, T., Larsen, J. O., Matsuura, S., Asano, S., Takeuchi, Y. & Grande, L. (2004). Displacement properties of landslide masses at the initiation of failure in quick clay deposits and the effects of meteorological and hydrological factors. *Engineering geology*, 72(3), 233-251.
- Olshansky, RB (1996) Planning for hillside development, American Planning Association Planning Advisory Service Report no. 466, 50 pp
- Osmanoğlu, B., Dixon, T. H., Wdowinski, S., Cabral-Cano, E., & Jiang, Y. (2011). Mexico City subsidence observed with persistent scatterer InSAR. *International Journal of Applied Earth Observation and Geoinformation*, 13(1), 1-12.
- Parise, M. (2001). Landslide mapping techniques and their use in the assessment of the landslide hazard. *Physics and Chemistry of the Earth, Part C: Solar, Terrestrial & Planetary Science*, 26(9), 697–703. doi:10.1016/S1464-1917(01)00069-1
- Parise, M. & Wasowski, J. (1999). Landslide activity maps for landslide hazard evaluation: three case studies from Southern Italy. *Nat Hazards* 20(2):159–183
- Patacca E. & Scandone P. (2007). Geology of the Southern Apennines. *Bollettino della Società Geologica Italiana*, Spec. Issue 7, 75-199.
- Perissin, D., Piantanida, R., Piccagli, D., & Rocca, F. (2007). Landslide in Dossena (BG): comparison between interferometric techniques.
- Perissin, D. (2008). Validation of the submetric accuracy of vertical positioning of PSs in C-band. *Geoscience and Remote Sensing Letters, IEEE*, 5(3), 502-506.
- Perissin, D. (2009). SARPROZ Manual: https://engineering.purdue.edu/~perissin/manual/main_master.html.
- Perissin D., Wang Z. & Wang T. (2011) - The SARPROZ InSAR tool for urban subsidence/manmade structure stability monitoring in China. Proc. of ISRSE 2010, Sidney, Australia, 10-15 April 2011.
- Perissin, D. & Wang, T. (2012). Repeat-Pass SAR Interferometry With Partially Coherent Targets. *IEEE Trans. on Geosc. and Remote Sens.* 50(1), 271, 280.
- Perissin, D., Wang, Z., & Lin, H. (2012). Shanghai subway tunnels and highways monitoring through Cosmo-SkyMed Persistent Scatterers. *ISPRS Journal of Photogrammetry and Remote Sensing*, 73, 58-67.
- Petitta, M. & Del Bon, A. (2003). Indagini idrogeologiche sulle Sorgenti delle Acque Albule (Bagni di Tivoli).
- Petitta, M., Primavera, P., Tuccimei, P., & Aravena, R. (2011). Interaction between deep and shallow groundwater systems in areas affected by Quaternary tectonics (Central Italy): a geochemical and isotope approach. *Environmental Earth Sciences*, 63(1), 11-30.
- Petley, D.N., Bulmer, M.H. & Murphy, W. (2002). Patterns of movement in rotational and translational landslides. *Geology*, 30(8): 719 - 722.
- Petley, D. N., Mantovani, F., Bulmer, M. H., & Zannoni, A. (2005). The use of surface monitoring data for the interpretation of landslide movement patterns. *Geomorphology*, 66(1), 133-147.
- Petley, D. & Rosser, N.J. (2006). On the mechanics of a typhoon induced landslide, Proceedings of the 10th Taiwan Geography Conference. The Geographical Society of China, Taipei, pp. 150–162. 177.
- Phien-wej, N., Gao, P.H., Nutalaya, P. (2006). Land subsidence in Bangkok, Thailand *Engineering Geology*, 82, pp. 187– 201.
- Picarelli, L., Oboni, F., Evans, S.G., Mostyn, G. and Fell, R., (2005). Hazard characterization and quantification. In: O. Hungr, R. Fell, R. Couture and E. Eberhardt (Editors), *Landslide Risk Management*. Taylor & Francis Group, London, pp. 27 - 61.

- Platel, J.P. & Roger, J. (1989). Evolution géodynamique du Dhofar (Sultanat d'Oman) pendant le Crétacé et le Tertiaire en relation avec l'ouverture du golfe d'Aden. *Bull. Soc. Geol. Fr.* 2, 253–263.
- Platel, J.P., Roger, J., Peters, T.J., Mercolli, I., Kramers, J.D. & Le Me'tour, J. (1992). Geological map of Salalah, Sultanate of Oman; sheet NE 40-09, scale 1:250000, Oman Ministry of Petroleum and Minerals, Directorate General of Minerals.
- Prati, C., Rocca, F., Monti Guarnieri, A. & Damonti, E. (1990), Seismic Migration For SAR Focussing: Interferometrical Applications, *IEEE Transactions on Geoscience and Remote Sensing*, 28(4):627–640.
- Prestininzi, A. (2008). Relazione conclusiva relativa alle convenzioni stipulate tra il Centro di Ricerca CE.RI. e la Regione Lazio (30/01/2006 e successiva del 04/07/2006), inerente agli studi e alle indagini condotte nelle zone soggette a fenomeni di subsidenza di Tivoli-Guidonia. CERI La Sapienza – Regione Lazio Protezione Civile.
- Qiao, G., Lu, P., Scaioni, M., Xu, S., Tong, X., & Feng, T. (2013). Landslide investigation with remote sensing and sensor network: From susceptibility mapping and scaled-down simulation towards in situ sensor network. *Remote Sensing*, 4319–4346. doi:10.3390/rs5094319
- Raspini, F., Loupasakis, C., Rozos, D., & Moretti, S. (2013). Advanced interpretation of land subsidence by validating multi-interferometric SAR data: the case study of the Anthemountas basin (Northern Greece). *Natural Hazards & Earth System Sciences*, 13(10).
- Raucoules, D., Le Mouélic, S., Carnec, C., Maisons, C., & King, C. (2003). Urban subsidence in the city of Prato (Italy) monitored by satellite radar interferometry. *International journal of remote sensing*, 24(4), 891-897.
- Raucoules, D., Colesanti, C., & Carnec, C. (2007). Use of SAR interferometry for detecting and assessing ground subsidence. *Comptes Rendus Geoscience*, 339(5), 289-302.
- Raucoules, D., Bourguine, B., De Michele, M., Le Cozannet, G., Closset, L., Bremmer, C., ... & Engdahl, M. (2009). Validation and intercomparison of Persistent Scatterers Interferometry: PSIC4 project results. *Journal of Applied Geophysics*, 68(3), 335-347.
- Reid, G. & Stewart, D. (1986). A large scale toppling failure at Afton, *Proceedings International Symposium on Geotechnical Stability in Surface Mining* Calgary, Canada, pp. 215 - 223.
- Riedel, B., & Walther, A. (2008). InSAR processing for the recognition of landslides. *Advances in Geosciences*, 14(14), 189-194.
- Robertson, A. H. F. & Bamkhalif, K. A. S. (2001). Late Oligocene-early Miocene rifting of the northeastern Gulf of Aden: basin evolution in Dhofar (southern Oman), in P. A. Ziegler, W. Cavazza, A. H. F. Robertson, and S. Crasquin-Soleau Eds, *Peri-Tethys Memoir 6: Perihal- 00021620*, version Tethyan Rift/Wrench Basins and Passive Margins, *Mém. Mus. Natn. Hist. Nat.*, 186, 641- 670.
- Rockaway, J.D. (1976). The influence of map scale on engineering geologic mapping. *Rull. Int. Ass. Eng. Geol.* 14, I 19-I 22.
- Roger, J., Platel, J.P., Cavelier, C. & Bourdillon de Grissac, C. (1989). Données nouvelles sur la stratigraphie et l'histoire géologique du Dhofar (Sultanat d'Oman). *Bull. Soc. GCol. Fr.* 8 (2) 265-277.
- Roger, J., Platel, J.P., Berthiaux, A. & Le Me'tour, J. (1992). Geological map of Hawf with Explanatory Notes; sheet NE 39-16, scale 1:250000, Oman Ministry of Petroleum and Minerals, Directorate General of Minerals.
- Rose, N.D. & Hungr, O. (2007). Forecasting potential rock slope failure in open pit mines using the inverse-velocity method. *International Journal of Rock Mechanics & Mining Sciences* 44 (2007) 308-320.
- Rosella, L. (2007). Indagine sui rapporti tra assetto idrogeologico ed attività antropiche nella Piana di Guidonia-Tivoli. Tesi di Laurea, Università La Sapienza, Roma.
- Ryan, T.M. & Call, R.D. (1992). Applications of rock mass monitoring for stability assessment of pit slope failure. In: Tillerson and Wawersik (Editors), *Rock Mechanics, Proceedings of the 33rd US Symposium*. Balkema, Rotterdam, Santa Fe, New Mexico, pp. 221 - 229.

- Saito, M. & Uezawa H. (1961). Failure of soil due to creep. Proceedings of the 6th ICSMFE 1: 315–318. Paris.
- Saito, M. (1965). Forecasting the time of occurrence of a slope failure. Proceedings of the 6th International Conference on Soil Mechanics and Foundation Engineering 2: 537–539.
- Saito, M. (1969). Forecasting time of slope failure by Tertiary creep. Proceedings of the 7th International Conference on Soil Mechanics and Foundation Engineering 2: 677–683.
- Saito, M. (1979). Evidential study on forecasting occurrence of slope failure. Trans. of the Dept. of Geomech. Armenian Academy of Sciences, Yerevan, URSS.
- Salt, G. (1988). Landslide mobility and remedial measure.
- Salvati, R., & Sasowsky, I. D. (2002). Development of collapse sinkholes in areas of groundwater discharge. *Journal of Hydrology*, 264(1), 1-11.
- Salvi, S., Pirro, M., Gasparini, C., Stramondo, S., Pagliuca, M.N., Atzori, S., Colini, L., Tolomei, C., Doumaz, F., Ferretti, A. & Allievi, J. (2004). Le deformazioni del suolo ricavate da dati satellitari in un settore a rischio sinkhole del Bacino delle Acque Albule (Lazio). 1° Convegno APAT, Roma, 20-21 Maggio, pp. 623-632.
- Samsonov, S., d'Oreye, N., & Smets, B. (2013). Ground deformation associated with post-mining activity at the French–German border revealed by novel InSAR time series method. *International Journal of Applied Earth Observation and Geoinformation*, 23, 142-154.
- Sarkar, S., & Kanungo, D. P. (2004). An Integrated Approach for Landslide Susceptibility Mapping Using RemoteSensing and GIS. *Photogrammetric engineering and remote sensing*, 70(5), 617-626.
- Sbarbati, C. (2008). Indagini idrogeologiche nella Piana di Tivoli-Guidonia (Roma). Tesi di Laurea, Università La Sapienza, Roma.
- Schuster, R. L., & Highland, L. (2001). Socioeconomic and environmental impacts of landslides in the Western Hemisphere. US Department of the Interior, US Geological Survey.
- Scisciani, V., Calamita, F., Tavarnelli, E., Rusciardelli, G., Ori, G.G. & Paltrinieri, W. (2001) – Foreland-dipping normal faults in the inner edges of syn-orogenic basins: a case from the Central Apennines, Italy. *Tectonophysics*, 330(3-4), 211-224.
- Siddle, H.J., Moore, R., Carey, J.M. & Petley, D.N. (2007). Pre-failure behaviour of slope materials and their significance in the progressive failure of landslides, In: E. Mathie; R. McInnes; H. Fairbank; J. Jakeways; (eds) *Landslides and Climate Change: Challenges and Solutions*, Proceedings of the International Conference on Landslides and Climate Change. 10.1201/NOE0415443180.ch25.
- Simons, M., Fialko, Y., & Rivera, L. (2002). Coseismic deformation from the 1999 Mw 7.1 Hector Mine, California, earthquake as inferred from InSAR and GPS observations. *Bulletin of the Seismological Society of America*, 92(4), 1390-1402.
- Simons, M., & Rosen, P. A. (2007). *Interferometric synthetic aperture radar geodesy*. Elsevier.
- Singh, L. P., Westen, C. J., Champati Ray, P. K., & Pasquali, P. (2005). Accuracy assessment of InSAR derived input maps for landslide susceptibility analysis: a case study from the Swiss Alps. *Landslides*, 2(3), 221–228. doi:10.1007/s10346-005-0059-z
- Singhroy, V., Mattar, K., & Gray, A. (1998). Landslide characterisation in Canada using interferometric SAR and combined SAR and TM images. *Advances in Space Research*, 21(3).
- Siqing, Q. & Sijing, W. (2000). A homomorphic model for identifying abrupt abnormalities of landslide forerunners. *Engineering Geology*, 57(3): 163 - 168.
- Smith, K. (2013). *Environmental hazards: assessing risk and reducing disaster*. Routledge.
- Stramondo, S., Bozzano, F., Marra, F., Wegmuller, U., Cinti, F. R., Moro, M. & Saroli, M. (2008) - Subsidence induced by urbanisation in the city of Rome detected by advanced InSAR technique and geotechnical investigations. *Remote Sensing of Environment*, 112(6): 3160-3172.

- Strappaveccia, C. (2007). Valutazione qualitativa e quantitativa della pressione antropica nell'area subsidente di Tivoli e Guidonia attraverso tecniche di telerilevamento. Tesi di Laurea, Università La Sapienza, Roma.
- Strozzi, T., Farina, P., Corsini, A., Ambrosi, C., Thüring, M., Zilger, J., Wiesmann, A., Wegmuller, U. & Werner, C. (2005). Survey and monitoring of landslide displacements by means of L-band satellite SAR interferometry. *Landslides*, 2(3), 193–201. doi:10.1007/s10346-005-0003-201
- Strozzi, T., Delaloye, R., Käab, A., Ambrosi, C., Perruchoud, E., & Wegmüller, U. (2010). Combined observations of rock mass movements using satellite SAR interferometry, differential GPS, airborne digital photogrammetry, and airborne photography interpretation. *Journal of Geophysical Research: Earth Surface* (2003–2012), 115(F1).
- Strozzi, T., Ambrosi, C., & Raetzo, H. (2013). Interpretation of aerial photographs and satellite SAR interferometry for the inventory of landslides. *Remote Sensing*, 5(5), 2554-2570.
- Syvitski, J. P., Kettner, A. J., Overeem, I., Hutton, E. W., Hannon, M. T., Brakenridge, G. R., Day, J., Vörösmarty, C., Saito, Y., Giosan, L. & Nicholls, R. J. (2009). Sinking deltas due to human activities. *Nature Geoscience*, 2 (10), 681-686.
- Teatini, P., Castelletto, N., Ferronato, M., Gambolati, G., Janna, C., Cairo, E., ... & Bottazzi, F. (2011). Geomechanical response to seasonal gas storage in depleted reservoirs: A case study in the Po River basin, Italy. *Journal of Geophysical Research: Earth Surface* (2003–2012), 116(F2).
- Terzaghi, K. 1950. Mechanisms of landslides, in Applications of geology to engineering practice. Geol. Soc. Amer. Spec. Pub 83–123. Berkley.
- Tesauro, M., Berardino, P., Lanari, R., Sansosti, E., Fornaro, G., & Franceschetti, G. (2000). Urban subsidence inside the city of Napoli (Italy) observed by satellite radar interferometry. *Geophysical Research Letters*, 27(13), 1961-1964.
- Thompson, P.W. & Cierlitz, S., (1993). Confirmation of a failure mechanism using open pit monitoring methods, Proceedings of the Australian Conference on Geotechnical Instrumentation and Monitoring in Open Pit and Underground Mining. Balkema, Kalgoorlie, pp. 483 - 489.
- Tofani, V., Raspini, F., Catani, F., & Casagli, N. (2013). Persistent Scatterer Interferometry (PSI) Technique for Landslide Characterization and Monitoring. *Remote Sensing*, 1045–1065. doi:10.3390/rs5031045
- Tomás, R., Herrera, G., Delgado, J., Lopez-Sanchez, J. M., Mallorquí, J. J., & Mulas, J. (2010). A ground subsidence study based on DInSAR data: calibration of soil parameters and subsidence prediction in Murcia City (Spain). *Engineering Geology*, 111(1), 19-30.
- Tong, X., Sandwell, D. T., & Fialko, Y. (2010). Coseismic slip model of the 2008 Wenchuan earthquake derived from joint inversion of interferometric synthetic aperture radar, GPS, and field data. *Journal of Geophysical Research: Solid Earth* (1978–2012), 115(B4).
- Ulusay, R. & Aksoy, H., (1994). Assessment of the failure mechanism of a highwall slope under spoil pile loadings at a coal mine. *Engineering Geology*, 38(1): 117 - 134.
- Van Leijen, F. J., & Hanssen, R. F. (2007). Persistent scatterer density improvement using adaptive deformation models. In *Geoscience and Remote Sensing Symposium, 2007. IGARSS 2007. IEEE International* (pp. 2102-2105). IEEE.
- Varnes, D.J. (1974) The logic of geological maps, with special reference to their interpretation and use for engineering purposes, U.S. Geol. Survey Prof. Paper 837, 48 pp.,
- Varnes, D.J. (1978) – Slope movement types and processes. Transportation Research Board Special Report, 176.
- Varnes, D.J. (1984) Landslide hazard zonation: a review of principles and practice, Unesco. Paris, Natural Hazards, 3,63 pp.
- Voight, B. (1988). A method for prediction of volcanic eruptions. *Nature*, 332(6160), 125-130.
- Voight, B. (1989). A relation to describe rate-dependant material failure. *Science*, 243, 200-203.

- W Lubczynski, M., & Gurwin, J. (2005). Integration of various data sources for transient groundwater modeling with spatio-temporally variable fluxes—Sardon study case, Spain. *Journal of hydrology*, 306(1), 71-96.
- Wasowski, J., Bovenga, F., Nitti, D. O., & Nutricato, R. (2012). Investigating landslides with Persistent Scatterers Interferometry (PSI): current issues and challenges. In *Proceedings of the 11th International Symposium on Landslides (ISL) and the 2nd North American Symposium on Landslides at Banff held in Alberta (Canada) in 2012*.
- Wasowski, J. & Bovenga, F. (2014). Investigating landslides and unstable slopes with satellite Multi Temporal Interferometry: current issues and future perspectives, *Engineering Geology*, doi: 10.1016/j.enggeo.2014.03.003
- Watchorn, F., Nichols, G.J. & Bosence, D.W.J. (1998). Rift-related sedimentation and stratigraphy, southern Yemen (Gulf of Aden). In: Purser, B.H., Bosence, D.W.J. (Eds.), *Sedimentation and Tectonics of Rift Basins: Red Sea– Gulf of Aden*. Chapman & Hall, London, pp. 165–191.
- Waterloo Hydrogeologic Inc. (2006). *Visual MODFLOW user's manual*. Ontario, Waterloo Hydrogeologic Inc.
- Wei, M., & Sandwell, D. T. (2010). Decorrelation of L-band and C-band interferometry over vegetated areas in California. *Geoscience and Remote Sensing, IEEE Transactions on*, 48(7), 2942-2952.
- Werner, C., Wegmuller, U., Strozzi, T., & Wiesmann, A. (2003). Interferometric point target analysis for deformation mapping. In *Geoscience and Remote Sensing Symposium, 2003. IGARSS'03. Proceedings. 2003 IEEE International (Vol. 7, pp. 4362-4364)*. IEEE.
- Wieczorek, GF (1984) Preparing a detailed landslide-inventory map for hazard evaluation and reduction. *IAEG Bull* 21(3):337–342.
- Wylie, D.C. & Munn, F.J. (1978). The use of movemnet monitoring to minimise production losses due to pit slope failures, *Proceedings First International Symposium on Stability in Coal Mining*, Miller Freeman, Vancouver, pp. 75 - 94.
- Xue, Y. Q., Zhang, Y., Ye, S. J., Wu, J. C., & Li, Q. F. (2005). Land subsidence in China. *Environmental geology*,
- Yilmaz, I. (2009). Landslide susceptibility mapping using frequency ratio, logistic regression, artificial neural networks and their comparison: A case study from Kat landslides (Tokat—Turkey). *Computers & Geosciences*, 35(6), 1125-1138.
- Yin, Y. (2011). Recent catastrophic landslides and mitigation in China. *Journal of Rock Mechanics and Geotechnical Engineering*. 2011, 3(1):10-18.
- Zavadni, Z.M. & Broadbent, C.D., (1980). Slope failure kinematics. *CIM Bulletin(April)*: pp. 69 - 74.
- Zebker, H. A., & Villasenor, J. (1992). Decorrelation in interferometric radar echoes. *Geoscience and Remote Sensing, IEEE Transactions on*, 30(5), 950-959.
- Zvelebil, J. (1984). Time Prediction of a Rockfall from a Sandstone Rock Slope. *IV International Symposium on landslides, Toronto. (1984). Volume 3*.
- Zvelebil, J. & Moser, M. (2001). *Monitoring Based Time-Prediction of Rock Falls: Three Case-Histories*.